UNIVERSITY OF CALIFORNIA,
IRVINE

Amorphous Intergranular Film Design Criteria and Application as Damage Tolerant Features in Nanocrystalline Alloys

DISSERTATION

submitted in partial satisfaction of the requirements
for the degree of

DOCTOR OF PHILOSOPHY

in Materials Science and Engineering

by

Jennifer Dolores Schuler

Dissertation Committee:
Professor Timothy J. Rupert, Chair
Professor Martha L. Mecartney
Professor Daniel R. Mumm

2019

DEDICATION

I dedicate this thesis to my family: Mom, Dad, Jackie, Grandmom, Grandpop, Aunt Janice, Uncle Randy, Uncle Joe, Aunt Dee, Aunt Marge, Uncle Franny, Uncle Dick, Buster, Princess, and Mr. Furious. I could not have done this without you, and I love you all very much.

I also dedicate this thesis to all of the friends and teachers I have been blessed to have over the years. They helped make me who I am today.

TABLE OF CONTENTS

LIST OF FIGURES

LIST OF TABLES

ACKNOWLEDGMENTS

I have gained so much more from my Ph.D. than simply new knowledge and expertise. I have grown fundamentally as a person, and the way I approach and interact with the world has changed. I think more critically, engage with more confidence, and learn with greater curiosity. All of this growth is attributed to my advisor Tim. Thank you Tim for your patience, guidance, and good-nature over these years.

I also thank the members of my thesis committee, Professor Martha Mecartney and Professor Daniel Mumm, for their guidance and support in the development of this thesis, and I also cannot forget about the Sandia crew: Khalid, Brad, Stephen, Fadi, Nathan H., Nathan M., Chris, Sam, Anthony, Brittany, and Caitlin. My time in Albuquerque was quite a ride, and it would not have been successful without all of you. I also give my warm thanks to all of the staff at IMRI, LEXI, UCLA, and SNL that have helped me turn ideas into reality. Finally, I thank the Rupert group: Charlette, Yang, Megan, Jenna, Zhifeng, Vlad, Olivia, Zhiliang, Jason, Simon, David, and Amir. My journey through higher education has felt mostly lonely, until our group. You all made coming into work every day a blast, and I cherish our friendship.

CURRICULUM VITAE

Jennifer D. Schuler

Education

Ph.D. in Materials Science and Engineering June 2019
University of California, Irvine (UCI) Irvine, CA
Thesis Topic: Amorphous Intergranular Film Design Criteria and Application as Damage Tolerant Features in Nanocrystalline Alloys
Advisor: Dr. Timothy J. Rupert

M.S. in Materials Science and Engineering June 2016
University of California, Irvine (UCI) Irvine, CA

B.S. in Physics May 2011
Rensselaer Polytechnic Institute (RPI) Troy, NY

Research Experience

Research Assistant 2014 - 2019
University of California, Irvine (UCI) Irvine, CA
Thesis Topic: Amorphous Intergranular Film Design Criteria and Application as Damage Tolerant Features in Nanocrystalline Alloys
Advisor: Dr. Timothy J. Rupert

- Investigated the impact of grain boundary structure on damage tolerance using ion beam irradiation and mechanical testing with electron microscopy on thin film and ball-milled nanocrystalline Cu-Zr.
- Developed materials selection rules for amorphous grain boundary formation in binary alloys by combining thermodynamic dopant segregation and bulk metallic glass concepts.
- Evaluated grain growth behaviors of grain boundary engineered alloys including Cu-Zr, Cu-Nb, Cu-Ta, and Ni-W.
- Created metal samples using sputter physical vapor deposition and electroplating, and characterized them using SEM, TEM, STEM, EDS, PED, EBSD, TKD, and FIB.

Research Assistant 2018
Sandia National Laboratories (SNL) Albuquerque, NM
Project: Grain Boundary Complexions as Efficient Sinks for Radiation Damage and Subsequent Influence on Mechanical Behavior
Advisors: Dr. Khalid Hattar, and Dr. Brad Boyce

- Investigated the radiation tolerance and mechanical behavior of grain boundary engineered alloys using in situ TEM techniques including ion beam irradiation, tensile testing, fatigue

testing, PED, and heating as part of the DOE Office of Science Graduate Student Research (SCGSR) Program.

Research Assistant 2009
Kansas State University (KSU) Manhattan, KS
Project: Building a Carbon Nanotube Mode-Locked Fiber Laser and Exploring the Deposition Process in Photonic Bandgap Fibers
Advisors: Dr. Brian R. Washburn, and Dr. Kristan L. Corwin

- Constructed a compact and fully functional mode-locked carbon nanotube fiber laser with exceptional durability as part of the NSF Research Experience for Undergraduates (REU) Program.

Professional Experience

Process Development Engineer 2011 - 2014
International Business Machines (IBM) Hopewell Junction, NY
Supervisors: Ian Melville, Dr. Brian Sundlof, and Dr. Subramanian S. Iyer

- Advanced the growth of semiconductor technology nodes in Wafer Finishing and Packaging by developing key engineering breakthroughs for pivotal projects including 3D technology and lead-free solder for the sputter physical vapor deposition, electroplating, and reactive ion etch unit processes.
- Evaluated the use of XRF to measure Ag composition in electroplated Sn-Ag solders for flip chip applications.

Corporate Internship 2010
International Business Machines (IBM) Albany, NY
Supervisor: Dr. John C. Arnold

- Managed gate-level reactive ion etch semiconductor processing experiments from initial wafer procurement to failure analysis including experimental design and data analysis.

Referred Journal Publications

[1] Schuler JD, Grigorian C, Barr CM, Hattar K, Boyce BL, Rupert TJ. "Improved damage tolerance upon irradiation of nanocrystalline Cu-Zr caused by amorphous intergranular films." *Manuscript in preparation*.

[2] Schuler JD, Briggs SA, Wardini JL, Rupert TJ, Hattar K. “Dewetting instability in thermally stable nanocrystalline binary alloys." *Manuscript in preparation*.

[3] Schuler, JD, Barr, CM, Heckman, NM, Copeland, G, Boyce, BL, Hattar, K, Rupert, TJ. "In situ high-cycle fatigue reveals importance of grain boundary structure in nanocrystalline Cu-Zr." *JOM* (2018): 1-12.

[4] Schuler JD, Donaldson OK, Rupert TJ. "Amorphous complexions enable a new region of high temperature stability in nanocrystalline Ni-W." *Scripta Materialia* 154 (2018): 49-53.

[5] Hu Y, Schuler JD, Rupert TJ. "Identifying interatomic potentials for the accurate modeling of interfacial segregation and structural transitions." *Computational Materials Science* 148 (2018): 10-20.

[6] Schuler JD, Rupert TJ. "Materials selection rules for amorphous complexion formation in binary metallic alloys." *Acta Materialia* 140 (2017): 196-205.

[7] Pun SC, Wang W, Khalajhedayati A, Schuler JD, Trelewicz JR, Rupert TJ. "Nanocrystalline Al-Mg with extreme strength due to grain boundary doping." *Materials Science and Engineering: A* 696 (2017): 400-406.

[8] Pham QN, Larkin LS, Lisboa CC, Saltonstall CB, Qiu L, Schuler JD, Rupert TJ, Norris PM. "Effect of growth temperature on the synthesis of carbon nanotube arrays and amorphous carbon for thermal applications." *Physica Status Solidi (a)* 214.7 (2017): 1600852.

Conference Presentations

[1] “Irradiation and Fatigue of Nanocrystalline Cu-Zr with Amorphous Intergranular Films.” Jennifer D. Schuler, Charlette Grigorian, Christopher M. Barr, Nathan M. Heckman, Guild Copeland, Brad L. Boyce, Khalid Hattar, Timothy J. Rupert. *The Minerals, Metals and Materials Society (TMS) Annual Meeting and Exhibition*. San Antonio, TX. March 2019. (Presenter)

[2] “Establishment of Predictive Criteria for Amorphous Complexion Formation.” Jennifer D. Schuler and Timothy J. Rupert. *Southern California Society of Microscopy and Microanalysis (SCSMM)*. Los Angeles, CA. April 2017. (Presenter)

[3] “Establishment of Predictive Criteria for Amorphous Complexion Formation.” Jennifer D. Schuler and Timothy J. Rupert. *The Minerals, Metals and Materials Society (TMS) Annual Meeting and Exhibition*. San Diego, CA. February 2017. (Presenter)

[4] “Formation and Characterization of Interfacial Complexions in a Range of Transition Metal Alloy Systems.” Jennifer D. Schuler and Timothy J. Rupert. *Gordon Research Conference (GRC) – Structural Nanomaterials*. Hong Kong, China. July 2016. (Poster)

[5] “Physical Vapor Deposition Qualification Criteria Required by 3D Processing.” Jennifer D. Schuler and Jorge Lubguban. *Americas North East Affiliate Face to Face Meeting*. Poughkeepsie, NY. October 2013. (Invited Poster)

[6] “Physical Vapor Deposition Qualification Criteria Required by 3D Processing.” Jennifer D. Schuler and Jorge Lubguban. *IBM Technology Corridor Exchange Conference.* Hopewell Junction, NY. September 2013. (Winner, Best New Hire Poster)

[7] “Assessment of XRF Technique as a Method to Measure Percent Ag in SnAg Solders for Flip Chip Applications.” Jennifer D. Schuler, Chia-Hsin Shih, Charles Arvin, Eric Perfecto and Kyung-Moon Kim. *International Microelectronics Assembly and Packaging Society (IMAPS) Symposium*. San Diego, CA. September 2012. (Presenter and IBM Representative)

Patents

[1] Charles L. Arvin, Harry D. Cox, Arthur G. Merryman, and Jennifer D. Schuler. "Filtering lead from photoresist stripping solution." U.S. Patent 9,804,498, issued October 31, 2017.

[2] Yuri M. Brovman, Brian M. Erwin, Nicholas A. Polomoff, Jennifer D. Schuler, Matthew E. Souter, and Christopher L. Tessler. "Substrate including selectively formed barrier layer." U.S. Patent 9,748,135, issued August 29, 2017.

[3] Charles L. Arvin, Wolfgang Sauter, and Jennifer D. Schuler. "Control of silver in C4 metallurgy with plating process." U.S. Patent 8,759,210, issued June 24, 2014.

[4] Charles L. Arvin, Eric D. Perfecto, Wolfgang Sauter, and Jennifer D. Schuler. "Solder volume compensation with C4 process." U.S. Patent 8,742,578, issued June 3, 2014.

[5] John C. Arnold, Jennifer D. Schuler, and Yunpeng Yin. "Method for forming small dimension openings in the organic masking layer of tri-layer lithography." U.S. Patent 8,735,283, issued May 27, 2014.

ABSTRACT OF THE DISSERTATION

Amorphous Intergranular Film Design Criteria and Application as Damage Tolerant Features in Nanocrystalline Alloys

By

Jennifer Dolores Schuler

Doctor of Philosophy in Materials Science and Engineering

University of California, Irvine, 2019

Professor Timothy J. Rupert, Chair

The large grain boundary volume fraction of nanocrystalline metals can bestow desirable mechanical behaviors, but the same grain boundaries that impart these beneficial properties challenge their application. Excess surface energy due to the substantial interfacial volume drives grain growth, and thus a loss of the benefits gained by nanocrystalline grain sizes. Also, not all grain boundaries are equal, where material behaviors can fluctuate dramatically depending on the grain boundary structure and composition. New pathways to fundamentally alter the grain boundary structure are needed to stabilize the nanocrystalline grain size and leverage the full potential of nanocrystalline metals.

"Complexion" is a term used to describe the phase-like behavior of grain boundaries, where grain boundaries, similar to bulk phases, can undergo discrete transitions in structure and composition based on external factors such as temperature. Amorphous intergranular films, a type of complexion, are of particular interest due to their ability to enhance both mechanical and radiation damage tolerance due to the excess free volume present in these structures. In this thesis, we seek to expand the current materials toolbox of alloys that can form amorphous intergranular films, and then investigate the impact of these unique damage tolerant features in applications

where they can be leveraged. First, we propose a set of materials selection rules aimed at predicting the formation of amorphous intergranular films, and then apply these rules to discover new alloys that can form these features. In doing this, we also discover a counterintuitive, ultra-high temperature grain size stabilization regime driven by the formation of amorphous intergranular films. Next, we investigate the impact of these features in applications where damage tolerance is critical, particularly fatigue and radiation. We find that incorporation of amorphous intergranular films throughout the grain boundary network of nanocrystalline alloys increases plasticity preceding a fatigue crack, and dramatically improves radiation tolerance. In summary, through an array of sputtered, electroplated and ball-milled Cu and Ni-based alloys, specialized heat treatments, and electron microscopy techniques, we find that amorphous intergranular films can potentially be found in a large number of alloys, and can dramatically improve nanocrystalline alloy behaviors.

Chapter 1: INTRODUCTION

1.1 The Motivation for Nanocrystalline Metals

While grain size is the standard metallurgical parameter, it is often the overlooked spaces between the grains, the grain boundaries, that drive many observed behaviors [1]. For example, grain boundaries increase strength by disrupting dislocation motion [2], but can also be weakest links and serve as fracture initiation sites [3]. Single crystal Ni superalloys, such as those found in the turbine blades of jet engines, eschew grain boundaries entirely in order to eliminate grain boundary diffusion and achieve unparalleled creep resistance [4]. If such benefits are possible on one extreme of the grain size spectrum by eliminating grain boundaries when problematic, then perhaps new desirable behaviors can be found by instead maximizing the number of grain boundaries when they are beneficial.

The portion within a material composed of grain boundary, called the grain boundary volume fraction, can be increased by decreasing the grain size, and nanocrystalline metals with grain sizes <100 nm take this concept to the extreme. For example, given a 1 nm grain boundary thickness and a 10 nm grain size, 30% of the material volume is composed of grain boundary [5]. This substantial grain boundary volume fraction bestows a host of desirable mechanical behaviors [6], most notably increased strength [7, 8]. The Hall-Petch effect defines the relationship between grain size and strength as shown in Equation 1:

$$\sigma_y = \sigma_o + \frac{k}{\sqrt{d}} \qquad (1)$$

where σ_y is yield strength, σ_o and k are material constants, and d is grain size [9]. Strength generally increases as grain size decreases, with the exception of the finest grain sizes where a transition to interfacial dominated behaviors causes an inverse effect [2], as shown in Figure 1.1. In addition

to increased strength, improved wear resistance [10-12] and longer fatigue lifetimes [13] have also been reported for nanocrystalline metals.

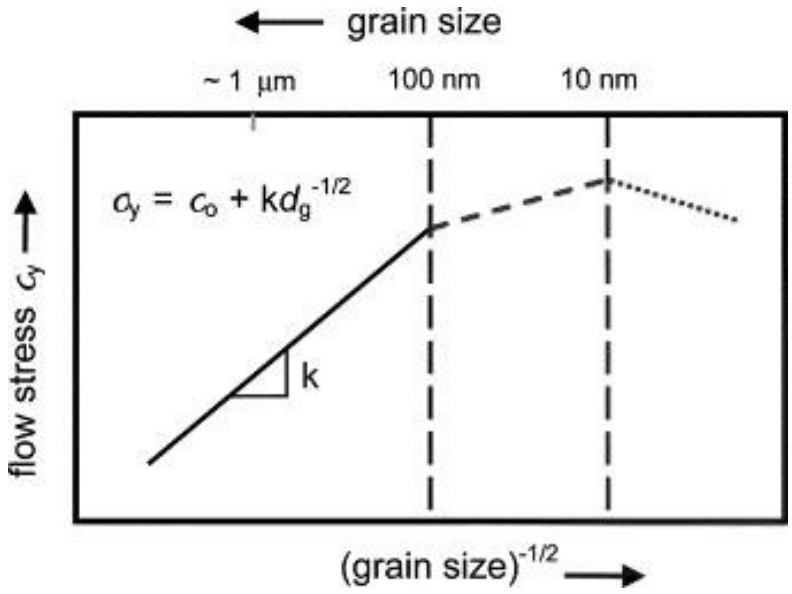

Figure 1.1. A schematic of the Hall-Petch effect showing the relationship between grain size and strength, from [2]. Strength increases as grain size decreases, with the exception of the smallest grain sizes.

These desirable behaviors driven by large grain boundary volume fractions ultimately boil down to the behavior of each individual grain boundary. The behavior of a grain boundary is determined by its structure and composition, and is commonly described using the five parameters of grain boundary character [14]. The lattice misorientation is defined by three degrees of freedom, and the grain boundary plane orientation has two degrees of freedom, comprising the five total parameters [15, 16]. The coincident site lattice (CSL) model can also be used to describe the grain boundary structure. Repeated units are formed from points where misoriented lattices coincide, and this repetition is described by the parameter Σ which is defined as the reciprocal ratio of coincident sites to the total number of sites. For example, Σ3 represents a twin boundary in a face-centered cubic lattice, meaning that one atom is shared between the two grains for every three atoms located in the lattice. Due to this definition, there is generally an inverse relationship

between structural order and Σ number, where grain boundaries with a higher Σ value have less structural order and vice versa. Increased levels of structural order are also connected to lower grain boundary energy levels, where grain boundaries with a low Σ value also tend to be low energy [17, 18]. Figure 1.2 plots grain boundary energy versus misorientation angle for a symmetric <110> tilt grain boundary in face-centered cubic Al. The energy minima show Σ3 and Σ11 special grain boundaries, illustrating the relationship between high structural order and low grain boundary energy.

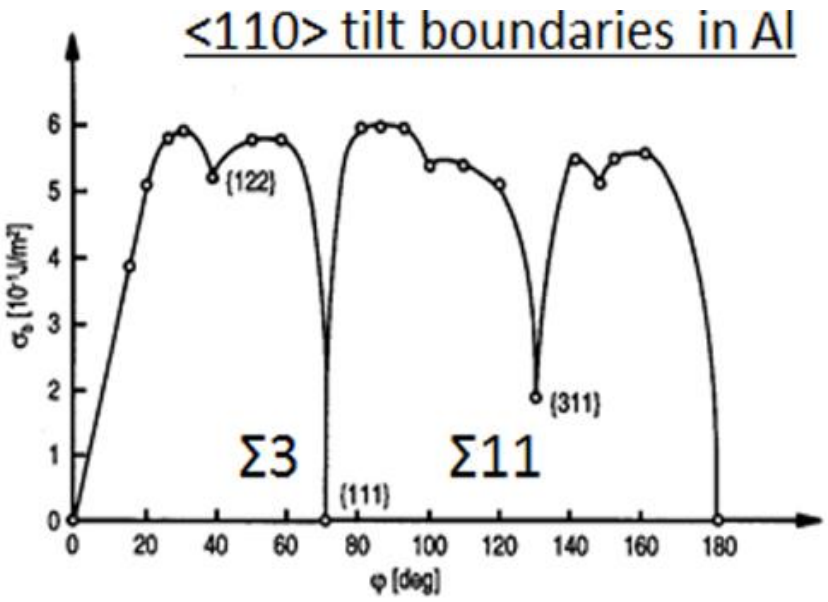

Figure 1.2. Grain boundary energy versus tilt angle for <110> boundaries in Al, from [15]. Energy minima for special boundaries Σ3 and Σ11 are indicated.

The grain boundary energy is also a function of composition as shown in Equation 2 [19, 20]:

$$\gamma = \gamma_0 - \Gamma(\Delta H^{seg} + RT \ln X) \qquad (2)$$

where γ is the grain boundary energy, γ_o is the original grain boundary energy of the pure metal, Γ is the grain boundary solute excess, ΔH^{seg} is the enthalpy of segregation, R is the Boltzmann

constant, T is the temperature, and X is global dopant composition. The equation ultimately means that segregation of dopant to grain boundaries can lower the grain boundary energy and consequently change its behavior.

1.2 Grain Boundaries: The Problem and Solution

The enhanced properties of nanocrystalline metals are attributed to their large volume fraction of grain boundaries [1], but the same grain boundaries that generate these desirable characteristics in turn serve to frustrate their application. Nanocrystalline metals are highly susceptible to grain growth, driven by a desire to lower the energy penalty associated with the large interfacial volume [21-28]. Grain growth can be simply pictured by looking at the velocity of a grain boundary (v) [29]:

$$v = M_{gb} \cdot \gamma_{gb} \cdot \kappa \tag{3}$$

where M_{gb} is the grain boundary mobility, γ_{gb} is the grain boundary energy, and κ is the local mean curvature of the boundary. From Equation 3, grain boundary velocity and therefore grain growth is a function of kinetic and thermodynamic components, where the thermodynamic component can be calculated using Equation 2. A tremendous amount of recent research has shown that these components can be influenced by alloying and selective doping, ultimately suppressing grain growth in a range of nanocrystalline metals [30-45].

Kinetically, the grain boundary mobility can be impeded through solute drag and Zener pinning caused by particle dispersions [30-35, 46], which has been observed in Cu-Ta [35, 47], and Cu-Nb [48]. Thermodynamically-driven stabilization is characterized by solute segregation to the grain boundary because it is energetically favorable for dopants to reside at interfaces compared to the crystalline interior. Such behaviors have been captured in various computational models [20, 39, 40, 49], which predict alloys that can sustain stabilized nanocrystalline structures,

and have been confirmed experimentally in binary alloys including Ni-W [50], W-Ti [20], and Fe-Zr [51]. Figure 1.3 shows a computationally derived library of dopant segregation tendencies, defined as ΔH^{seg}, for a wide variety of binary metallic alloys [39]. Essentially, the binary combination indicated with a red square will have preferential dopant segregation to the grain boundary that will stabilize the nanocrystalline grain size. This parameter has been extended into a full set of stability criteria in order to design alloys that have optimal thermodynamic grain size stability [42].

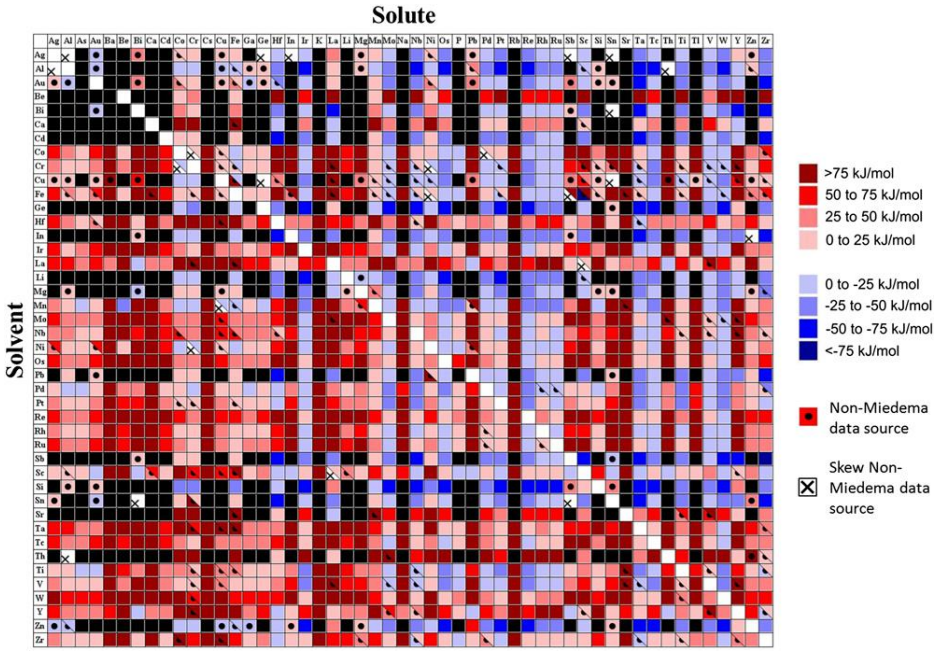

Figure 1.3. The enthalpy of segregation (ΔH^{seg}) for many binary alloys, where the base metal is the solvent, and the dopant is the solute, from [39]. The red scale means a positive ΔH^{seg} and a tendency for solute segregation to the grain boundary. The blue scale means a negative ΔH^{seg} and a tendency for depletion of solute at the grain boundary. Black indicates insufficient data for a calculation, and a dot or "x" indicates the data source.

Dopant segregation does not occur equally across the grain boundary network due to the distribution of structures, compositions, free volumes, and energies at each grain boundary. Instead, dopant segregation occurs heterogeneously, where different grain boundaries have different dopant atomic fractions [52-54]. This is shown in Figure 1.4 in nanocrystalline Pt with

different degrees of segregated Au dopant across the grain boundary network [52]. This heterogeneous dopant distribution has been observed to impact mateiral behaviors. For example, differences in dopant grain boundary concentration across the grain boundary network can increase toughness by causing nanoscale crack arrest, where an ideal global concentration can be found to optimize both nanocrystalline stability and energy dissipation [55]. Also, thermodynamic and kinetic mechanisms for nanocrystalline stability depend on the dopant concentration, and eventually break down with increasing temperature where rapid coarsening is then observed [50]. New methods to tailor the grain boundary network in order to achieve ideal dopant segregation and structural distributions for optimal mechanical behaviors and grain size stabilization at high temperatures are necessary in order to further improve the application of nanocrystalline metals in extreme environments.

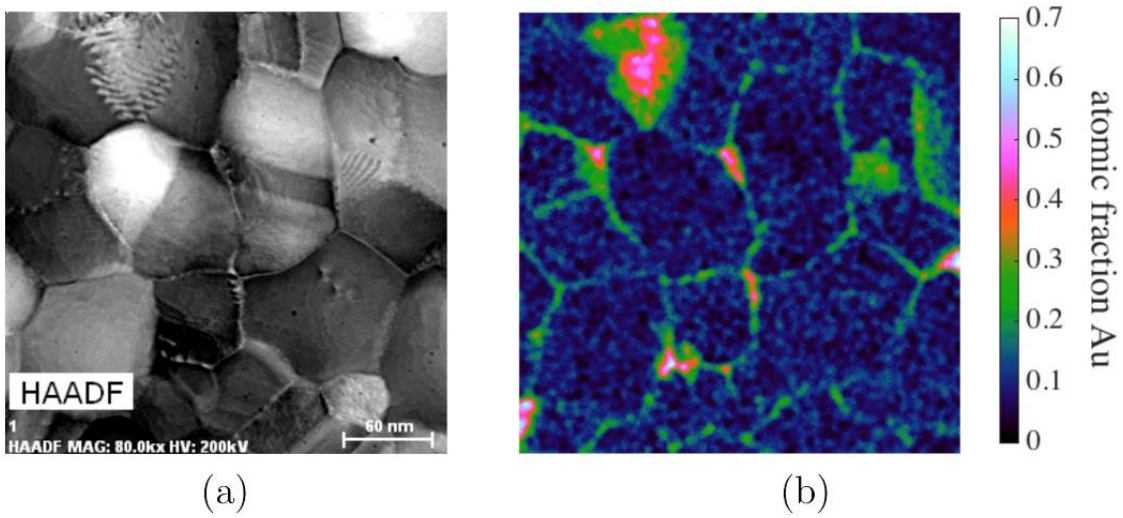

Figure 1.4. Nanocrystalline Pt with Au dopant segregation to the grain boundaries, from [52]. (a) shows the high angle annular dark field (HAADF) image, and (b) shows the corresponding Au concentration map gathered using energy dispersive X-ray spectroscopy. The atomic fraction of Au at the grain boundary is indicated by the color gradient scale.

1.3 Complexions: A Powerful Perspective

An exciting concept for the design and control of interfacial properties are complexions, defined as interfacial structures that are in thermodynamic equilibrium and have a stable, finite thickness [56-58]. Complexions can be considered quasi-2D "phases" that only exist at an interface, surface, or grain boundary [59]. Since their existence is dependent on the neighboring crystalline grains, complexions do not technically adhere to the Gibbs definition of a phase and thus are considered with this separate terminology [59, 60]. Dillon et al. [56] developed a convention to classify complexions into six different types according to thickness, structural ordering, and composition, shown in Figure 1.5. The six types suggested in Figure 1.5 were: (a) sub-monolayer segregation, (b) clean, undoped grain boundaries, (c) bilayer segregation, (d) multilayer segregation, (e) nanoscale intergranular films, and (f) wetting films. This continuum of complexion types can be subdivided into ordered or disordered. Complexion types in Figures 1.5(a)-(d) have crystalline structure and are classified as ordered, whereas the types in Figures 1.5(e) and (f) can assume either an ordered or disordered structure. The disordered versions of Figures 1.5(e) and (f) can be classified as amorphous intergranular films (AIFs) [56].

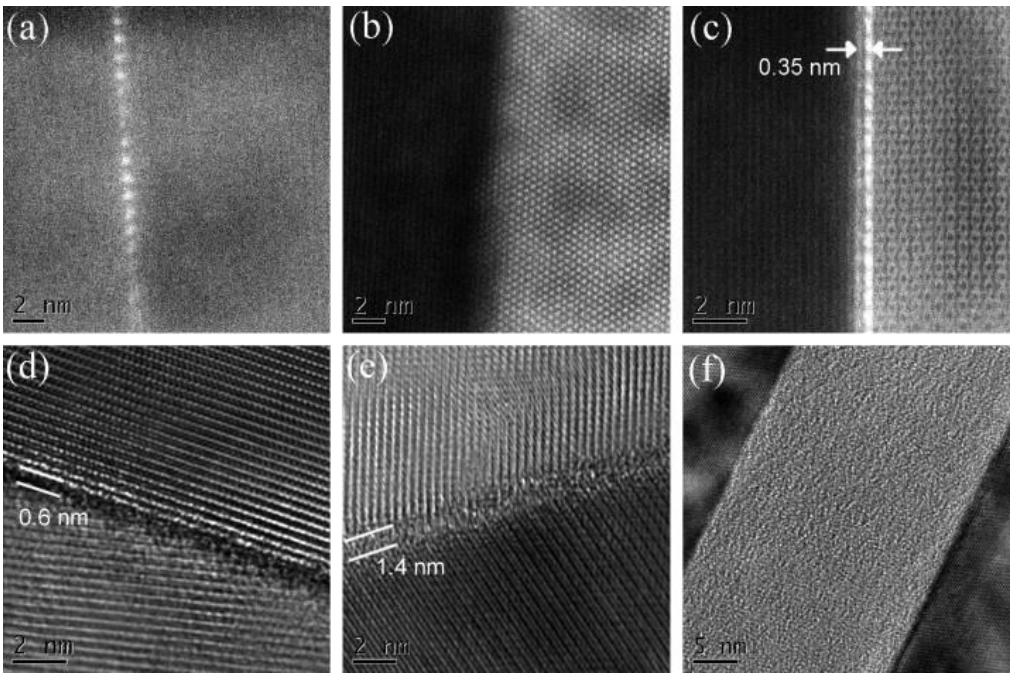

Figure 1.5. Classification of complexion types according to thickness, from [56]. The complexions are classified as follows, (a) sub-monolayer segregation, (b) clean, undoped grain boundaries, (c) bilayer segregation, (d) multilayer segregation, (e) nanoscale intergranular films, and (f) wetting films.

Similar to bulk phases, complexions can be described with thermodynamic parameters and can even undergo phase-like transitions in response to alterations of external variables such as temperature, pressure, and chemistry [58, 59, 61]. The interfacial potential between the adjoining grains can be calculated as a function of the grain boundary thickness, composition, and interatomic distance assuming exponentially decaying interfacial forces. This results in an oscillating free energy versus complexion thickness relationship where energy minima occur when the complexion thickness is an integer number of bond lengths. This means that energetically favorable grain boundary structures with characteristic thicknesses can occur [62]. Figure 1.6 shows these discrete complexion equilibrium thicknesses (h) with increasing temperature (T) and chemical potential (μ) in accordance with complexion type transitions [62]. Different complexion types have been shown to dramatically influence material behavior and have been deemed the root

cause of several previously unexplained phenomena. Ordered bilayer complexions were found to explain liquid metal embrittlement in Cu-Bi [63] and Ni-Bi [64] due to the segregation of Bi to the grain boundaries which stretches the intergranular atomic bonds to near the breaking point, making them very fragile. Similarly, Ga segregates to the grain boundaries in Al-Ga to form an ordered multilayer complexion that also has an embrittling effect [65]. By preferentially incorporating certain complexion types within the grain boundary network of nanocrystalline metals, dramatic changes to grain boundary structure and composition can be achieved, resulting in dramatically changed material behaviors.

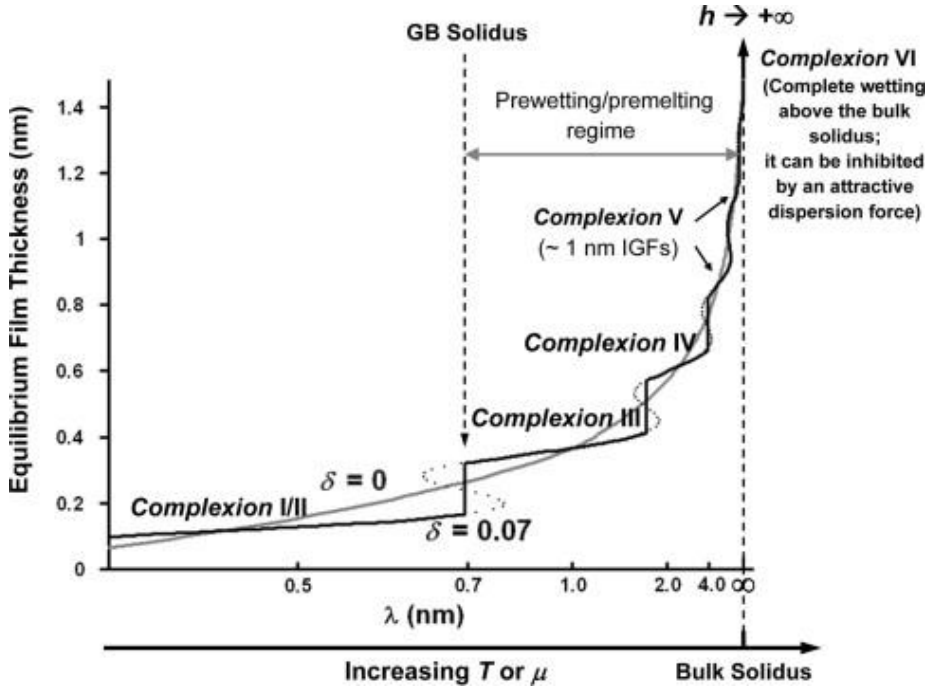

Figure 1.6. Discrete transitions in complexion equilibrium thickness (*h*) with increasing temperature (T) or chemical potential (μ) in accordance with complexion type transitions, from [62].

1.4 The Motivation for Amorphous Intergranular Films

The AIFs investigated in this thesis are the disordered version of the nanoscale film complexion consisting of dopant-enriched grain boundaries with nanometer-scale thicknesses and amorphous structure [56]. Figure 1.7 shows high resolution transmission electron microscopy (TEM) images of AIFs in Cu-Zr compared to a traditional, ordered grain boundary [66]. The insets show the associated fast Fourier transform patterns for each region, highlighting the crystallinity of the grains and amorphousness of the AIFs. AIFs form when the energy needed to create an amorphous region of a given thickness with two new crystalline-amorphous interfaces is less than the energy of the original grain boundary, shown in Equation 4 [62]:

$$\Delta G_{amorph} \cdot h + 2\gamma_{cl} < \gamma_{gb} \tag{4}$$

where ΔG_{amorph} refers to the volumetric free energy penalty for an undercooled amorphous film at a given binary alloy composition, h is the film thickness, γ_{cl} is the excess free energy of the new crystalline-amorphous interfaces, and γ_{gb} is the excess free energy of the original crystalline grain boundary. Figure 1.7(e) shows a range of measured AIF thicknesses present in the alloy in accordance with Equation (4). In effect, AIF formation is a form of grain boundary premelting, which is prohibitively difficult to observe in pure metals [67] but accessible for highly doped boundaries.

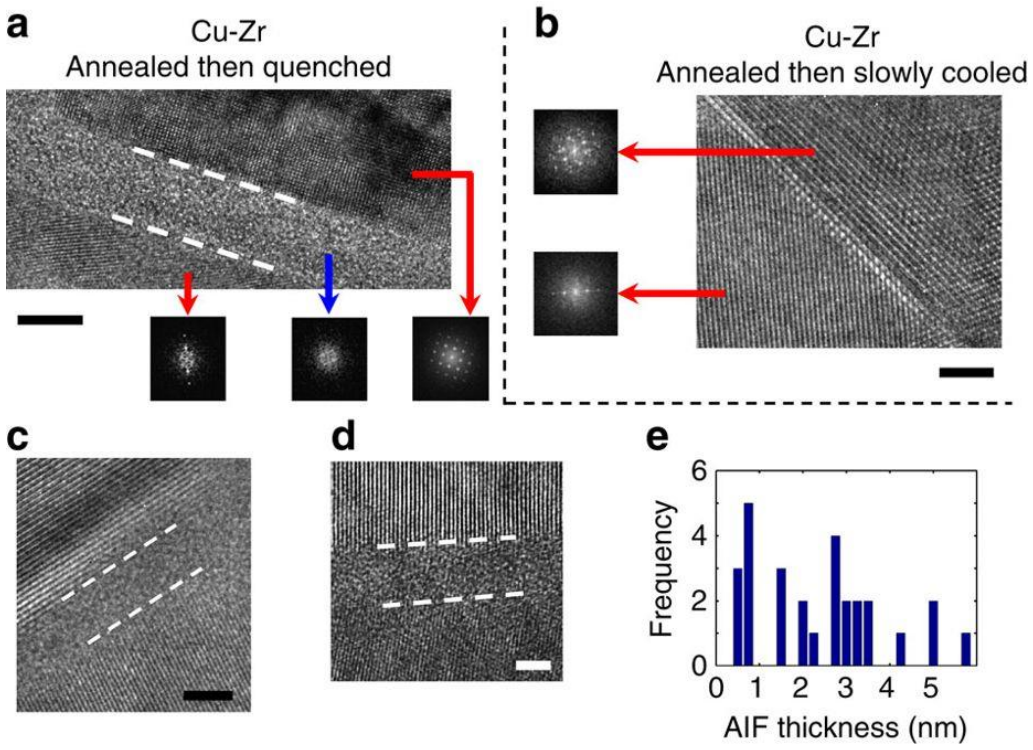

Figure 1.7. High resolution transmission electron microscopy images of amorphous inergranular films (AIFs) in Cu-Zr, from [66]. (a) shows AIFs from a quenched sample, whereas (b) shows the slowly cooled sample containing only ordered grain boundaries. The insets show the fast Fourier transforms taken across the grain boundaries. (c) and (d) show AIFs of other thicknesses, and (e) shows a frequency plot of measured AIF thicknesses.

AIFs have been shown to impart extremely desirable behaviors when incorporated within nanocrystalline metals. Unlike bilayer complexions that can embrittle in Ni-Bi and Cu-Bi, AIFs have been shown to improve damage tolerance due to the excess free volume present in the amorphous grain boundary structure [68-70]. Atomistic simulations have shown that the amorphous-crystalline interfaces that bound AIFs can attract dislocations [70]. Also, molecular dynamics simulations have shown that AIFs increase toughness by delaying intergranular crack formation and propagation [68, 69], increase radiation tolerance by acting as efficient and unbiased sinks for point defects [71], and increase strength through dislocation pinning [72]. Experimental studies support these findings, where nanocrystalline Cu-Zr containing AIFs had enhanced

strength and ductility compared to the same alloy with only ordered grain boundaries [66]. Figure 1.8 shows a strain-to-failure versus yield strength plot for a variety of nanocrystalline metals, where the alloys containing AIFs, indicated by red circles, had both significantly longer strain-to-failures and increased yield strengths [66]. AIFs have also been shown to dramatically increase diffusion which can cause solid state activated sintering [56, 62]. Solid state activated sintering, referring to improved densification rates that occur below the solidus temperature, has been observed in both metallic and ceramic systems. The addition of a small amount of sintering aid element creates disordered intergranular films that act as pathways for improved diffusion below the bulk eutectic temperature [62, 68-71, 73]. In addition, AIFs were recently found to stabilize nanocrystalline grain structures against grain growth at elevated temperatures, with a nanocrystalline Cu-Zr alloy remaining nanostructured even after a week at 98% of its melting temperature (950 °C) [74]. This is shown in Figure 1.9 where the 950 °C Cu-Zr anneal is represented by the green squares.

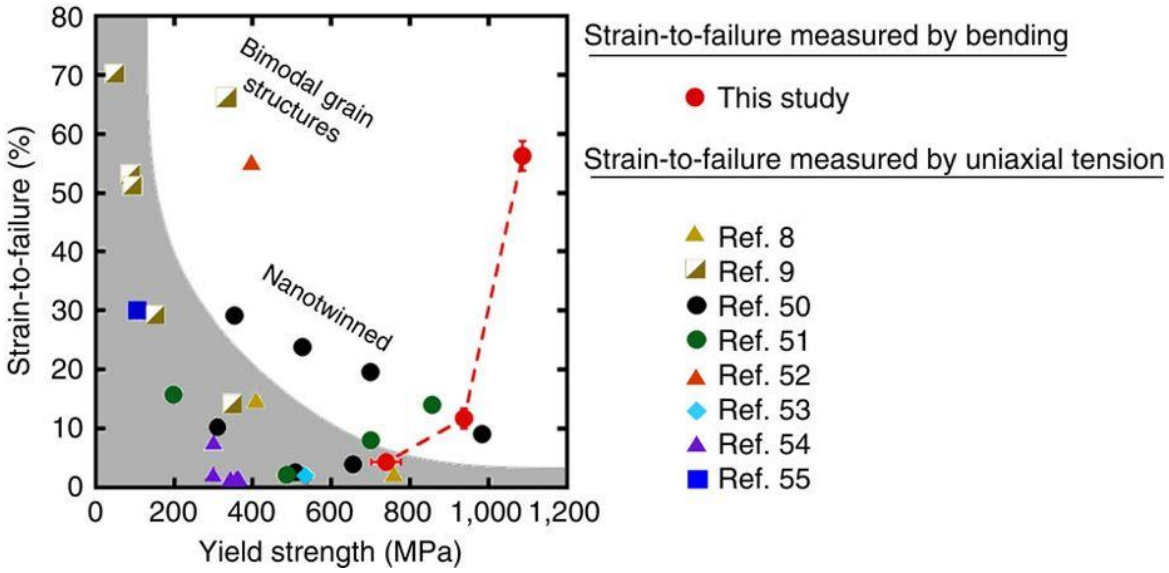

Figure 1.8. Strain-to-failure versus yield strength plot for a variety of nanocrystalline metals, from [66]. The alloys containing AIFs, indicated by the red circles, had both significantly improved strain-to-failure and increased yield strength compared to other nanostructured metals.

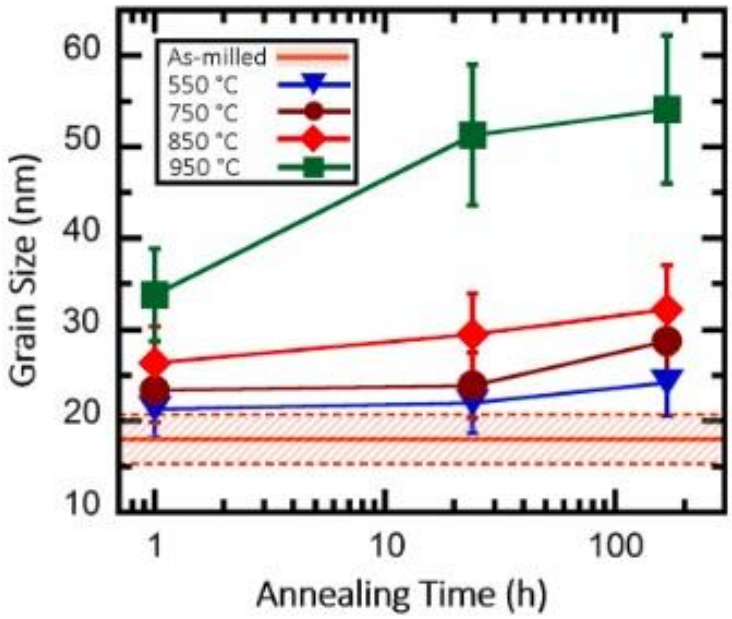

Figure 1.9. Grain size as a function of annealing time in nanocrystalline Cu-Zr at a variety of annealing temperatures, from [74].

1.5 Problem Statement and Research Objectives

Nanocrystalline metals offer a variety of desirable mechanical behaviors, but are ultimately challenged by uncontrolled grain growth. Thermodynamic and kinetic mechanisms to stabilize the grain size are possible, but generally break down at high temperatures. In order to apply nanocrystalline alloys in extreme environments that operate at high temperatures and leverage their desirable mechanical behaviors, new methods are needed to dramatically engineer the grain boundary network. Complexions offer this possibility by considering grain boundaries as phase-like features that can have radically different compositions, structures, and behaviors. AIFs, a type of complexion, are especially intriguing since they both increase nanocrystalline grain size stability extremely close to the melting point and improve damage tolerance. Few alloys are known to form these features and consequently few application studies exist.

In order to address the issues, the present work is organized as follows:

- Chapter 2: First we investigate material parameters that drive AIF formation, and use those parameters to predict new binary alloys in which AIFs are accessible. Borrowing concepts from bulk metallic glass materials design, we find that the enthalpy of segregation and enthalpy of mixing best indicate if an alloy can form AIFs.
- Chapter 3: We then flex our new predictive muscle in order to discover new binary alloys that can form AIFs, and we find that Ni-W, a well-studied nanocrystalline alloy, can indeed form AIFs. Using Ni-W, we also discover a counterintuitive, ultra-high temperature stability regime driven by AIF formation.
- Chapter 4: Now having populated the materials toolbox of alloys that can form AIFs, we turn our attention to applying these features in environments that can benefit from large

volume fractions of grain boundaries and increased damage tolerance. Fatigue is a primary candidate, and in situ TEM fatigue testing is used to investigate the impact of AIFs on toughness in nanocrystalline Cu-Zr.

- Chapter 5: Nuclear radiation is also an extreme, high temperature environment where nanocrystalline alloys with AIFs may be extremely beneficial. In situ TEM and ex situ bulk irradiation on nanocrystalline Cu-Zr are used to investigate the impact of AIFs on radiation tolerance.

Chapter 2: Materials Selection Rules for Amorphous Complexion Formation in Binary Metallic Alloys

The contents of this chapter have been previously published as [75] J.D. Schuler, T.J. Rupert, Materials selection rules for amorphous complexion formation in binary metallic alloys, Acta Mater. 140 (2017) 196.

2.1 Introduction

Due to the enhanced performance imparted by AIFs, the application of these unique grain boundary structures to a wider array of alloys would be advantageous. The hypothesis of surface premelting promoted interest in stable interfacial films [76], which lead to thermodynamic descriptions of 2D-interfacial films that undergo phase transformations [77-79]. Complexions have since been extensively studied in ceramics [56, 59, 80] and multicomponent metallic systems where AIFs are accessible [81, 82]. Advancement of the thermodynamic theories behind complexions has even allowed for the development of grain boundary phase diagrams that connect structural transitions at an interface with alloy composition and temperature, emphasizing their phase-like behavior [57, 62].

While the theoretical framework behind AIF formation is well-developed, the implementation of this concept to new alloy systems has been limited. The experimental study and application of these features has been largely relegated to ceramics where AIFs have been extensively observed [56, 83], or in alloys where AIFs were already suspected, such as those alloys that exhibit the AIF-driven behavior of solid state activated sintering [84]. Development of a general set of materials selection rules using readily available material parameters to predict material systems in which AIFs are possible would be powerful. The history of amorphous materials research can serve as an instructive example of this concept. In 1932, Zachariasen [85] offered a critical discussion of the structure of glassy ceramics and suggested general guidelines for materials selection, prompting a flurry of discoveries and advancements built upon these

guidelines. Despite their rudimentary nature, Zachariasen's rules are recognized as one of the first attempts to systematically address glass forming ability, fundamentally influencing future research in the field [86]. Similarly, as interest began to build for amorphous metals, Inoue [87] suggested a set of three empirical rules that have since provided a preliminary guide for the development of new bulk metallic glasses (BMGs).

In this study, we propose materials selection rules for the promotion of AIFs that emphasize dopant segregation to grain boundaries and the creation of energetically favorable conditions for forming an amorphous region. To test the robustness of these rules, a variety of Cu-rich systems with contrasting thermodynamic parameters were selected and processed. Here, we focus on transition metal dopants in order to avoid complicating factors such as directional bonding, complex kinetics, and crystallographic anisotropy dependence that are characteristic of ceramic systems [62, 88, 89]. The behavioral patterns established by the inspection of the Cu-rich alloys are then extended to predict the complexion formation behavior of a new Ni-based alloy where AIFs have not yet been observed in prior work. In summary, the type of complexion formed at the grain boundaries of a polycrystalline binary metallic alloy can be controlled by an informed selection of enthalpy of segregation (ΔH^{seg}), enthalpy of mixing (ΔH^{mix}), and atomic radius mismatch, where AIF formation depends on dopant segregation to the grain boundary and the glass forming ability of the alloy.

2.2 Materials and Methods

The alloys used in this study were produced with magnetron co-sputtering using an Ar plasma in an Ulvac JSP 8000 metal deposition sputter tool. Sputtering was specifically chosen in order to create high purity samples. High-purity targets were obtained from Kurt Lesker with purities of 99.99 wt.% for Cu, 99.2 wt.% (inc. Hf) for Zr, 99.9 wt.% (exc. Zr) for Hf, 99.95 wt.%

(exc. Ta) for Nb, 99.95 wt.% for Mo, and 99.99 wt.% for Ni. In addition, deposition was only performed after a 10^{-7} mTorr base chamber pressure was achieved to further minimize impurity incorporation into the films. The films were deposited at 400 °C using an Ar pressure of 1.5 mTorr with sample stage rotation during deposition in order to achieve a uniform film. The metals were co-deposited onto Cu or Ni substrates which had been polished to a mirror surface finish prior to deposition. Films were deposited onto sheets of the primary alloying element in order to eliminate unwanted chemical reactions between the thin film and substrate during subsequent thermal processing. A summary of the key deposition parameters, processing details, and film information are presented in Table 2.1. Additional insight regarding the sputter and anneal processes are presented in Appendix A.

Alloy	Substrate	Dep. Temp. (°C)	Solute/ Solvent Dep. Power (W)	Ar base Pressure (mTorr)	Dep. Rate (Å/sec)	Avg. Film Thickness (µm)	Post Quench (at. %)	Avg. Grain Size (nm)	$0.92T_{solidus}$ (°C)
Cu-Zr	Cu	400	75/150	1.5	1.8	1.94	4.3	99 ± 29	900
Cu-Hf	Cu	400	75/150	1.5	1.7	2.04	6.2	47 ± 12	915
Cu-Nb	Cu	400	75/150	1.5	1.6	1.92	2.7	468 ± 185	1000
Cu-Mo	Cu	400	75/150	1.5	1.6	1.82	3.3	85 ± 26	1000
Ni-Zr	Ni	400	75/150	1.5	0.9	1.34	5.5	40 ± 12	1100

Table 2.1. The sputter deposition parameters including substrate, deposition temperature, power, base pressure and deposition rate. Also included is the resultant film thickness, dopant percentage and final grain size of each alloy after all thermal processing treatments were completed.

Since the average thickness of a transmission electron microscope (TEM) sample must generally be <100 nm in order to achieve electron transparency [90], very small grains can overlap, introducing uncertainty to structural and chemical analysis [91]. In order to minimize this issue, high sputtering temperatures were chosen in order to increase atom mobility and maximize grain size at deposition, as well as suppress the growth of a void-filled film [92]. A micrometer-scale film thickness was also targeted since the maximum grain size achievable in a thin film is typically

tied to the film thickness [93]. After deposition, all samples were annealed under vacuum at 500 °C for 24 h to promote further grain growth and allow for segregation of dopants to the grain boundary to achieve chemical equilibrium.

Target alloy compositions were chosen far from intermetallic transitions but above the solid solubility limits in order to minimize the unwanted precipitation of second phases while still promoting grain boundary segregation. Different complexion types can be accessed by modulating annealing conditions, such as temperature and pressure, to control complexion type transformations [59], with higher temperatures promoting the formation of thicker AIFs [57]. In order to maximize AIF formation, the samples were heated to ~0.92$T_{solidus}$ of the alloy at the measured composition (900 °C for Cu-Zr, 915 °C for Cu-Hf, and 1000 °C for both Cu-Nb and Cu-Mo), held for 1 minute and then rapidly quenched to preserve any thermodynamically stable interfacial structures that are only achievable in the heated state. In order to execute the heating and quenching steps without oxidation, the samples were sealed under vacuum in high purity quartz tubes, suspended in a vertically-oriented tube furnace for the high temperature annealing, and then dropped into a water bath in under 1 s for quenching. The 500 °C anneal for 24 h permits long range diffusion of the dopants. After this, the diffusion length scales calculated for the ~0.92$T_{solidus}$ anneal for 1 minute are on the scale of hundreds of nanometers for each alloy, providing ample opportunity for dopants already localized at the grain boundary post the 500 °C anneal for 24 h to reorder across the nanometer scale. This local reorganization thus permits dopants segregated to the grain boundary to reorder into a thermodynamically favorable state, such as an AIF.

TEM samples were created using the focused ion beam (FIB) lift-out technique on an FEI dual beam Quanta 3D microscope using Ga^+ ions. To reduce ion beam damage, all TEM samples

received a final polish with a low power 5 kV beam to remove surface amorphization and minimize damage caused by the beam. Bright field (BF) TEM images and selected area electron diffraction (SAED) patterns were collected using a Philips CM-20 operating at 200 kV. The average grain sizes of the alloys were determined by measuring the areas of at least 100 grains and calculating the average equivalent circular diameter. High resolution TEM (HRTEM) was performed on an FEI Titan at 300 kV. Energy-dispersive X-ray spectroscopy (EDS) and high angle annular dark field (HAADF) scanning TEM (STEM) were collected on the same microscope at 300 kV. Fresnel fringe imaging was used to identify interfacial films as well as to ensure edge-on orientation of the grain boundary during imaging [94].

2.3 Results and Discussion

2.3.1 Proposed Materials Selection Rules for AIF Formation

We hypothesize that two key requirements must be satisfied for a nanoscale amorphous complexion to form in a binary metallic alloy. First, sufficient excess dopant needs to be present at the grain boundary in order to drive AIF formation. In situ TEM heating experiments have shown that grain boundary premelting is vanishingly difficult in pure monotonic metals, with an ordered boundary structure persisting to at least 99.9% of the melting temperature [67]. Alternatively, the addition of a segregating dopant can make grain boundary premelting conditions accessible at much lower temperatures (e.g., 60-85% of the melting temperature for W-rich alloys [84]), explaining solid state activated sintering [95]. The enthalpy of segregation, ΔH^{seg}, describes whether it is energetically favorable for a dopant element to segregate to the grain boundary in a polycrystalline system, with a positive value denoting a propensity for segregation and a negative value denoting a preference for depletion of the dopant at the grain boundary [39].

Murdoch and Schuh [39] developed a catalogue of ΔH^{seg} values using a Miedema-type model for a large number of binary alloy combinations in order to further understand the role of this parameter in stable nanocrystalline alloy design. By lowering the grain boundary energy through dopant segregation, the thermodynamic driving force for grain growth is mitigated, allowing these materials to retain their desirable nanocrystalline structure even when exposed to elevated temperatures [19]. The theoretical framework to predict stable nanocrystalline materials using a thermodynamic stabilization route has made considerable progress in recent years [36-42, 49]. Darling et al. [43] also contributed to this field by calculating stability maps for the solute composition needed to minimize the excess grain boundary energy for a given grain size and temperature. Both types of studies provide a firm foundation for elemental selections when designing thermally-stable nanocrystalline alloys by utilizing grain boundary segregation. Similarly, the first requirement for nanoscale AIF formation is that ΔH^{seg} must be positive to ensure sufficient dopant is situated at the grain boundary.

The second requirement for AIF formation is that it must be energetically favorable for the grain boundary to assume an amorphous structure with a stable thickness and chemical composition. Nanoscale AIF formation is energetically favorable when the free energy penalty associated with the formation of a disordered film of a certain thickness is less than the reduction in interfacial energy caused by the replacement of the original crystalline grain boundary with two new amorphous-crystalline interfaces, as summarized in Equation 5 (the same as Equation 4 but rearranged for clarity) [62]:

$$\Delta G_{amorph} \cdot h < \gamma_{GB} - 2\gamma_{cl} \equiv \Delta\gamma \qquad (5)$$

ΔG_{amorph} refers to the volumetric free energy penalty for an undercooled amorphous film at a given alloy composition, h is the film thickness, γ_{gb} is the excess free energy of the original crystalline

grain boundary, and γ_{cl} is the excess free energy of the crystalline-amorphous interface. From Equation 5, it is advantageous to have a small volumetric free energy penalty for the amorphous phase to promote AIF formation or alternatively sustain thicker AIFs. Due to their amorphous structure, AIFs bear a clear resemblance to BMGs. Prior work has even shown that the short-range structural order in the interior of an AIF is identical to a bulk amorphous phase [96]. As such, we propose that the materials selection rules used for the creation of BMGs can be instructive for nanoscale AIFs.

Three empirical guidelines, primarily introduced by Inoue [87], have been used to improve the glass forming ability (defined as the critical cooling rate needed to retain an amorphous structure during solidification from the melt) of materials for BMG production. First, multi-component alloys, usually consisting of three or more elements, increase the complexity and size of the possible crystalline structures, reducing the possibility of long range periodicity upon cooling [87, 97]. While ternary and higher alloys make the best BMGs, examples exist in binary systems as well, such as Cu-Zr [98]. Binary alloys were selected for this work in order to simplify the selection process and ensure segregation, since grain boundary enrichment is critical for nanoscale AIF formation in accordance with the first AIF selection rule. The prediction of segregation behavior in systems with multiple dopants is challenging, as the various dopants can compete for segregation sites and interact to influence the final microstructure [99]. In this study, we focus on binary systems in order to circumvent this complicating factor while still allowing for grain boundary enrichment.

Second, a large atomic radius mismatch between elements further hinders the formation of a crystalline structure by creating a high packing density in the amorphous structure, which impedes the free volume expansion necessary to form a crystalline structure [87, 97]. The atomic

radius mismatch is defined as the difference in the metallic bonding radii [100] of the elements in the binary metallic alloy divided by the radius of the smaller element, where a value greater than 12% is preferential for BMG formation [97, 101], as shown in Equation 6:

$$\Delta r/r = \left(r_{larger} - r_{smaller}\right)/r_{smaller} > 12\% \quad (6)$$

Third, a negative ΔH^{mix} creates a thermodynamically favorable landscape that reduces the rate of crystal nucleation [87, 97]. A negative ΔH^{mix} refers to an exothermic solution where energy is released upon mixing, meaning bonding between differing elements is favorable. Conversely, a positive value refers to an endothermic solution where bonding between like elements is favorable [102]. A common empirical signature of a negative ΔH^{mix} is the presence of many intermetallic phases on the equilibrium phase diagram.

Thus, alloys with positive ΔH^{seg} as well as negative ΔH^{mix} and atomic radius mismatch greater than 12% are promising candidates for AIF formation. Four Cu-rich, binary metallic alloys (Cu-Zr, Cu-Hf, Cu-Nb, and Cu-Mo) that exhibit dopant segregation and possess a range of ΔH^{mix} and atomic radius mismatch combinations were chosen in order to test these selection rules. Cu-Zr and Cu-Hf have a positive ΔH^{seg}, as calculated using the Miedema method [39]. Cu-Nb is also expected to have a positive ΔH^{seg}, due to previous modeling and experimental research that has shown Nb segregation and clustering at grain boundaries in Cu [103-105]. Experiments on Cu-Mo have shown that irradiation leads to Mo clustering at grain boundaries [106], also indicating a positive ΔH^{seg}. In addition, Atwater and Darling [107] calculated a theoretical minimum grain boundary energy caused by Nb and Mo added to nanocrystalline Cu, further suggesting a thermodynamic propensity for dopant segregation to lower the grain boundary energy. In order to examine the second half of our materials selection requirements (promotion of an amorphous structure), alloys were chosen with different thermodynamic parameters. Cu-Zr and Cu-Hf have

negative ΔH^{mix} values [108], whereas Cu-Nb and Cu-Mo have positive ΔH^{mix} values [43, 109]. Cu-Zr and Cu-Hf have several intermetallic phases with deep eutectics that can form whereas Cu-Nb and Cu-Mo do not [110], reflective of the ΔH^{mix} parameters in these systems. Additionally, all of the alloys except Cu-Mo have an atomic radius mismatch greater than 12%. Cu-Zr is a well-known glass former and was in fact the first binary BMG created [98], with evidence emerging that the high crystal-liquid interfacial free energy of this alloy is responsible for this behavior [111]. Cu-Hf has also exhibited reasonable glass forming ability [112].

As a result, we predict that Cu-Zr and Cu-Hf alloys can sustain nanoscale AIFs because dopant segregation is encouraged while favorable values of ΔH^{mix} and atomic radius mismatch promote the formation of an amorphous structure. Conversely, Cu-Nb and Cu-Mo are predicted to have ordered grain boundaries due to the low glass forming ability of these systems. Grain boundary segregation of the added dopants is expected in all four of the alloy systems. The key thermodynamic parameters and predictions are summarized in Table 2.2.

Alloy	**ΔH^{seg}**	**ΔH^{mix}**	**Atomic Radius Mismatch (%)**	**Grain Boundary Prediction**
Cu-Zr	Positive	Negative	25	AIF
Cu-Hf	Positive	Negative	24	AIF
Cu-Nb	Positive	Positive	14	Ordered
Cu-Mo	Positive	Positive	9	Ordered
Ni-Zr	Positive	Negative	29	AIF

Table 2.2. The thermodynamic variables and predictions for complexion type for the binary metallic alloys. Alloys with a positive ΔH^{seg} coupled with a negative ΔH^{mix} are predicted to have AIF formation. In contrast, those alloys having a positive ΔH^{seg} coupled with a positive ΔH^{mix} are predicted to have ordered grain boundaries. An atomic radius mismatch >12% promotes BMG formation and is also evaluated for its influence on grain boundary structure.

2.3.2 Characterization of Cu-rich Alloys

BF TEM images of the Cu-rich alloys after heat treatment are shown in Figure 2.1. All of the alloys exhibited equiaxed grains, with the average grain sizes and standard deviations presented in Table 2.1. Despite a deposition temperature of 400 °C, micrometer scale film thicknesses, a 500 °C anneal for 24 h, and an annealing step at $0.92T_{solidus}$ (all of which should promote grain growth), the Cu-Zr, Cu-Hf, and Cu-Mo films were still nanocrystalline with average grain sizes of 99 nm, 47 nm, and 85 nm, respectively. This is in contrast to pure Cu films deposited using similar deposition conditions which exhibited substantial grain growth. Cu-Nb also exhibited some amount of grain boundary stabilization, although to a lesser degree with an average grain size of 468 nm in the ultrafine-grained regime. EDS elemental maps were collected to provide a preliminary understanding of the degree of grain boundary segregation and dopant distribution experienced by each alloy, as shown in Figure 2.2 and Figure 2.3. Figure 2.2 shows the accompanying HAADF STEM image to the EDS map for Cu-Zr, highlighting how the dopant concentration values are highest at the grain boundaries. Both Figures 2.2 and 2.3 show that dopant concentration is inhomogeneous and that segregation to the grain boundaries occurs, in agreement with the positive ΔH^{seg} values for the four alloys.

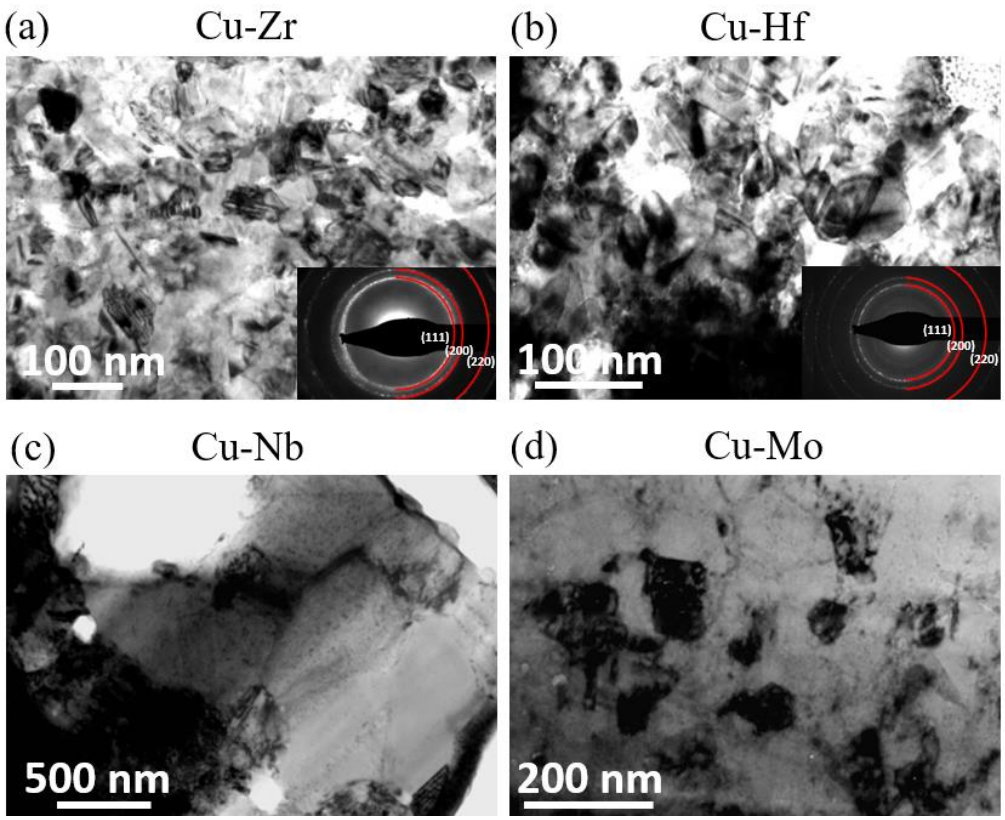

Figure 2.1. Bright field transmission electron microscopy images of the (a) Cu-Zr, (b) Cu-Hf, (c) Cu-Nb and (d) Cu-Mo films after completion of all heat treatment steps. The insets show the electron diffraction patterns for (a) Cu-Zr and (b) Cu-Hf, where only single phase face-centered cubic (fcc) diffraction rings are observed.

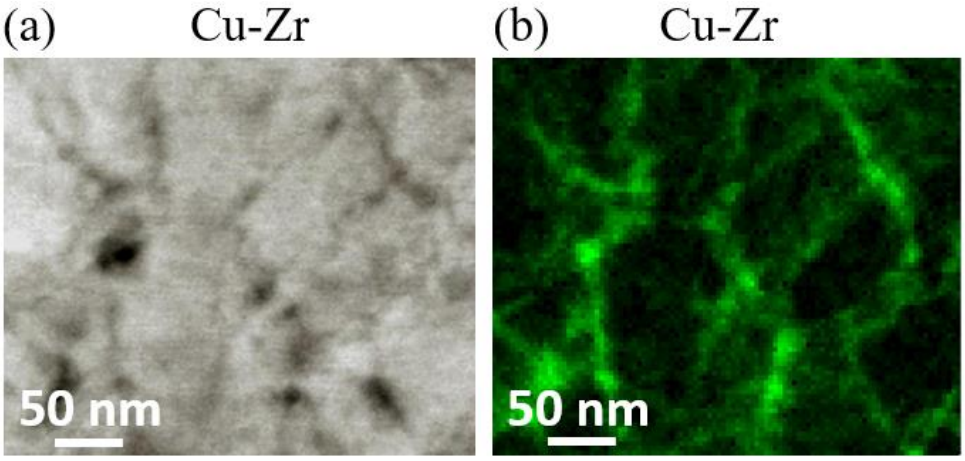

Figure 2.2. (a) shows a scanning transmission electron microscopy image, and (b) shows the corresponding compositional map of the (b) Cu-Zr alloy, after completion of all heat treatment steps. Green regions correspond to high Zr content, which is present at the grain boundaries.

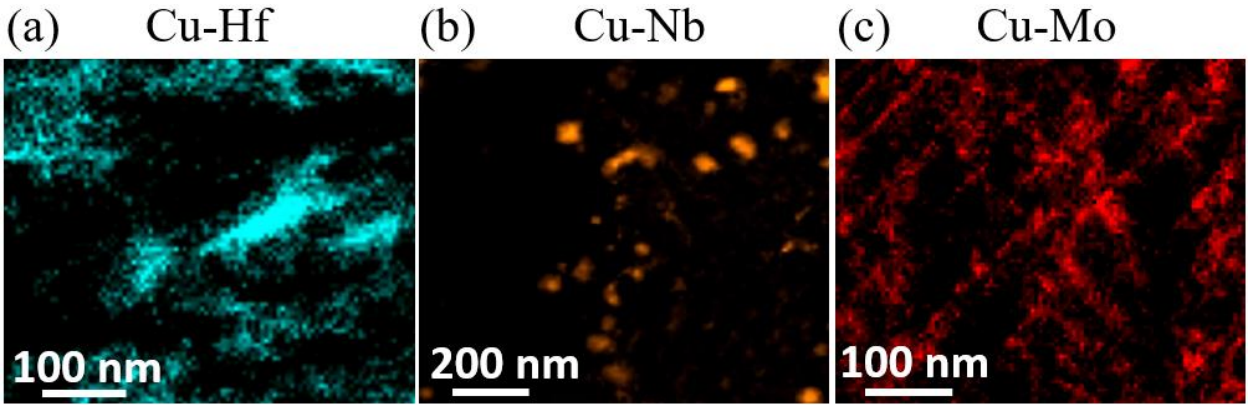

Figure 2.3. Compositional map of the (a) Cu-Hf, (b) Cu-Nb, and (c) Cu-Mo alloys, after completion of all heat treatment steps. Blue, orange, and red regions correspond to high levels of Hf, Nb, and Mo, respectively.

While all of the alloys experienced dopant segregation, the grain boundary structures differed significantly. TEM inspection of interfaces in the Cu-Zr and Cu-Hf system are presented in Figure 2.4. The SAED insets in Figures 2.1(a) and (b) confirm that the Cu-Zr and Cu-Hf films had no second phase precipitation, indicated by the presence of only the face-centered cubic (fcc) Cu diffraction rings in the pattern [113, 114]. Figure 2.4(a) shows an HRTEM image of a ~2 nm thick AIF in the Cu-Zr alloy, with Figure 2.4(b) displaying the accompanying EDS line profile scan for that grain boundary. The Zr segregation is evident in the line profile, reaching a maximum value of 7 at.% Zr and dropping to approximately 1 at.% Zr in the grain interior. It is important to note that the interaction volume of the electron beam is likely larger than the grain boundary thickness, meaning the maximum Zr composition measured is an average of the AIF composition and the crystalline material next to it. The segregation observed here is similar to the behavior reported by Khalajhedayati and Rupert [74] in a Cu-Zr alloy with AIFs that was created through ball-milling. Figures 2.4(c) and (d) present similar data for the Cu-Hf system, showing a 5 nm thick AIF that reaches a maximum dopant concentration of ~12 at.% Hf at the grain boundary but

then the composition drops down as the line profile extends into the neighboring grains. Again, the overall trend of dopant segregation to the grain boundary is clear.

Also presented in Figures 2.4(a) and (c) are fast Fourier transform (FFT) patterns taken from HRTEM images of the grain boundary films and the neighboring grains. The FFTs of the adjoining grains show periodic spots around the center point, indicating the presence of crystalline order, which also appears in the HRTEM image as lattice fringes. In contrast, the FFTs of the grain boundary film are featureless, confirming the presence of an amorphous region. The thickness of the films in Figures 2.4(a) and (c) are constant along the grain boundary, suggesting that the films are in thermodynamic equilibrium with the two neighboring crystalline grains and can be classified as nanoscale AIFs. Work by Dillon and Harmer [80] on complexions in Al_2O_3 showed that the thickness along a wetting film can change significantly and tended to be much thicker (>10 nm in many cases) than the films found here, lending additional confidence to the classification of these films as nanoscale AIFs and not amorphous wetting films. It is important to note that the thickness of the observed AIFs varied from boundary-to-boundary and that some interfaces even appeared ordered without an amorphous complexion. This variety of thicknesses was also observed in ball-milled Cu-Zr [66] and is likely due to variations in grain boundary character [115] as well as local fluctuations in Zr content.

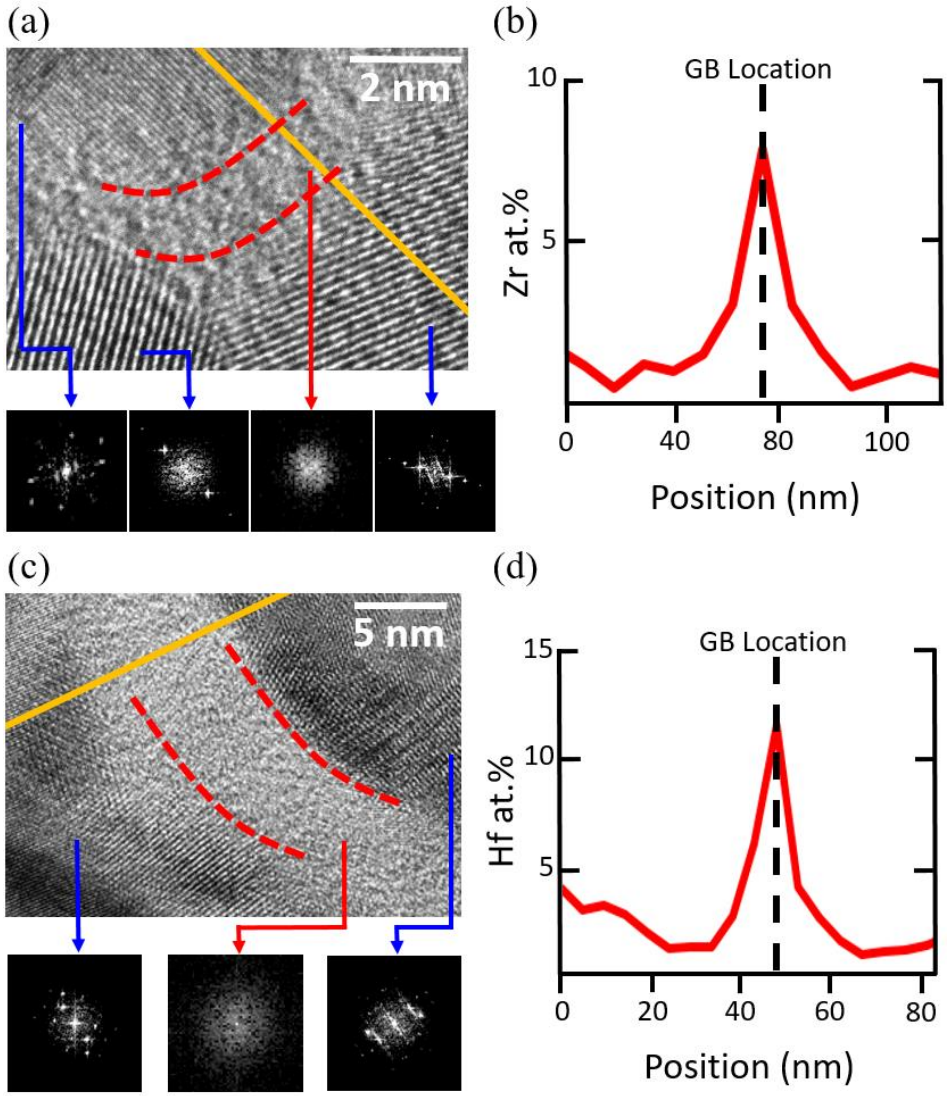

Figure 2.4. High resolution transmission electron microscopy images of amorphous intergranular films in the (a) Cu-Zr and (c) Cu-Hf samples, with fast Fourier transform images shown in the insets. Composition line profile scans across (b) the Cu-Zr sample and (d) the Cu-Hf samples are also shown. The yellow lines in (a) and (c) give the scan locations, with the grain boundary (GB) location marked on the line profiles in (b) and (d).

Figures 2.5 and 2.6 show HRTEM images and EDS line profiles of representative grain boundaries in the Cu-Nb and Cu-Mo systems. Both systems had only atomically sharp grain boundaries with ordered structures. No AIFs were found even after the inspection of many boundaries. Figures 2.5(b) and 2.6(b) show EDS line scans of Cu-Nb and Cu-Mo grain boundaries

with excess dopant being seen for each system, reaching 8 at.% Nb and 10 at.% Mo at the grain boundaries and dropping down inside the neighboring grain interiors. While dopant segregation was present at the grain boundaries, dopant-rich crystalline clusters were also found at both the grain boundaries and within the grain interiors for both alloys. For Cu-Nb, the clusters were typically ~30 nm in diameter. An HRTEM image of a Nb precipitate located at a grain boundary is shown in Figure 2.5(c), with the associated EDS line scan across the cluster in Figure 2.5(d), reaching a maximum value of 27 at.%. Nb. Cu-Mo formed smaller clusters that were ~5 nm in diameter. An HRTEM image of multiple Mo clusters is presented in Figure 2.6(c), with the associated EDS line scan across the cluster in Figure 2.6(d) showing a maximum composition of 17 at.% Mo. Again, it is likely that the compositions of the precipitates are higher due to the surrounding Cu being included in the beam interaction volume. The FFT insets in Figures 2.5(c) and 2.6(c) confirm the crystallinity of the clusters and neighboring grains. A summary of the grain boundary structures found in the Cu alloys is presented in Table 2.3.

Alloy	Dopant Segregation to Grain Boundary?	Complexion Type Found
Cu-Zr	Yes	AIF
Cu-Hf	Yes	AIF
Cu-Nb	Yes	Ordered
Cu-Mo	Yes	Ordered
Ni-Zr	Yes	AIF

Table 2.3. A summary of the final results for both the Cu-rich and Ni-rich systems. All of the systems experienced dopant segregation. Cu-Zr and Cu-Hf both had AIF formation, while Cu-Nb and Cu-Mo had ordered grain boundaries. Using this knowledge, Ni-Zr was predicted to contain AIFs, which was confirmed.

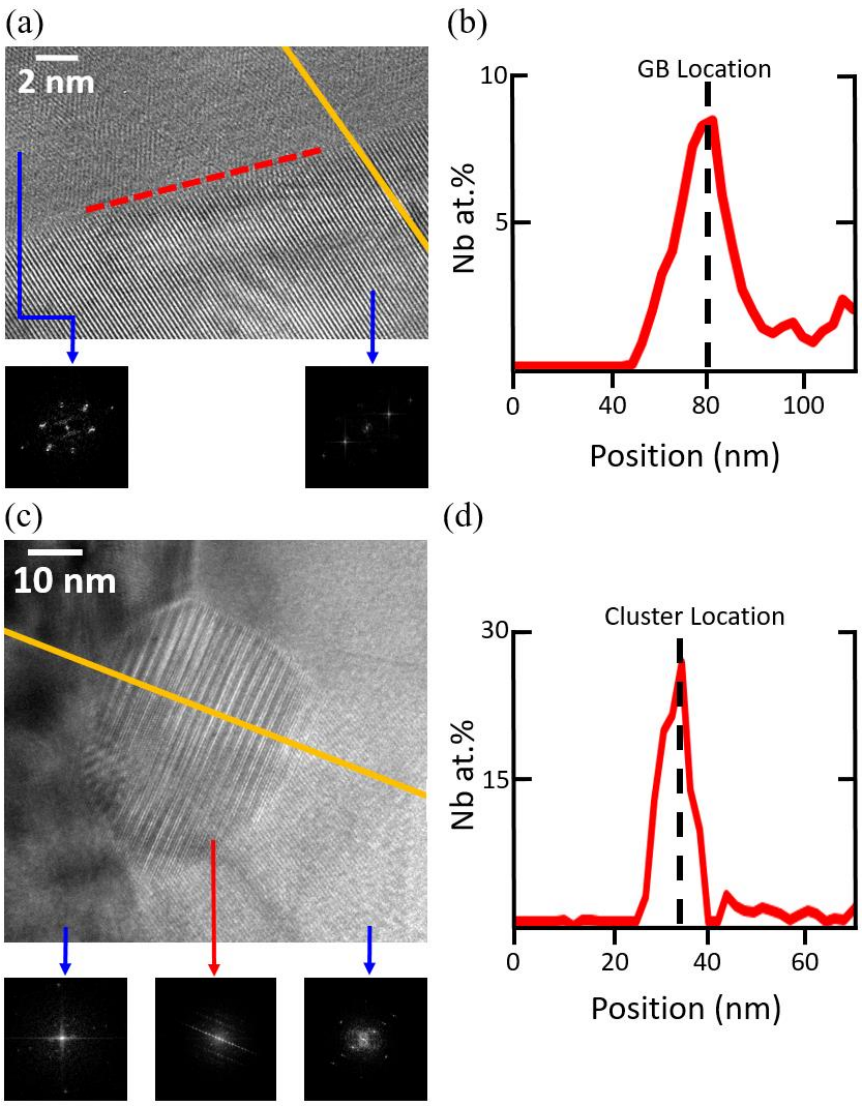

Figure 2.5. High resolution transmission electron microscopy images from Cu-Nb of (a) an ordered grain boundary and (c) a Nb-rich cluster located along a grain boundary. Fast Fourier transform images shown in the insets are sampled across the grain boundary film and the Nb-rich cluster, as well as the grain interiors. Compositional line profile scans are given across the (b) grain boundary and (d) Nb-rich cluster. The yellow lines in (a) and (c) give the scan locations, with the grain boundary (GB) and cluster location marked on the line profiles in (b) and (d) respectively.

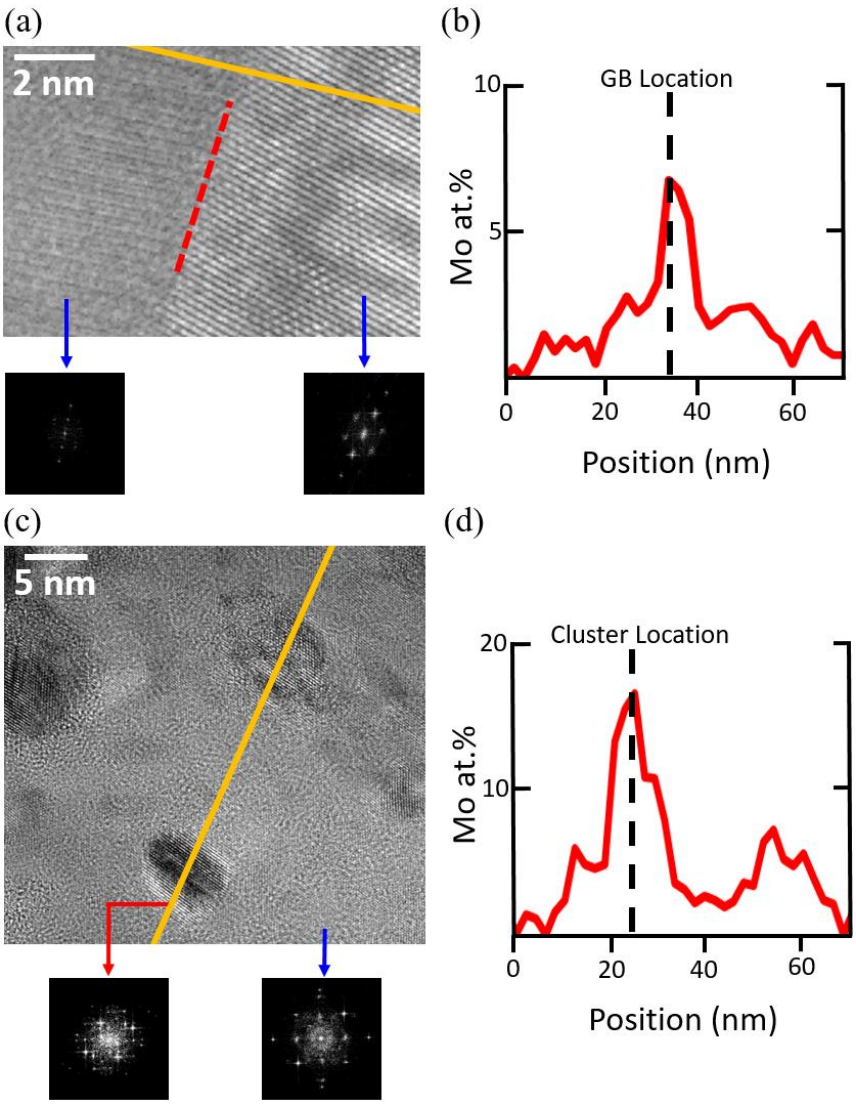

Figure 2.6. High resolution transmission electron microscopy images from Cu-Mo of (a) an ordered grain boundary and (c) a Mo-rich cluster. Fast Fourier transform insets are sampled across the grain boundary and Mo-rich cluster. Compositional line profile scans are given across the (b) grain boundary and (d) Mo-rich cluster. The yellow lines in (a) and (c) give the scan locations, with the grain boundary (GB) and cluster location marked on the line profiles in (b) and (d) respectively.

The efficacy of dopant segregation in stabilizing grain size was particularly evident in the Cu-Zr, Cu-Hf, and Cu-Mo films, which remained nanocrystalline despite processing efforts to increase the grain size for easier TEM inspection. Such grain size stability, at temperatures as high as $0.92T_{solidus}$, has been documented for Cu-Zr [74] but is a new observation for the Cu-Hf and

Cu-Mo systems. While stabilization through doping has been reported in systems such as Ni-W [50], Hf-Ti [116], and W-Ti [20], the annealing temperatures used were significantly lower than $0.90T_{melting}$ in these studies. Darling et al. [51] did report on a very stable nanocrystalline Fe-Zr alloy, with the stability attributed to Zr segregation. In the case of Cu-Zr and Cu-Hf shown here, it appears that stability at high temperatures is aided by AIF formation, since these features are the lowest energy structures available at such high temperatures and therefore fit into the thermodynamic theories of stabilization.

On the other hand, the Cu-Mo system is stabilized by a combination of grain boundary segregation as well as the presence of small precipitates, meaning both thermodynamic and kinetic stabilization are active. The kinetic contribution comes from Zener pinning caused by the dopant clusters [35, 52, 103, 117]. Clustering of Mo and the eventual precipitation of a second phase in a Cu-rich alloy has been previously reported due to the immiscibility of the added dopant [48, 103, 104, 106]. Similar behavior has been observed in Cu-Ta, an alloy system that also has a positive ΔH^{mix} and experiences dopant segregation [35, 47]. Finally the Cu-Nb alloy does not appear to be adequately stabilized, even though Nb segregates to the grain boundaries and precipitates do form. Kapoor et al. [103] also reported grain growth in Cu-Nb where the grain growth behavior was dependent on the Nb concentration, with lower percentages promoting grain growth. It is also possible that the larger size of the precipitates (tens of nm in diameter for Cu-Nb versus only a few nm in diameter for Cu-Mo) is responsible for the lack of stability, as a uniform distribution of many fine particles smaller than the critical precipitate radius is best for reducing grain boundary motion [118].

In summary, Cu-Zr and Cu-Hf both contained nanoscale AIFs after being quenched from a high annealing temperature, showing that a negative ΔH^{mix} and a large atomic radius mismatch

promote such features. As hypothesized in our design rules, it is also clear that a two component alloy is sufficient for stabilizing AIFs. The difference between AIFs (requires two elements) and BMGs (usually have three or more elements) can perhaps be attributed to the different length scales over which an amorphous structure must be stable. AIFs only require disorder of a nanoscale region, while BMGs require disorder that extends over mm length scales. This suggests that compositions that can sustain AIFs should be more plentiful than those which can be used for BMGs.

Cu-Nb and Cu-Mo both have positive ΔH^{mix} values, but these two alloys are differentiated by one key materials selection metric: the atomic radius mismatch. Cu-Nb has an atomic radius mismatch of 14% while Cu-Mo has a mismatch of 8.6%. Cu-Mo therefore achieves neither of the criteria needed to sustain an amorphous film and only has ordered grain boundaries as expected. Despite Cu-Nb satisfying one of the empirical rules for BMG formation, this alloy only exhibited ordered grain boundaries structures. When only looking at the results from our Cu-rich alloys, it is impossible to confirm whether both a negative enthalpy of mixing and a large atomic size mismatch are needed, or whether the negative enthalpy of mixing criteria is enough to predict AIF formation with atomic size being a secondary consideration. However, a detailed discussion of the available literature in the next section can clarify this point.

2.3.3 Extension of Materials Selection Rules to New Alloys

To make a final determination of our materials selection rules, it is necessary to examine a larger collection of literature reports. Table 2.4 shows a summary of binary metallic alloys that have exhibited behaviors which can be attributed to complexion formation. The longstanding mystery of grain boundary embrittlement has recently been solved and attributed to ordered

complexions in Ni-Bi [64], Cu-Bi [63], and Al-Ga [65] . These alloy systems have a positive ΔH^{mix} and therefore ordered complexions would be predicted, which agrees with experimental observations. Solid state activated sintering is typically attributed to the presence of AIFs and has been observed for certain Mo-rich and W-rich alloys [84, 95]. Inspection of Table 2.4 shows that all of the alloys which experience activated sintering, and therefore likely contain AIFs, have negative ΔH^{mix} values, but some of these materials do not have large atomic size mismatches (one of the empirical rules to enhance glass forming ability). This observation shows that the primary variable that increases the propensity for nanoscale AIF formation is a negative ΔH^{mix}, with a large atomic size mismatch perhaps being a secondary consideration. In contrast, activated sintering was not observed for W-Cu [84], which agrees with our prediction that only ordered boundaries would be present due to the positive ΔH^{mix} of the system.

Primary Element	Dopant	ΔH^{seg}	ΔH^{mix}	Atomic Radius Mismatch (%)	Observed Behavior	Complexion Structure
Ni	Bi	+	+	*	GB embrittlement [64]	Ordered
Cu	Bi	+	+	*	GB embrittlement [63]	Ordered
Al	Ga	+	+	*	GB embrittlement [65]	Ordered
Mo	Fe	+	−	10	Activated sintering [95]	AIF
Mo	Co	+	−	11	Activated sintering [95]	AIF
Mo	Ni	+	−	12	Activated sintering [95]	AIF
Mo	Rh	+	−	4	Activated sintering [95]	AIF
Mo	Pd	+	−	2	Activated sintering [95]	AIF
Mo	Pt	+	−	<1	Activated sintering [95]	AIF
W	Co	+	−	11	Activated sintering [84]	AIF
W	Ni	+	−	12	Activated sintering [84, 95]	AIF
W	Ru	+	−	4	Activated sintering [95]	AIF
W	Rh	+	−	4	Activated sintering [95]	AIF
W	Pd	+	−	2	Activated sintering [84]	AIF
W	Pt	+	−	<1	Activated sintering [95]	AIF
W	Cu	+	+	9	No activated sintering [84]	Ordered

Table 2.4. Additional binary alloys that have exhibited behavior that can be potentially attributed to amorphous intergranular film formation. All of the alloys have a positive ΔH^{seg}, meaning dopant segregation to the grain boundary is energetically favorable. Ni-Bi, Cu-Bi and Al-Ga have a positive ΔH^{mix}, which predicts an ordered grain boundary structure (confirmed experimentally) and has been attributed to boundary embrittlement. The Mo and W alloys (except W-Cu) have negative ΔH^{mix} and experience solid-state activated sintering, behavior which has been attributed to AIFs. In contrast, activated sintering has not been observed for W-Cu, which aligns with the positive ΔH^{mix} and ordered grain boundaries predicted for these systems. The atomic radius mismatch values calculated using the metallic bonding radii are also under 12% for many of the alloys that experience activated sintering and have AIFs, providing further confirmation that this parameter plays a secondary role in encouraging AIF formation. Those alloys with a (*) have potentially directional bonding which may influence the atomic radius mismatch calculation.

Inspection of the grain boundary structures in various Cu-rich alloys, as well as a critical review of literature data, allows us to finalize our materials selection rules. A positive ΔH^{seg} leads to dopant segregation while a negative ΔH^{mix} plus a large atomic size mismatch promotes AIF

formation, where a large atomic size mismatch may play a secondary role. To further show the utility of these rules, we next move to make and then test a prediction for Ni-rich systems. Ni-Zr is particularly promising, as it adheres to all selection criteria (see Table 2.2). Ni-Zr has demonstrated good glass forming ability and also experiences deep eutectics, similar to the Cu-Zr and Cu-Hf systems [119]. Ni-Zr has a positive ΔH^{seg} [39], a negative ΔH^{mix} [120], and an atomic radius mismatch of 29%. A Ni-5.5 at.% Zr alloy was deposited under similar sputtering conditions, with deposition details presented in Table 2.1. All annealing treatments followed those presented in the Methods section.

Figure 2.7(a) shows a BF TEM image of the Ni-Zr alloy after the various heat treatments. The inset gives the SAED pattern, with the Ni fcc rings being clearly visible and no other phases detected. Again, despite concerted efforts to induced grain coarsening, the average grain size remained in the nanocrystalline range at 41 nm. The EDS elemental map in Figure 2.7(b) highlights the segregation of the Zr dopant to the grain boundaries, confirming the positive ΔH^{seg} of the system. Figure 2.8(a) shows an HRTEM image of a 3 nm thick AIF in the Ni-Zr alloy, with Figure 2.8(b) displaying the accompanying EDS line profile scan for this interface. The line profile confirms the elevated Zr concentration in the AIF, reaching a maximum concentration of 21 at.% Zr and dropping back down once inside the grains. While this local percentage is in range for intermetallic formation according to the Ni-Zr phase diagram, no second phases were detected in the SAED pattern. The FFT images confirm the crystalline nature of the two grains and the amorphous nature of the intergranular film. Similar to the Cu-Zr and Cu-Hf systems, the thickness of the AIFs in Ni-Zr were always constant along a given grain boundary, pointing toward thermodynamic equilibrium of the film. Ultimately, the Ni-Zr system matched with the prediction that AIFs will form.

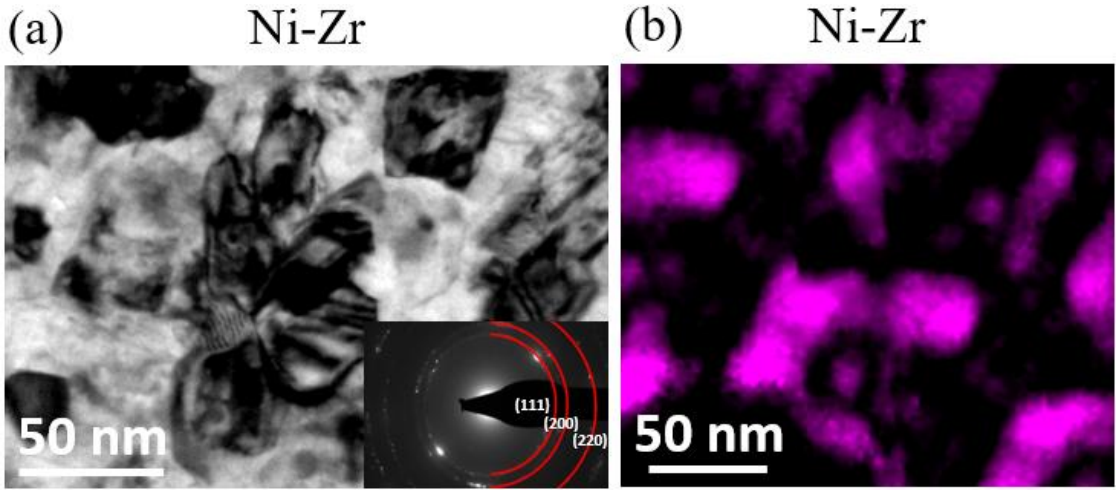

Figure 2.7. (a) Bright field transmission electron microscopy image of Ni-Zr after completion of all heat treatment steps, with an electron diffraction inset. (b) shows associated compositional mapping of the heat treated Ni-Zr with Zr denoted by pink.

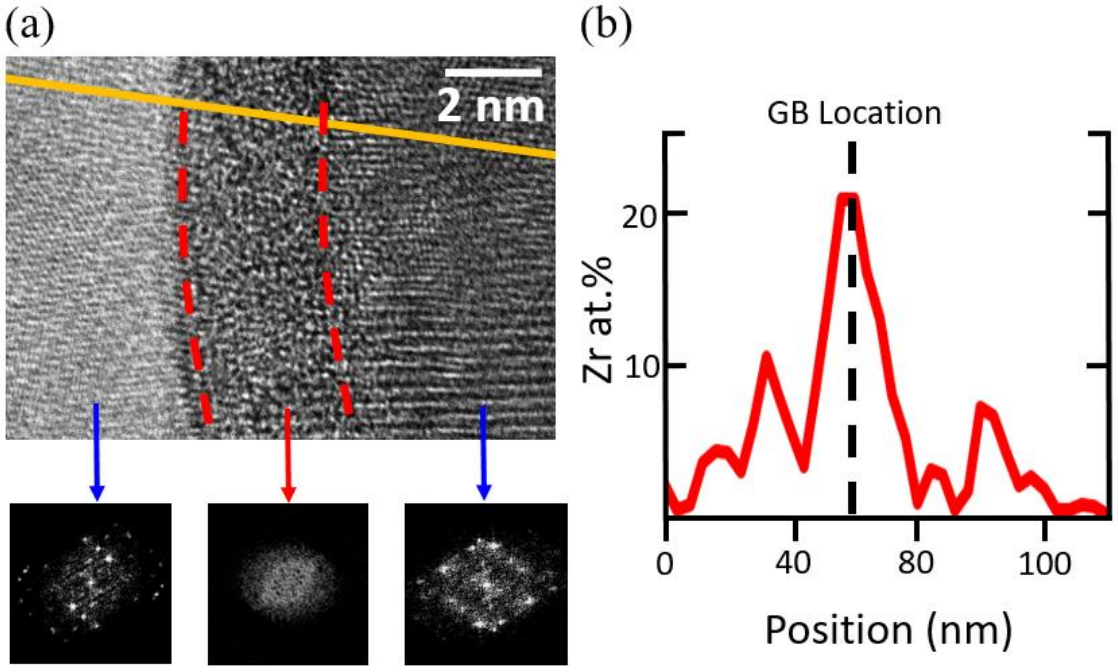

Figure 2.8. High resolution transmission electron microscopy image of (a) an amorphous intergranular film in Ni-Zr with fast Fourier transform insets sampled across the boundary structure. The compositional line profile scan across the amorphous intergranular film is shown (b). The yellow line in (a) gives the scan location, with the grain boundary (GB) location marked on the line profile in (b).

Our simple materials selection rules can also be used to make predictions for a wide variety of alloy systems. Using the ΔH^{seg} modeling estimations from Murdoch and Schuh [39] in conjunction with ΔH^{mix} calculated values from Atwater and Darling [107], we present a range of predictions in Table 2.5 for numerous binary metallic alloy combinations. Blue squares in this table have a positive ΔH^{seg} and a negative ΔH^{mix}, and are thus predicted to be possible nanoscale AIF formers. Red squares have a positive ΔH^{seg} and a positive ΔH^{mix}, and are thus predicted to have dopant segregation but only form ordered complexions. Gray squares have a negative ΔH^{seg} and are therefore predicted to have dopant depletion at the interfaces (i.e., dopants prefer to be located inside of the grains). Black squares indicate self-doping (e.g., Al in an Al lattice) or lack of available data to make a prediction. Other sources were also used to further confirm the enthalpy parameter values where applicable [35, 42, 95, 121-123]. It is worth noting that we do not explicitly treat any competition for dopants from second phase formation here, which can add an additional complication. It is possible that the magnitude of ΔH^{mix} may also be practically important, since very negative values may lead to intermetallic formation that removes dopants from the grain boundaries. Alloys with known ability to form metallic glasses are also particularly promising targets for AIFs and can be used to pinpoint some alloys with great potential. For example, Fe-Ti, Co-Nb, and Ni-Nb have demonstrated good glass forming ability [124, 125] as well as positive ΔH^{seg} and negative ΔH^{mix} values, and thus are excellent candidates to form nanoscale AIFs.

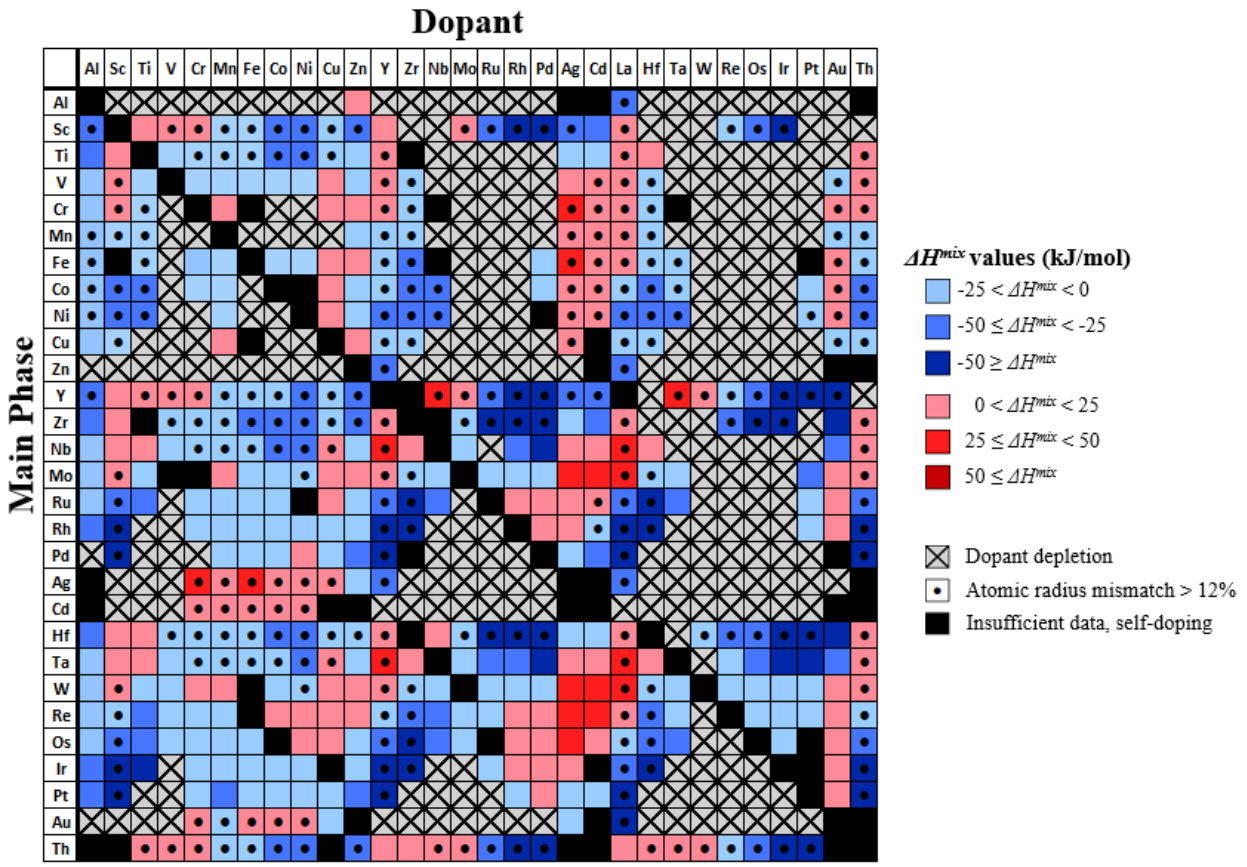

Table 2.5. Binary transition metal alloys evaluated for nanoscale AIF formation. Blue squares denote a positive ΔH^{seg} and a negative ΔH^{mix}, and are thus predicted to be possible AIF formers. Red squares have a positive ΔH^{seg} and a positive $\Delta H^{mix,}$ and are thus predicted to have dopant segregation and ordered complexions. Gray squares with an "X" have a negative ΔH^{seg} and are predicted to have dopant depletion at the grain boundary. Black squares indicate self-doping or lack of available data to make a prediction. A dot indicates the alloy has an atomic radius mismatch greater than 12%. The modeling calculation values for ΔH^{seg} are gathered from Murdoch and Schuh [39], while ΔH^{mix} values are gathered from Atwater and Darling [107].

It is worth noting that the predictive potential of Table 2.5 is only as good as the data used to find the thermodynamic parameters. We use the work of Murdoch and Schuh [39] and Atwater and Darling [107] because these are the most complete databases available, but these are not infallible. For example, the ΔH^{seg} modeling estimations for Cu-Nb and Cu-Mo indicate dopant depletion at the grain boundary, which contradicts the experimental data collected here for these

alloys. Thus, any interest in a particular system is best served by the accurate calculation or measurement of the ΔH^{seg} and ΔH^{mix} for that exact alloy.

2.4 Conclusion

In this study, a variety of binary Cu-rich alloys and their respective grain boundary structures were evaluated in order to define a relationship between material parameters and the ability to sustain nanoscale AIFs. Four alloys encompassing a range of parameter combinations (Cu-Zr, Cu-Hf, Cu-Nb, and Cu-Mo) were created using sputter deposition and processed to encourage dopant segregation to grain boundaries and grain boundary structure transformation. Analysis of the results from these alloys revealed a pattern of materials selection criteria to predict grain boundary composition and structure. These criteria were then applied to predict and confirm nanoscale AIF formation in Ni-Zr, as well as make predictions for a number of binary transition alloy combinations. The following specific conclusions can be made:

- ΔH^{seg} and ΔH^{mix} were found to be the primary determining factors behind the complexion type formed. Other factors that contribute to BMG stability, such as atomic radius mismatch and the usage of three or more elements are secondary at best and require further research to understand their role in AIF formation.
- A positive ΔH^{seg} coupled with a negative ΔH^{mix} promotes nanoscale AIF formation in polycrystalline binary metallic alloys. These AIFs were readily observed in Cu-Zr, Cu-Hf, and Ni-Zr.
- A positive ΔH^{seg} coupled with a positive ΔH^{mix} promotes ordered grain boundary complexions, where there is also the potential for dopant clustering and phase separation in this scenario. Cu-Nb and Cu-Mo demonstrated doped yet ordered grain boundary structures.

The key conclusion emerging from this study is the development of general materials selection rules for nanoscale AIF formation. Complexion type is determined by the presence of the required dopant element at the grain boundary and the ability of the grain boundary to assume the desired amorphous or crystalline structure. These findings can be leveraged to avoid undesirable material behaviors such as grain boundary embrittlement, and to realize improvements to material behavior such as increased damage tolerance, ductility, and accelerated diffusion.

Chapter 3: Amorphous Complexions Enable a New Region of High Temperature Stability in Nanocrystalline Ni-W

The contents of this chapter have been previously published as [126] J.D. Schuler, O.K. Donaldson, T.J. Rupert, Amorphous complexions enable a new region of high temperature stability in nanocrystalline Ni-W, Scripta Mater. 154 (2018) 49.

3.1 Introduction

Based on the materials selection rules introduced in Chapter 2, Ni-W would be expected to form AIFs at sufficiently high temperatures, with ΔH^{seg} = 10 kJ/mol and ΔH^{mix} = -3 kJ/mol [42]. This alloy system has been studied extensively in the past, with the unique feature that the grain size can be tailored during electrodeposition by controlling the reverse pulse current and, therefore, the W content [127, 128]. Prior work has shown that nanocrystalline Ni-W remains stable up to ~500 °C, primarily due to W grain boundary segregation [50]. However at higher temperatures Ni-W alloys have been observed to undergo rapid grain growth. Because of this rapid grain growth, most studies of thermal stability only extend to temperatures up to ~900 °C (see, e.g., [50]). While it appears that solute segregation-enabled stabilization breaks down by these temperatures, 900 °C is only ~60% of the melting temperature, meaning it is roughly at the lower limit of potential AIF formation. While AIFs have not been observed in Ni-W to date, we suggest that most studies have not gone to high enough temperatures. Moreover, very rapid quenching would be needed to freeze these features into the microstructure. Thus, we hypothesize that AIFs will form in Ni-W at sufficiently high temperatures, with the secondary hypothesis that these complexions will impact grain growth at these elevated temperatures. In this paper, the grain boundary composition and structure, as well as the grain growth behavior of nanocrystalline Ni-W, was analyzed at temperatures as high as 1200 °C. We find that Ni-W is indeed capable of sustaining AIFs, with these features observed above ~1000 °C. The AIF formation also creates a new region of high temperature grain size stability that had not been previously observed.

3.2 Material and Methods

20 μm thick nanocrystalline Ni-W films with 5-6 at.% W were created using the pulsed electrodeposition technique described by Detor and Schuh [128]. Deposition was performed on a >98 wt.% pure Ni substrate which had been mechanically polished to a mirror finish using a diamond suspension prior to deposition. A plating solution consisting of sodium citrate, ammonium chloride, nickel sulfate, sodium tungstate and sodium bromide was heated to a temperature of 75 °C. Cycles of forward current density at 0.20 A/cm^2 for 20 ms, and reverse current density at 0.20 A/cm^2 for 3 ms were applied between the Ni substrate and a commercially pure Pt mesh, the insoluble counter-electrode, for 1 h. The samples were encapsulated under vacuum in high purity quartz tubes, suspended in a vertically-oriented tube furnace during annealing, and then plunged into a water bath in under 1 s for quenching. The samples underwent rapid quenching to preserve any thermodynamically-stable states that are only accessible at elevated temperatures.

X-ray diffraction (XRD) was performed using a Rigaku SmartLab X-ray Diffractometer operated at 40 kV and 44 mA with a Cu Kα source. Profiles were analyzed using the Rigaku PDXL2 software, with grain sizes determined using the Scherrer equation on the (111) peak. Transmission electron microscopy (TEM) samples were created using the focused ion beam (FIB) lift-out technique on an FEI Quanta 3D FEG Dual Beam and FEI Nova 600 scanning electron microscope (SEM)/FIB. To reduce ion beam damage, all TEM samples received a final polish with a low power 5 kV beam. The global film composition was verified in the SEM using energy dispersive X-ray spectroscopy (EDS) operating at 30 kV. Grain boundary compositional analysis was performed in a JEOL 2800 TEM at 200 kV and FEI Tecnai G(2) F30 S-Twin at 300k V using EDS in conjunction with scanning, bright field, and high resolution TEM to inspect the grain size

and grain boundary structure. Phase identification was gathered under the same conditions using selected area electron diffraction (SAED). Grain size was calculated from bright field TEM images by measuring the areas of at least 50 grains and calculating the average equivalent circular diameter. Fresnel fringe imaging was used to identify interfacial films and ensure edge-on orientation of the grain boundaries during imaging [94].

3.3 Results and Discussion

First, a Ni-5 at.% W sample was annealed at 650 °C for 24 h, with the goal of coarsening the microstructure so that TEM samples only had one grain through the thickness, to allow for easy viewing of grain boundary structure. The sample was then heated to 1100 °C (~73% $T_{melting}$ for Ni-5 at.% W) for 10 min and then quenched. The grain structure is shown in bright field TEM images in Figures 3.1(a) and (b), where equiaxed grains are observed. No precipitates or second phases were detected in the film (Figure 3.1(c)). This is in agreement with the bulk Ni-W phase diagram, which predicts solid solution for compositions up to ~10 at.% W [129], even at high temperatures. The microstructure was further inspected using high resolution TEM and scanning TEM (STEM)-EDS to analyze the grain boundary structure and composition. Multiple AIFs with an average thickness of approximately 1 nm are shown in Figure 3.2. In Figure 3.2(c), the image has been digitally enhanced using a fast Fourier transform bandpass filter to smooth background variations down to 2 nm, so as not to disturb the presentation of the grain boundary structure. It is important to note that the AIF thicknesses are all constant along the length of the interface, which is indicative of nanoscale intergranular films in equilibrium at the grain boundary. In contrast, wetting films tend to be much thicker and have an arbitrary thickness that is dependent on the amount of available liquid phase [56, 80]. Moreover, the annealing temperature is below the

lowest eutectic on the Ni-W phase diagram, meaning it would be impossible for the grain boundary structure to come from a liquid phase.

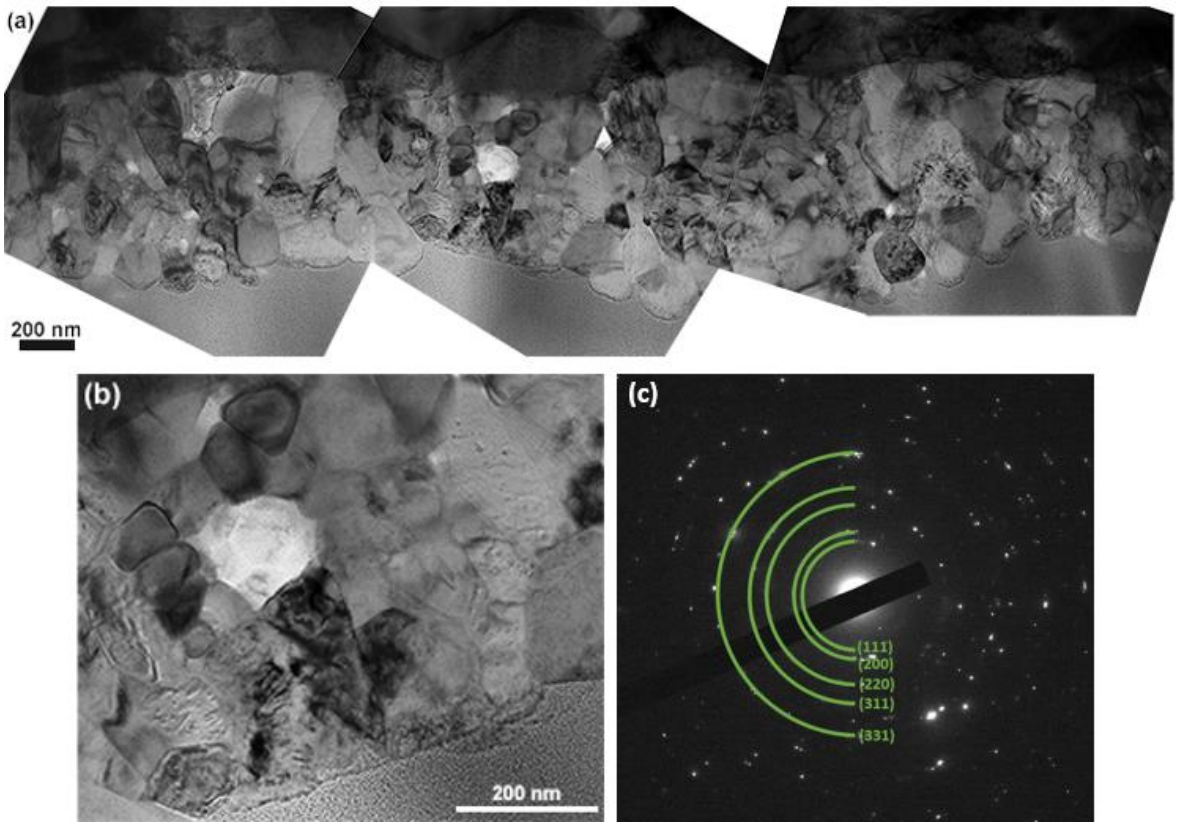

Figure 3.1. Bright field transmission electron microscopy images of nanocrystalline Ni-5 at.% W after a 24 h anneal at 650 °C and then a 10 min anneal at 1100 °C. (a) shows the overall film microstructure, while (b) shows a magnified image where equiaxed grains are observed. (c) The selected area electron diffraction pattern shows that only face centered cubic (fcc) Ni rings are present.

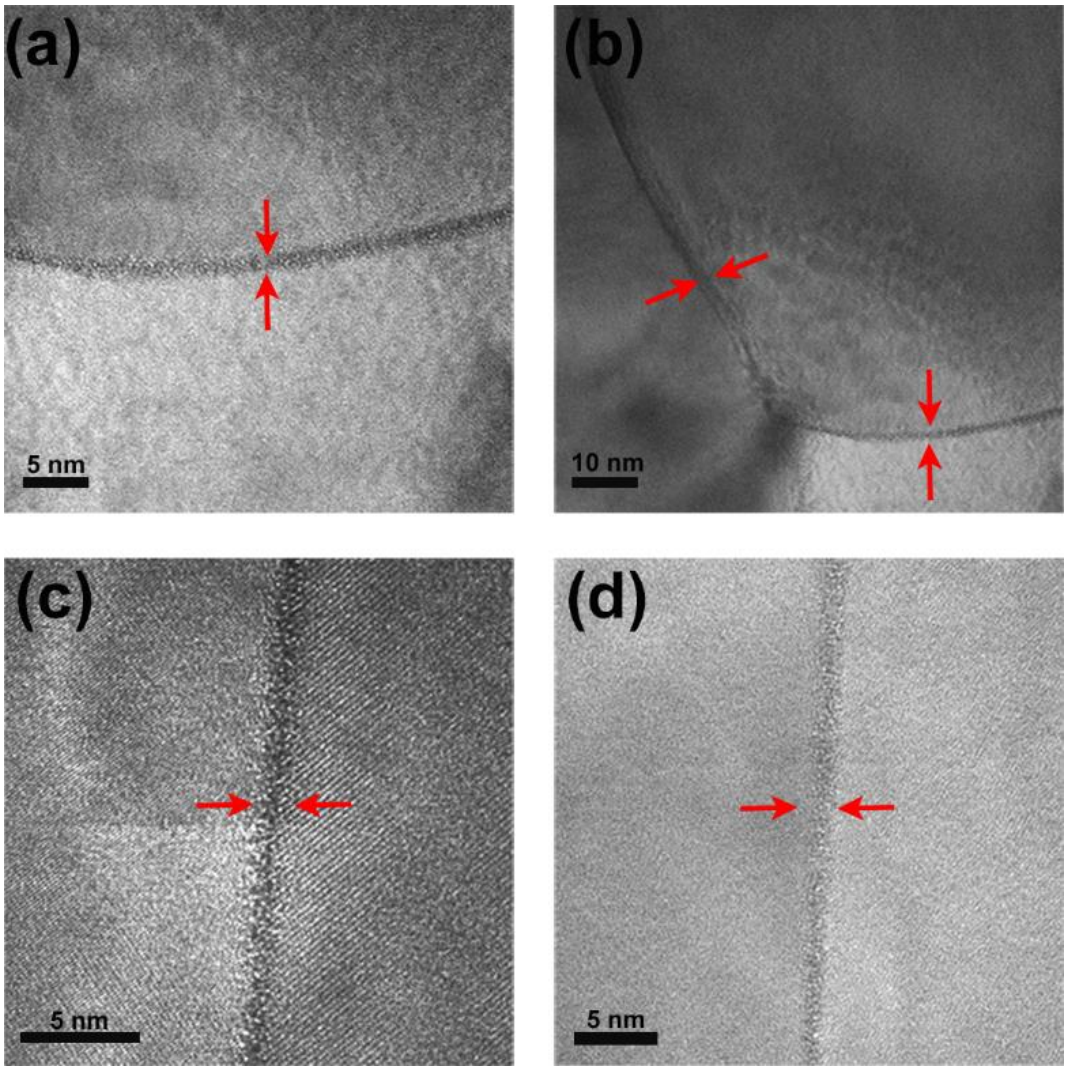

Figure 3.2. High resolution transmission electron microscopy images of ~ 1 nm thick amorphous intergranular films in the Ni-5 at.% W alloy after quenching from 1100 °C, with multiple examples shown in (a)-(c).

The EDS line scan across a grain boundary in Figure 3.3(b) with the associated STEM image in Figure 3.3(a) shows increased W composition at the grain boundary compared to the crystalline interior. While absolute EDS compositional values are subject to spatial averaging due to the beam interaction volume, W segregation is clearly observed. Only moderate W segregation is observed, which agrees with prior research where W was observed to be a weak segregator due to the significant solid solubility of W in Ni [50, 128]. The sample had an average grain size of 174 ±

54 nm, as shown in Figure 3.1(a) and (b). The large volume fraction of grain boundaries, approximately 1-2% [5], due to the grain size accommodates an elevated percentage of W dopant as reflected by Figure 3.3(b). While the grain interior composition is lower than 5 at.%, the significant volume of W-enriched grain boundaries accounts for the higher global average. If only the initial 650 °C annealing treatment is considered, our measured grain size would agree well with prior Ni-W annealing studies [50]. However, the primary differentiator here is the additional 1100 °C annealing treatment, which would be expected to cause rampant grain growth well beyond the measured value if trends from prior work were extrapolated. The absence of this rampant grain growth at very high temperature suggests that stabilization by AIFs may be occurring. To test this hypothesis, a detailed grain growth study was performed over a wide temperature range, going to higher temperatures than have previously been studied.

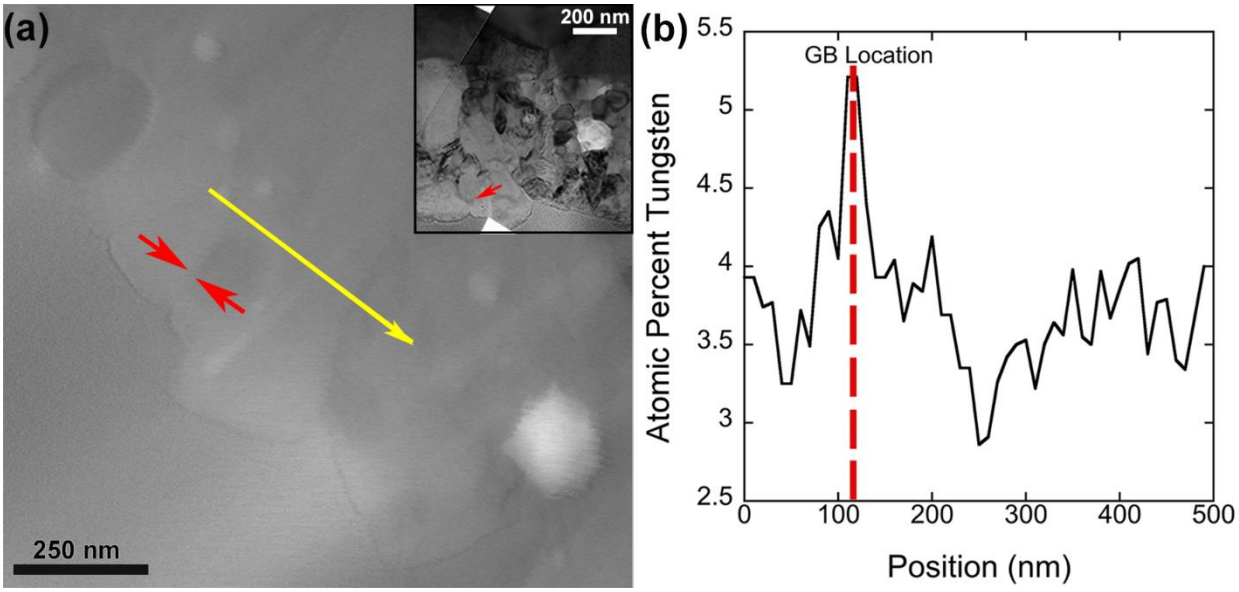

Figure 3.3. (a) Scanning transmission electron microscopy image of the Ni-5 at.% W alloy that was quenched from 1100 °C, with the associated bright field image shown in the inset. Red arrows in the scanning and bright field transmission electron microscopy images identify the boundary of interest, while the yellow line in (a) shows the scan location. (b) W concentration data demonstrates that W segregation occurs at the boundary.

A second set of similar Ni-W films were created with an initial average grain size of 35 ± 4 nm and a composition of 6 at.% W. Separate pieces of the film were then each subjected to 1 h annealing treatments at temperatures ranging from 200-1200 °C by inserting the sample at temperature followed by rapid quenching, with the resulting grain sizes plotted in Figure 3.4. Initially, negligible grain growth is observed up to ~600 °C, consistent with solute segregation serving as the primary stabilization factor to hinder grain growth [39, 49]. Annealing to 900 °C resulted in a 3-fold increase in the grain size, again consistent with previous observations [50, 130, 131]. However, the behavior that was observed at even higher temperatures was profoundly different than would be expected based on previous work. Further annealing to 1100 °C showed a secondary regime of stabilization with an average grain size of ~55-60 nm, indicating a significant deviation from expected grain growth trends. Finally, further annealing to 1200 °C yielded grain growth, with the grain size increasing rapidly.

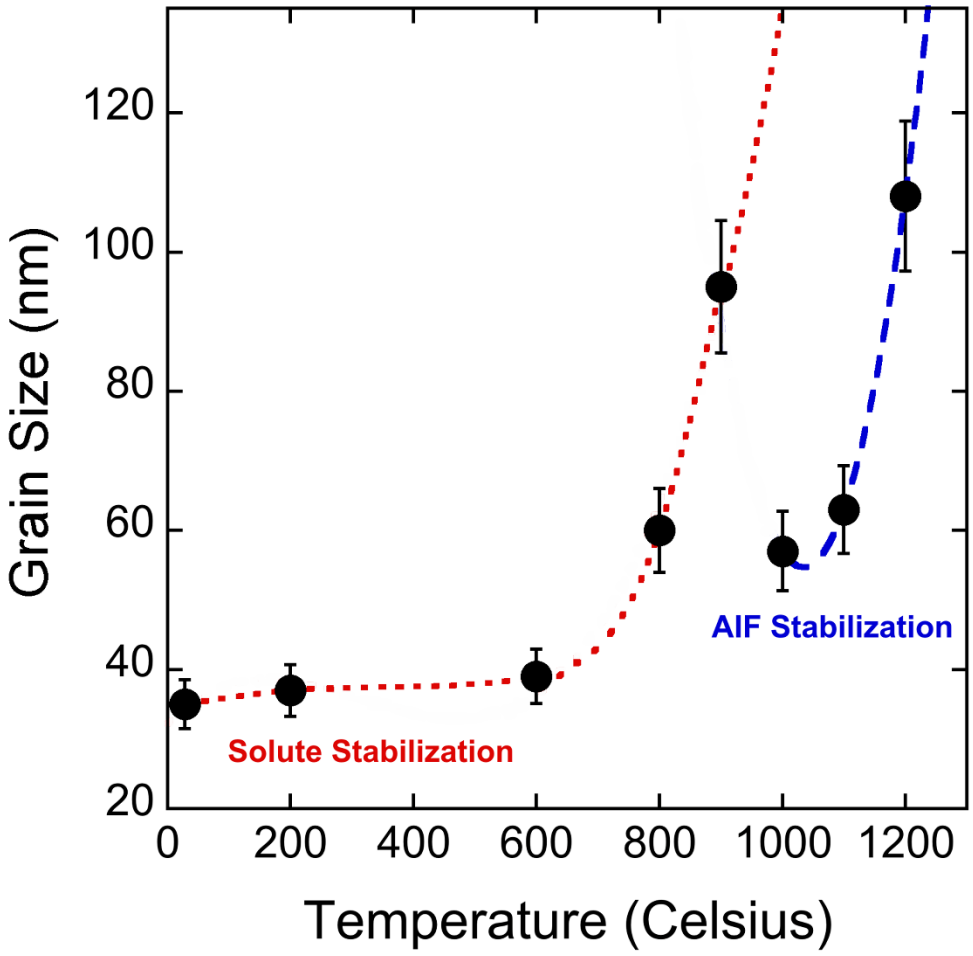

Figure 3.4. X-ray diffraction grain size analysis of the Ni- 6 at. %W electrodeposited alloys after annealing for 1 h at different temperatures. The data shows distinct regions of stabilization by solute segregation and amorphous intergranular film formation. Rough trend lines are added to guide the eye and highlight these two regions.

A higher bulk composition that correlates to more segregated dopant can increase complexion width and prompt ordered-to-amorphous structural transitions [59], and also enhance thermal stability [50]. The Ni-6 at.% W alloy could have slightly thicker and a larger volume fraction of AIFs with improved nanocrystalline stability compared to 5 at.%, but these differences are expected to be small. Thermodynamic treatments of complexion formation have suggested that AIFs become the preferred grain boundary structure after a threshold transition temperature [59,

132]. For Ni-6 at.% W, we find that this transition temperature is between 900 and 1000 °C (~60-67% $T_{melting}$). Interestingly, the formation of AIFs in a Ni film doped with W is similar to segregation-induced grain boundary premelting that was previously observed in W-1 at.% Ni [133]. Solid state activated sintering observed in the W-rich system was caused by Ni segregation to form amorphous grain boundary complexions. In this study, even though W is a weakly segregating dopant in Ni, it appears that the boundary composition is enriched enough to enable premelting at some grain boundaries. AIFs have also been observed in Cu-Zr [74], Cu-Hf [75], Ni-Zr [75] and Mo-Ni [134] binary alloys, all of which have a negative ΔH^{mix} [107] and exhibit dopant segregation, corresponding to the general AIF material selection guidelines put forth by Schuler and Rupert [75]. In addition, AIFs have been observed in materials made by a wide variety of processing routes, having been observed in sputtered [75], ball-milled [74], and sintered [135] materials. AIF formation is therefore a general phenomenon that can occur in a wide range of materials, including Ni-W where such features had not been observed previously. We suggest that AIFs have not been seen in prior works on Ni-W because either (1) heat treatments were not performed at high enough temperatures, (2) rapid quenching was not performed, or (3) detailed characterization of grain boundary structure was not performed.

3.4 Conclusion

In summary, electrodeposited Ni-W samples were analyzed to test the hypothesis that AIFs could form in this system. The Ni-5 at.% W sample demonstrated solute segregation and AIF formation, as well as a lack of dramatic grain growth even after annealing at 1100 °C. A similar sample set (electrodeposited Ni-6 at. % W), was annealed for 1 h at various temperatures up to 1200 °C, followed by rapid quenching, and two regions of grain size stabilization were observed. The first region coincides with solute segregation-enabled nanocrystalline stability which

eventually transitions to grain growth, which has been reported on extensively in past work. Upon reaching temperatures sufficient for AIF formation, a second, unexpected region of nanocrystalline stability is observed. The observation that nanocrystalline Ni-W has smaller grain sizes at higher temperatures disrupts conventional thinking on thermal stability. Ultimately, this study indicates that it is possible to stabilize nanocrystalline grains at temperatures higher than previously expected through a new method that utilizes AIFs.

Chapter 4: In Situ High-Cycle Fatigue Reveals the Importance of Grain Boundary Structure in Nanocrystalline Cu-Zr

The contents of this chapter have been previously published as[136] J.D. Schuler, C.M. Barr, N.M. Heckman, G. Copeland, B.L. Boyce, K. Hattar, T.J. Rupert, In situ high-cycle fatigue reveals importance of grain boundary structure in nanocrystalline Cu-Zr, JOM 71(4) (2019) 1221.

4.1 Introduction

While nanocrystalline metals, defined as having an average grain size less than 100 nm, have excellent structural properties such as high strength [137], hardness [138], and wear resistance [12], these properties are challenged by the most widespread mechanical failure: fatigue [139]. Nanocrystalline metals can usually achieve longer overall fatigue lifetimes compared to coarse-grained counterparts [140], but their weakness is limited resistance to crack growth and hence rapid failure following crack nucleation [141]. Fatigue lifetime in the high-cycle, low-amplitude regime can be considered in two stages as (1) crack initiation, followed by (2) crack propagation until sudden failure. Crack initiation in nanocrystalline metals has been shown to be preceded by abnormal grain growth and slip protrusions [142-144], whereas coarse-grained metal crack initiation relies primarily on persistent slip band activity [145]. Once initiated, cracks propagate through combinations of plasticity and interior crack formation that are dependent on the loading conditions and grain size [2, 146], driven by mechanisms such as dislocation nucleation and motion [147], deformation twinning [148], grain boundary migration [149], grain boundary sliding [150, 151], cooperative grain rotation [152], and cavitation [147]. Crack propagation in coarse-grained metals is resisted by tortuosity, plasticity, and roughness-induced crack closure, but these mechanisms all become suppressed with decreasing grain size [146].

Complexions are defined as thermodynamically-stable grain boundary features that can assume a range of ordered or disordered structures [56], where the disordered version with an equilibrium thickness is called an amorphous intergranular film (AIF). Nanocrystalline grain sizes

can potentially offer new opportunities by leveraging their associated large grain boundary volume fraction [5] through complexions. Nanocrystalline Cu-Zr alloys with AIFs have both increased strength and ductility compared to the same alloy with only conventional, ordered grain boundaries [66]. AIFs increase ductility and damage tolerance by diffusing the local strain concentrations at the grain boundary caused by dislocation absorption, which results in slower crack nucleation and growth [66, 68]. To date, this behavior has only been studied under monotonic loading scenarios, but it is hypothesized that a similar mechanism may also allow for improved fatigue behavior.

In this study, in situ transmission electron microscopy (TEM) fatigue was performed on nanocrystalline Cu-1 at.% Zr thin films processed to have either only ordered grain boundaries ("ordered grain boundary sample") or to contain AIFs scattered throughout the grain boundary network ("AIF-containing sample"). Microstructural analysis during crack initiation and propagation reveals grain growth at crack initiation with unstable crack growth and extensive nanocracking in the ordered grain boundary sample, whereas the AIF-containing sample had no grain growth at crack initiation with stable crack growth and distributed plasticity. Both samples were extrinsically toughened through grain bridging, while the more ductile AIF sample was also toughened intrinsically through crack tip plasticity mechanisms. By tuning grain boundary structure and composition, traditional extrinsic and intrinsic fatigue toughening mechanisms can be applied to resist crack propagation in nanocrystalline metals.

4.2 Materials and Methods

Cu-1 at.% Zr thin films were produced with magnetron co-sputtering using an Ar plasma with a Kurt J. Lesker Lab 18 modular thin film deposition system. The films were deposited at room temperature using 400 W for Cu and 46 W for Zr at 12 mTorr onto polished salt substrates. The films were then floated onto Protochips, Inc. Fusion heating chips through dissolution of the

salt substrate in a solution of water and isopropyl alcohol. Additional details describing the film deposition and sample preparation are provided in Appendix B.1. The films were annealed under vacuum using an Aduro double tilt heating holder in an FEI Tecnai G(2) F30 S-Twin 300 kV TEM. The samples were subjected to different heat treatments on separate heating chips in order to create the ordered grain boundary or AIF-containing samples. First, both samples were heated from 25 to 850 °C over the course of 1 h (ramp rate of 0.23 °C/s) and then held at 850 °C for 1 h. AIFs have been previously observed in ball-milled Cu-Zr alloys that were annealed at this temperature [74]. After the 1 h anneal, one sample was slowly cooled over the course of 600 s to 25 °C (cool-down rate of 1.4 °C/s) to create the ordered grain boundary sample. The AIF structure is only stable at high temperatures where grain boundary pre-melting occurs, so the slow cooling treatment allows these features to crystallize and form the typical ordered grain boundary structure. Alternatively, another sample was quickly cooled in <1 s by turning off the applied electrical current, which rapidly removes the heating input. Since the remainder of the heating chip is much larger than the sample itself, the specimen rapidly cools and "freezes" in any boundary structures that were stable at high temperatures (AIFs for these alloys) [153]. This rapid cooling step is analogous to quenching of powder samples that was used previously for ball-milled Cu-Zr [74]. Similar rapid quenching to freeze in an amorphous structure has also been used to create monatomic metallic glasses [154]. Bright field TEM, high resolution TEM, selected area electron diffraction (SAED), and scanning TEM energy-dispersive X-ray spectroscopy (STEM-EDS) were performed with a JEOL 2800 and JEOL 2100 operated at 200 kV. A film thickness of 51 ± 6 nm was measured for the as-deposited sample through electron energy loss spectroscopy (EELS) at 300 kV in a JEOL Grand ARM300CF, with additional EELS measurement details in Appendix

B.2. Average grain sizes were calculated from bright field TEM images by measuring the equivalent circular diameters of at least 100 grains from each sample.

The in situ TEM fatigue methodology was modeled after a prior study by Bufford et al. [155]. Electron transparent Single Edge Notched Tension (SENT) [156] specimens were prepared from the annealed thin films using a focused ion beam (FIB) lift-out technique with an FEI Nova 600 Nanolab FIB scanning electron microscope (SEM), where efforts were made to minimize inadvertent Pt deposition and FIB damage over the gauge area, both of which can impact mechanical behavior [157]. These specimens were then placed on push-to-pull (PTP) devices from the Bruker Corporation for testing. Additional details regarding mechanical testing sample preparation are provided in Appendix B.1. The PTP devices were actuated with a Bruker PI 95 TEM PicoIndenter holder in a JEOL 2100 operated at 200 kV at Sandia National Laboratories [158]. Tension-tension open loop fatigue was performed at 100-200 Hz with a staircase loading regimen [159] consisting of progressively increasing peak loads and amplitudes, with the full loading conditions provided in Appendix B.3. The loading conditions between the two samples were identical until final fracture of the AlF-containing sample, with the ordered grain boundary sample receiving continued progressive loading until fracture. While the final loading conditions differ between the two samples, our focus was on ensuring that the fatigue crack progressed so that we could understand the relevant deformation mechanisms for each material. The fatigue tests were performed with continuous video recording using a 680 nm × 680 nm field of view and an image capture rate of 15 frames per second in bright field TEM mode that was optimized for diffraction contrast. Note that during fatigue cycling, TEM images were blurred since the loading frequency was faster than the frame rate, with approximately 14 cycles captured per frame. In order to better capture the evolution of each sample, cycling was interrupted by periods of constant

load where cycling was stopped and the samples partially unloaded to capture clear images. All bright field TEM images of the fatigue specimen captured from the video have been rotated so that the loading direction is vertical, and crack propagation is from left to right.

4.3 Results and Discussion

Bright field TEM images of the ordered grain boundary sample and AIF-containing sample are shown in Figures 4.1(a) and (b), respectively, where the white arrow in Figure 4.1(a) indicates the loading direction. Figure 4.1(c) shows an SEM image of the sample preparation on the PTP device using Pt deposition. The brighter contrast over the gauge region indicates that the deposited thickness of the thin film is sufficiently thin as to be electron transparent. Experimental factors that are hard to control such as precise sample geometries, notch shape, specimen warp, internal film stress, changing grain imaging conditions, and imperfect Pt attachment at the gripper region limit the potential discussion of exact fatigue properties. Even within a given sample, specimen thickness variations preclude direct interpretation of quantitative data. However, differences in microstructural mechanisms and behavior during fatigue are investigated and reveal insight as to how AIFs can contribute to fatigue crack growth resistance. Bright field TEM images of the ordered grain boundary (Figure 4.1(d)) and AIF-containing (Figure 4.1(e)) samples are shown at the regions of interest immediately adjacent to the notch where crack initiation and propagation occurred. Locally thin regions are present in both films, which may be due to the sputter deposition process [160], grain boundary grooving, or preexisting inhomogeneities. The average grain size of the ordered grain boundary sample is 43 ± 11 nm, while the average grain size of the AIF-containing sample is 46 ± 14 nm, meaning that only one or possibly two grains are through the film thickness. A few abnormally large grains at the notch, visible in Figure 4.1, are present prior to fatigue and are likely due to FIB-induced grain growth from notch creation [161]. The SAED

pattern insets in Figures 4.1(d) and (e) only have Cu face centered cubic rings, overlaid in blue, meaning no detectable second phase such as hexagonal close packed Zr or an intermetallic was observed. The film composition of 0.9 ± 0.3 at. % Zr was measured by averaging values across STEM-EDS line scans. Clear evidence of dopant segregation to the grain boundaries was not detected unlike previous Cu-Zr experimental studies [74, 75]. However, the solid solubility of 0.12 at.% Zr in Cu coupled with compositions near the EDS resolution lower limits may make dopant segregation in this study more subtle and difficult to measure than in previous experimental studies that used higher Zr doping percentages. The high resolution TEM image in Figure 4.1(f) shows an AIF from the quenched film that was identified through Fresnel fringe imaging [94] in edge-on conditions. AIF formation is dependent on the grain boundary energy, local chemistry, and quenching rate, so it does not occur at every grain boundary [56, 66]. Instead, AIF-containing samples have a distribution of complexion types, including both ordered and disordered grain boundaries.

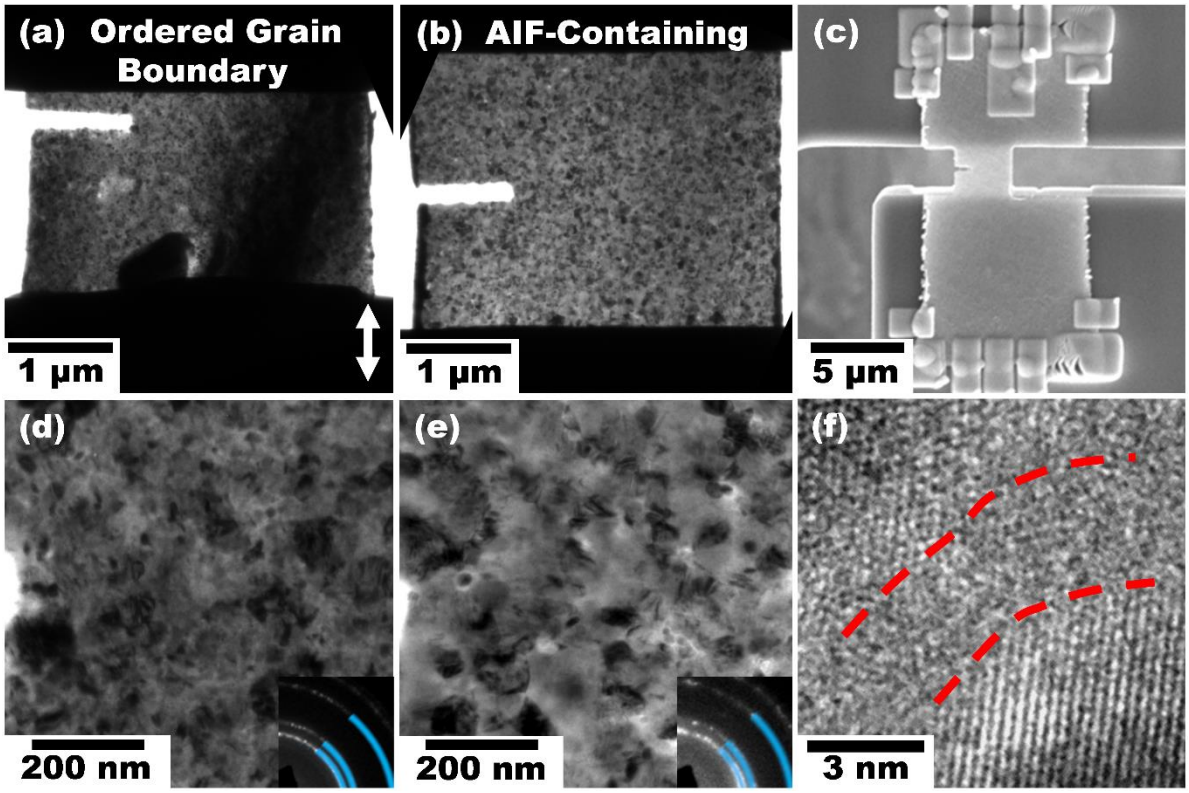

Figure 4.1. Bright field transmission electron microscopy (TEM) images of the Cu-1 at.% Zr films with (a) ordered grain boundaries and (b) amorphous intergranular films (AIFs). (c) shows scanning electron microscopy image of the fatigue sample preparation on the push-to-pull device. Bright field TEM images of the region adjacent to the notch (left) are shown for the (d) ordered grain boundary and (e) AIF-containing samples. The insets in (d) and (e) show the corresponding electron diffraction patterns with the Cu face-centered cubic rings superimposed in blue. (f) shows high resolution TEM image showing an AIF from the AIF-containing sample outlined by dashed red lines.

Analysis of crack initiation, the first stage of fatigue damage, is presented first. Crack initiation is defined as when a crack ingress has been observed beyond the FIB-created notch. In both the ordered and AIF-containing samples, the nanoscale fatigue cracks first initiated about one grain diameter (~20 nm) ahead of the notch, presumably due to the higher stresses ahead of the notch and/or weaker microstructural features to enable crack initiation. Grain growth preceded crack initiation in the ordered grain boundary sample, reminiscent of prior nanocrystalline metal fatigue studies [142-144], but grain growth was absent during crack initiation in the AIF-

containing sample. AIFs strongly resist grain growth, so much that even when nanocrystalline ball-milled Cu-Zr containing AIFs was held at 98% of its solidus temperature for a week, it remained nanocrystalline [74]. In fact, Schuler et al. [126] even observed a new regime of high temperature nanocrystalline stability due to AIF formation in Ni-W alloys. The ability of AIFs to both stabilize the grain size and diffuse local grain boundary strain concentrations may contribute to the absence of grain coarsening in the AIF-containing sample at fatigue crack nucleation. Figures 4.2(a)-(f) show crack initiation at the notch marked by the dashed line in the ordered grain boundary sample with progressive cycling in the loading direction indicated by the white arrow in Figure 2(a). The number of elapsed cycles is indicated in white at the bottom right of each frame. The grain denoted by the black arrows in Figures 4.2(a)-(f) more than triples in size from 12 nm to 41 nm. Although the grain growth is less dramatic than that observed in other nanocrystalline metal fatigue studies [142, 143, 155], this may be due to the maximum grain size being limited by the thin film thickness [162]. In the ordered grain boundary sample, black contrast features were observed to migrate during cyclic loading, particularly across the grains marked by the black and blue arrows in Figures 4.2(e) and (f). While the defect character was not determined due to the unknown beam condition and diffraction contrast, the contrast is consistent with dislocation-based plasticity [148, 160]. The red arrows in Figure 4.2(f) mark competing crack initiation sites where intergranular cracks have formed. The grain adjacent to the lower interior crack in Figure 4.2(f) eventually yields, allowing the intergranular crack to connect to the notch and commence crack propagation. In contrast, the AIF-containing sample shown in Figures 4.2(g)-(l) had distributed plastic activity evidenced by discrete microstructural contrast changes surrounding the notch region until an internal crack marked by the red arrow in Figures 4.2(k) and (l) formed at a microstructural feature. The adjacent grain indicated by the blue arrow in Figures 4.2(k) and (l)

eventually breaks away, connecting the internal crack to the notch to allow crack propagation. Such interior crack formation and nanocracking has been previously observed as a primary crack propagation mechanism in nanocrystalline metals [146, 148, 163], where void formation at grain boundaries and triple junctions ahead of the main crack contribute to intergranular fracture [164].

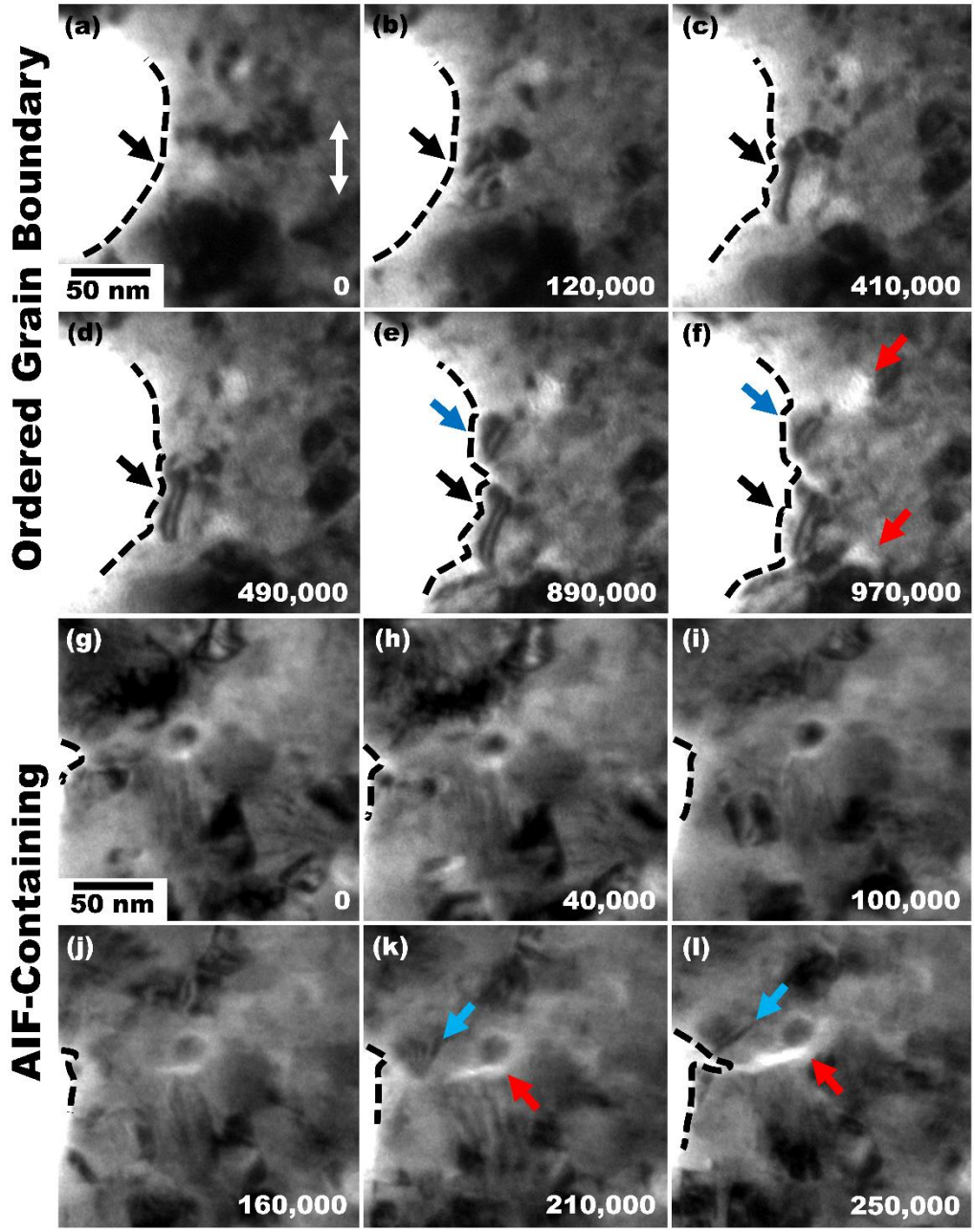

Figure 4.2. Bright field transmisison electron microscopy images of the (a)-(f) ordered grain boundary and (g)-(l) amorphous intergranular film (AIF) containing samples that show crack initiation with progressive cycling, where the number of elasped cycles is indicated in the bottom right. The dashed lines show the notch. The black arrows in (a)-(f) identify a grain that grows with cycling and where crack initiation eventually occurs, while the blue arrows show a competing crack initiation site. The red arrows in (f) indicate intergranular cracks formed in front of the notch at the competing crack initiation sites. The blue arrows in (k) and (l) indicate a grain that plastically deforms and yields due to the nucleating crack, and the red arrows show an interior crack formed in front of the notch. The white arrow in (a) shows the loading direction.

Crack propagation, the second stage of fatigue lifetime, is analyzed next. Grain bridging is defined as when a grain spans the opposing fracture surfaces in the crack wake, dissipating energy that would have extended the crack tip [165, 166]. A network of nanocracks and grain bridging events cause unstable crack propagation in the ordered grain boundary sample, whereas the AIF-containing sample had steady crack propagation punctuated by a series of nanocracks that ultimately connect to cause failure. Crack progressions captured from video frames are shown in Figures 4.3(a)-(f) for the ordered grain boundary sample and Figures 4.3(g)-(l) for the AIF-containing sample, with the number of elapsed cycles in the loading direction indicated in the bottom right corner of each image. Relative motion of microstructural features in both samples visible in Figure 4.3 may be due in part to global elongation caused by creep from the extended time under tension necessary to reach high-cycle fatigue. Similar microstructural shifts were also observed by Bufford et al. [155] during in situ TEM Cu high-cycle fatigue. The last frames before failure for the ordered grain boundary sample (Figure 4.3(f)) and AIF-containing sample (Figure 4.3(l)) show the ordered grain boundary sample failing during constant loading between cycling steps and the AIF-containing sample failing during active fatigue cycling, which causes the image to be blurry.

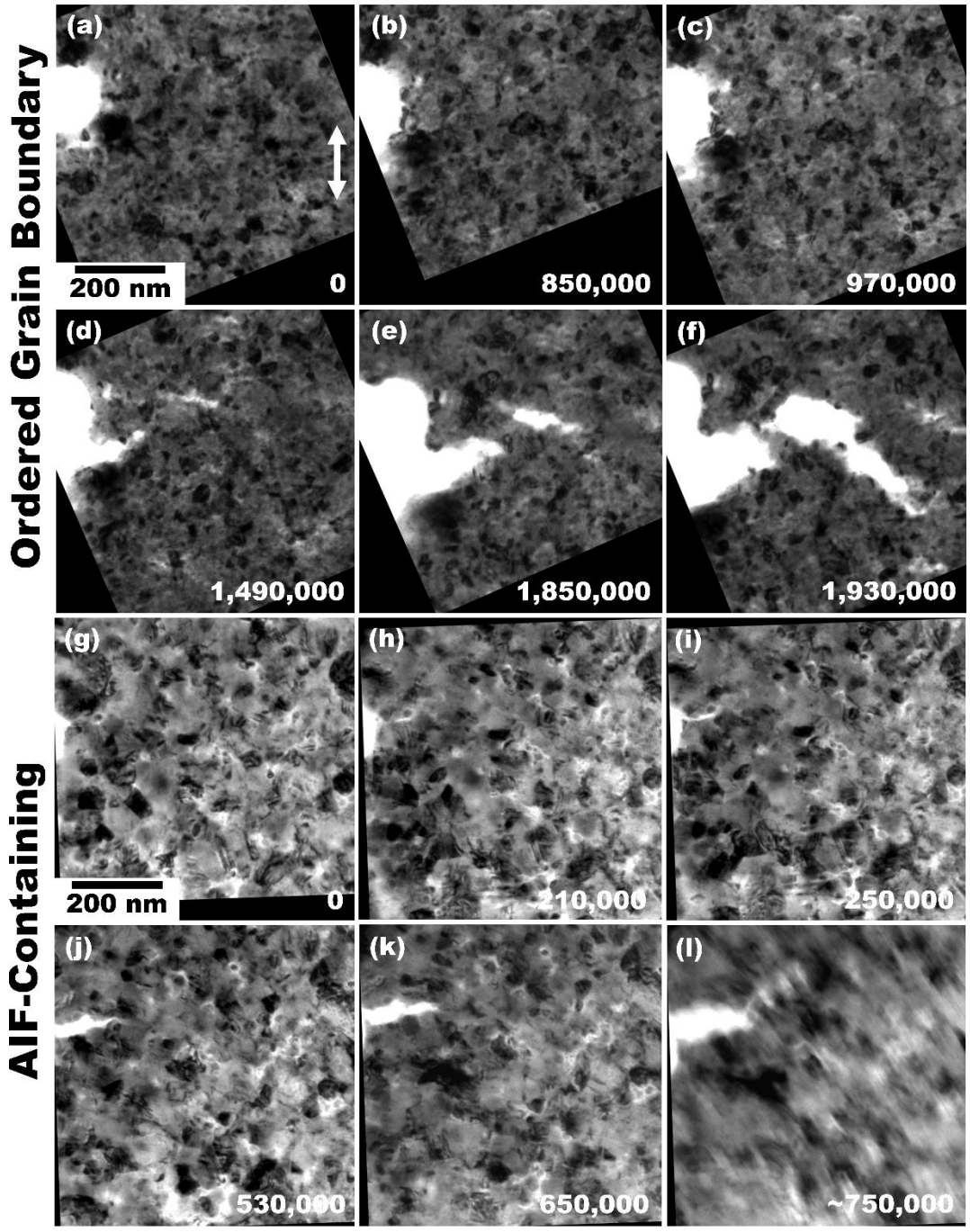

Figure 4.3. Bright field transmission electron microscopy images of the (a)-(f) ordered grain boundary and (g)-(l) amorphous intergranular film (AIF) containing samples showing crack propagation with progressive fatigue cycling, where the number of elapsed cycles is indicated in the bottom right. The white arrow in (a) shows the loading direction. The last frame before failure is shown in (f) and (l), where the (f) ordered grain boundary sample failed during constant loading between fatigue cycling and the (l) AIF-containing sample failed during fatigue cycling, causing the image to be blurry.

Unlike early fatigue studies in the TEM [167], the recently developed nanoindentation-based capability permits quantitative measurement of the driving force and crack advance throughout the fatigue test. From the measured forces and estimates for sample dimensions, it is possible to calculate approximate values for the plane stress linear elastic stress intensity range during fatigue loading. After the first 100 nm of propagation, the crack is expected to have escaped the influence of the ~90 nm notch radius and a rudimentary estimate of the stress intensity factor for the clamped SENT geometry is possible [168]. The crack tip is defined as the furthest ingress of the crack. Note that the crack tip could be a nanocrack with bridging grains in its wake [169]. For the AIF-containing specimen at a total crack length of 1.1 μm (for notch plus crack length a, which we note is a definition used only for this exercise, and specimen width W, a/W=0.33), the 10 μN applied force amplitude corresponds to a stress intensity factor range of $\Delta K \sim 0.4$ MPa$\sqrt{\text{m}}$, well below the macroscopic fatigue threshold for Cu [170]. Direct in situ visual measurements of total crack length as a function of cycles shown in Figures 4.4(a) and (b) for the ordered grain boundary and AIF-containing samples respectively enabled a determination of the crack growth rate, with additional details provided in Appendix B.3. For these conditions, we measure a crack growth rate of 2×10^{-12} m/cycle for the AIF-containing sample. Given the yield strength of approximately 1 GPa [66], the corresponding plane stress monotonic plastic zone size is estimated to be in the vicinity of 35-65 nm, confirming small-scale yielding and a valid estimate of the plane stress K_I. This extremely low crack growth rate is comparable to the value reported previously for in situ measurements on pure Cu [155] and is a growth rate that is difficult to measure by other macroscopic test techniques. The low crack growth rate corresponds to a single lattice parameter of average crack advance every ~200 cycles. Consistent with direct observation, the crack grows intermittently, arresting and restarting at the atomic scale, in spite of the apparent monotonic

growth shown in Figure 4.4. The early crack growth rate for the ordered boundary specimen was even lower at ~5×10^{-13} m/cycle, in spite of a higher driving force ΔK ~ 1.2 MPa$\sqrt{m}$ at a crack length of 1.1 μm. Finally, the crack growth accelerates in the ordered grain boundary sample, consistent with an increasing driving force for propagation as the crack propagated and the loading conditions increased. In contrast, the AIF-containing sample showed an unexpected constant crack growth rate in spite of the increasing driving force associated with both a growing crack and increasing load amplitudes. The growth rate behavior during in situ fatigue loading of metals warrants further investigation, since the observations reported here are substantially different from those reported for bulk ultrafine grained Cu [170].

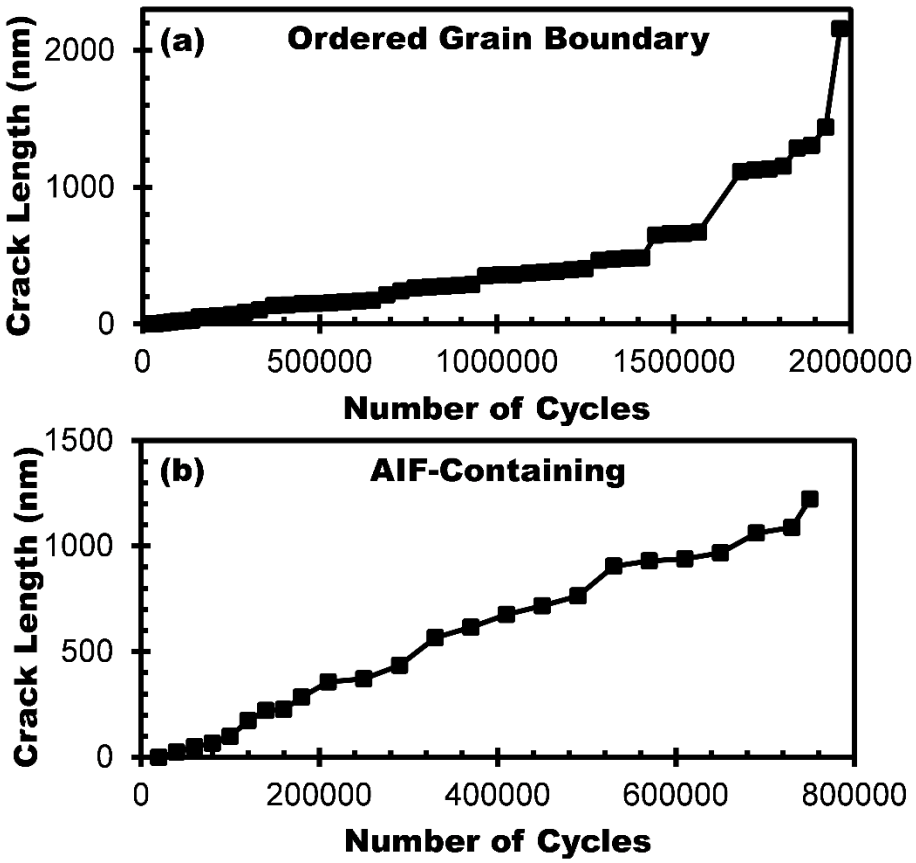

Figure 4.4. Crack growth beginning at the notch as a function of fatigue cycle for the (a) ordered grain boundary and (b) amorphous intergranular film (AIF) containing samples.

Plastic activity was identified dynamically through observation in the video in frame by frame analysis, where moving dislocations and grain boundaries differentiated from bend contours through their discrete and asynchronous motion [160]. Instances of plastic activity, which may include dislocation nucleation, dislocation movement, or grain boundary migration, as a function of distance from the advancing crack tip are shown as heat maps in Figure 4.5(a) for the ordered grain boundary sample and in Figure 4.5(b) for the AIF-containing sample. In this figure, activity closest to the crack tip is black and the farthest is white. The background bright field TEM images show the last clear frame before sudden failure for reference. The load amplitude for all except the first 160,000 cycles in both samples corresponds to ~50 nm of displacement, causing a 1 to 2 grain ambiguity in the recorded plastic activity locations, corresponding to a ~40-80 nm potential error in the position measurements. The crack tip coordinates were then found during constant loading conditions between cycling sets and used to calculate the linear distance from the plastic event to the crack tip position at the time of occurrence. Cycling steps 44, 45 and 53 for the ordered grain boundary and 23 for AIF-containing samples, as described in Appendix B.3, were not analyzed for plastic behavior due to excessive drift. Plastic events were then separated as being in front of or behind the crack tip, such as at a grain bridge. 75% of the total plastic events in the ordered grain boundary sample were in front of the crack tip compared to 98% of AIF-containing sample plastic events, signifying enhanced plasticity preceding the crack tip when AIFs are present. The heat maps show that plastic activity in front of the crack tip is concentrated along the path of crack advancement for the ordered grain boundary sample, with localized clusters at the point of initiation and where a grain bridge eventually occurs. In contrast, plastic activity in the AIF-containing sample is more evenly distributed and far in front of the crack tip. Figure 4.5(c) presents the position data from Figures 4.5(a) and (b) as cumulative distributions. One can pick

an arbitrary distance to understand the difference in the two distributions. For example, 50% of plastic activity in the ordered grain boundary sample occurred within ~130 nm from the crack tip, whereas 50% of plastic activity in the AIF-containing sample occurred within ~300 nm from the crack tip. Also, plastic activity only extended to ~600 nm from the crack tip in the ordered grain boundary sample, but reached up to 800 nm away in the AIF-containing sample.

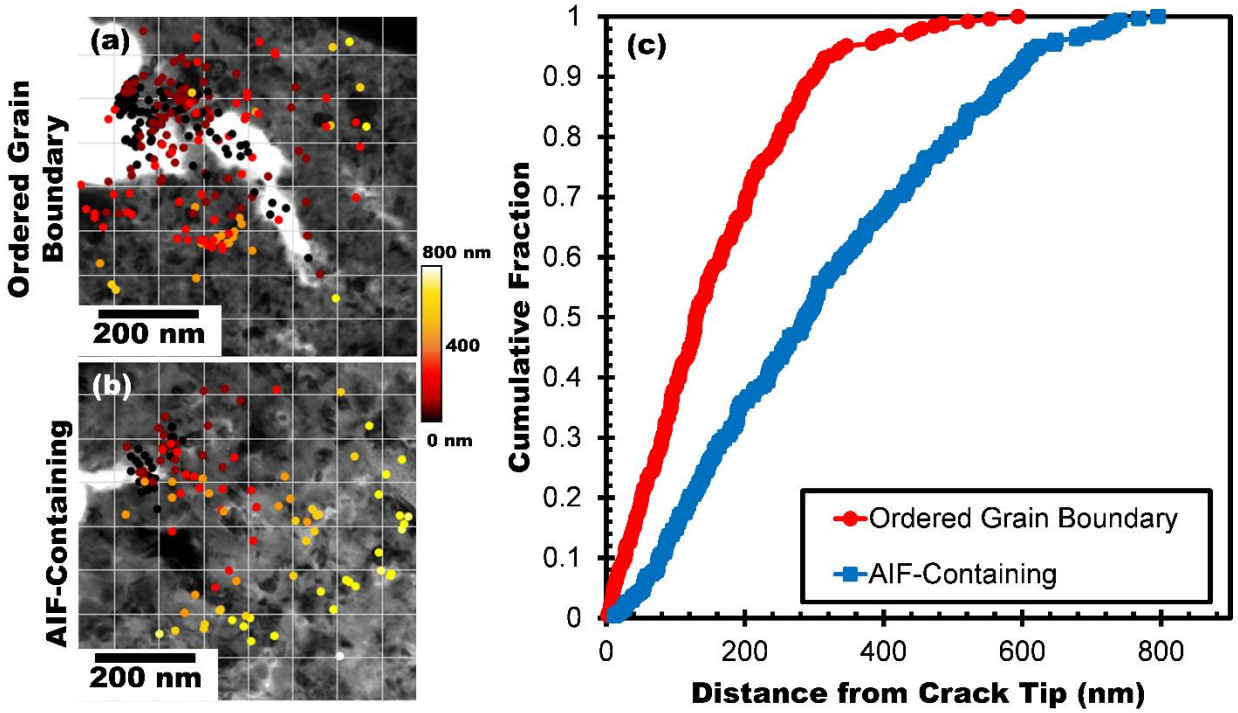

Figure 4.5. Heat maps of the (a) ordered grain boundary and (b) amorphous intergranular film (AIF) containing samples showing the location of plastic activity identified dynamically through the video in front of the advancing crack tip. The color gradient shows the distance of the plastic event from the crack tip at the time of detection, where black is closest and white is farthest. The backgrounds are bright field transmission electron microscopy images of the last clear frame before fracture for reference. (c) shows the cumulative distribution fraction of plastic activity as a function of the distance from the crack tip at the point of detection. The ordered grain boundary sample data is shown with red circles and the AIF-containing sample data appears as blue squares.

For the ordered grain boundary sample, very few plastic events were recorded at nanocracks outside of the main crack, suggesting these features likely formed through sub-critical

cleavage. Similar events were observed previously for sputtered thin films [160]. The extensive nanocrack network observed in the ordered grain boundary sample, but not the AIF-containing sample may be accounted for by the larger distribution of plastic activity in the AIF-containing sample. AIFs diffuse grain boundary strain, giving grain boundaries with these features a higher damage tolerance than a comparable ordered grain boundary [68]. The distributed plastic activity observed in the AIF-containing sample is likely due to AIFs mitigating boundary damage and allowing observable plastic activity to manifest, whereas the ordered grain boundary sample succumbed to nanocracking before having observable plastic activity.

The unstable crack propagation in the ordered grain boundary sample propagated through the formation of nanocracks and grain bridges. The evolution of one such grain bridge with progressive cycling is shown in Figure 4.6(a) for the ordered grain boundary sample. The red arrow marks a grain that sustained considerably localized plasticity and has grown across the grain bridge, serving as the point of eventual detachment. While the AIF-containing sample also had grain bridging, it was accompanied by significant crack tip plasticity with steady crack propagation. Bright field TEM images of the AIF-containing sample in Figure 4.6(b) shows a distinct “V” shape preceding the crack tip, with one example indicated by the red arrows, which may be a blunted crack or plastic hinge caused by local thinning and deformation from strain fields ahead of the crack tip [171-173], or movement of material through dislocation emission and absorption between nearby grain boundaries and the advancing crack tip [2]. The plastic deformation zone was also confined to the grains located immediately in front of the crack tip, indicating that possible slip transfer was limited by factors such as grain boundary character, slip system orientation, and angle of crack deflection [160, 174-177].

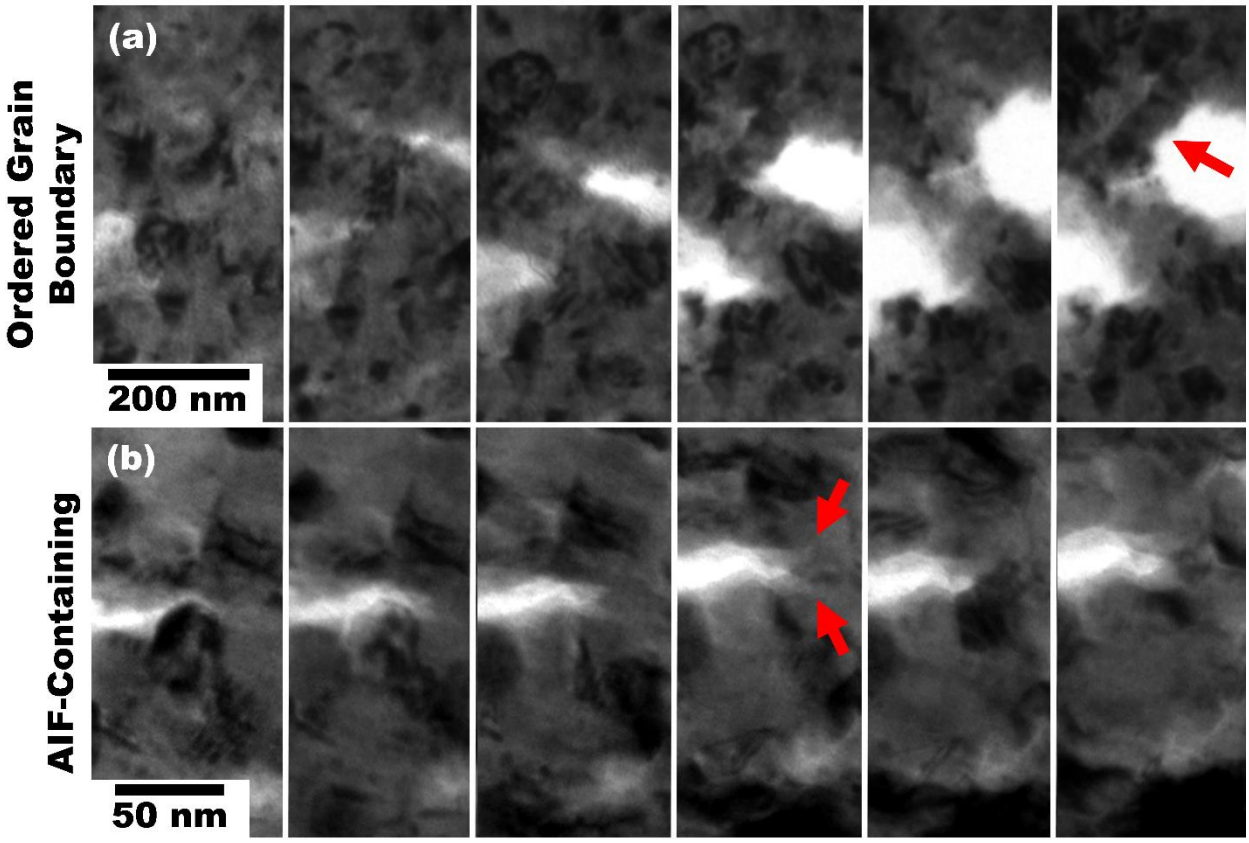

Figure 4.6. Bright field transmission electron microscopy images of the (a) ordered grain boundary and (b) amorphous intergranular film (AIF) containing samples showing the evolution of microstructrual events that occurred in each film during fatigue. A grain bridging event in the ordered grain boundary sample that sustained substantial plastic activity is visible in (a), where the grain indicated by the red arrow grew across the bridge and served as the eventual point of detachment. The plastic deformation zone in front of the crack tip of the AIF-containing sample appears in (b), where a distinctive "V" shape preceding the crack is highlighted by the red arrows.

Next, analysis of the fracture surfaces post failure is presented. Tortuosity can be defined as the ratio between the total crack length and the distance between the crack starting and ending points, excluding the notch [178]. Propagation refers to the stage of crack growth after initiation until the critical length that causes sudden, uncontrolled failure is reached. Failure refers to the portion of the fracture surface formed after the propagation stage at sudden failure. Saw-toothing is defined as individual grains that undergo severe local plastic deformation and become ligaments until finally necking down to a point [148]. Bright field TEM images of the fracture surfaces are

shown in Figure 4.7 for the ordered grain boundary and AIF-containing samples. The dashed red lines mark the start of the propagation stage where crack nucleation occurs on the left and the crack propagates to the right. The solid blue lines mark the end of the propagation stage and the commencement of sudden failure. The fracture surfaces from the failure stages are shown in greater detail for the ordered grain boundary and AIF-containing samples in Figures 4.7(c) and (e), respectively, with the outlines of the fracture surfaces shown in Figures 4.7(d) and (f) to help guide interpretation. The crack deflection segment lengths, deflection angles, and tortuosity measurements from the fracture surfaces for each stage are presented in Table 4.1. The larger average deflection angle in the failure versus propagation stage for both samples can be attributed to saw-toothing that was only observed in the failure stage, as shown in Figures 4.7(c) and (e). The mean deflection lengths are on the same scale as the grain size, with good alignment between mating surfaces excluding saw-toothed regions [179]. The tortuosity is comparable between all stages, except the propagation stage in the AIF-containing sample that is significantly smoother with almost no measurable tortuosity. Fracture modes due to cyclic loading differ from monotonic loading conditions when crack tip plasticity is appreciable. Since plasticity is largely absent from brittle materials, the fracture surface morphologies subject to cyclic or monotonic loads will be similar in classically brittle materials such as ceramics [139]. The difference in tortuosity between the propagation and failure fracture surfaces observed in the AIF-containing sample are therefore another sign of enhanced ductility.

	Avg. Deflection Length (nm)		Avg. Deflection Angle (°)		Tortuosity	
	Propagation	**Failure**	**Propagation**	**Failure**	**Propagation**	**Failure**
Ordered Grain Boundary	37.7	34.3	68.8	83.3	1.53	1.53
AIF-Containing	46.2	38.9	58.9	82.2	1.01	1.52

Table 4.1. Fracture surface analysis of the ordered grain boundary and amorphous intergranular film (AIF) containing samples from the propagation and failure stages of the fatigue crack lifetime.

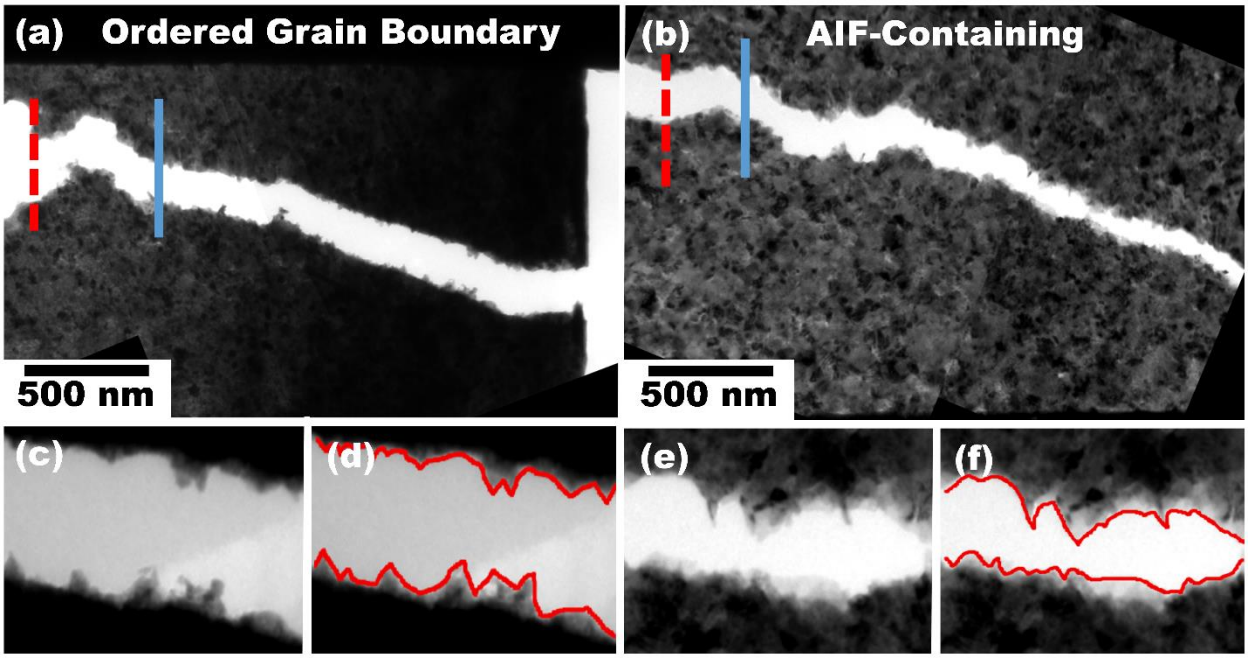

Figure 4.7. Bright field transmission electron microscopy images are shown of the (a) ordered grain boundary and (b) amorphous intergranular film (AIF) containing samples after fatigue failure. The dashed red lines indicate the point of crack initiation where crack propagation occurs to the right until reaching the solid blue line, where sudden failure then commenced. The fracture surfaces are shown in greater detail for the (c) ordered grain boundary and (e) AIF-containing samples, with outlines of the fracture surface shown for each sample in (d) and (f).

Toughening mechanisms can be categorized based on where they occur in relation to the crack tip and the shielding mechanisms. Extrinsic toughening operates behind the crack tip and lowers the effective force felt by the crack tip. Intrinsic toughening operates in front of the crack tip primarily through plasticity and normally operates in more ductile materials [139]. Plasticity-

induced toughening was more extensive in the case of the ordered grain boundary sample – a result that was indirectly confirmed by the longer stable (subcritical) crack length prior to catastrophic failure in the ordered grain boundary sample compared to the AIF-containing sample. The effects of plasticity are also apparent in the propagating crack tip shape, as the ordered grain boundary sample showed a more open, blunted crack whereas the AIF-containing crack had a narrower crack profile, and correspondingly lower crack-tip opening displacement (Figure 4.3). This enhanced plasticity-induced toughening is due, in part, to the 12% lower yield strength of the ordered grain boundary sample (938 MPa for ordered grain boundaries compared to 1068 MPa for AIF-containing) [66]. Grain bridging, an extrinsic mechanism, was present in both samples and can also contribute to improved toughness. Factors such as dopant segregation, grain boundary character, disordering, and energy state have been found to impact the damage tolerance of a grain boundary [180-185]. For example, minimizing the number of low-angle grain boundaries and enhancing twinning improves fracture toughness [180, 186, 187]. Incorporation of these techniques with extrinsic mechanisms to enhance grain bridging offers pathways to resist crack propagation in nanocrystalline metals. Alloys with appropriate doping and annealing conditions that permit AIF formation should utilize the enhanced ductility observed in this study to intrinsically toughen nanocrystalline alloys and avoid catastrophic, sudden fracture. Nanocrystalline alloys containing AIFs are also stronger than the same alloy with only ordered grain boundaries [66, 72, 74], offering a unique combination of ductile crack tip shielding with strengths even higher than nanocrystalline metal expectations.

4.4 Conclusion

Cu-1 at.% Zr thin films were thermally processed to have either ordered grain boundaries or contain AIFs and then subjected to in situ TEM fatigue. A number of observations are made, with our main findings categorized by fatigue lifetime stage.

1) *Crack initiation*: The ordered grain boundary sample experienced grain growth and dislocation activity at the crack initiation site. Nanocracks formed within the ordered grain boundary sample interior and grew until a bridging grain detached, connecting the internal nanocrack to the notch to allow the start of crack propagation. The AIF-containing sample had no grain growth at crack initiation and instead had distributed plastic activity surrounding the notch region. Similar to the ordered sample, internal cracking occurred until the bridging grain yielded, connecting the nanocrack to the notch and allowing crack propagation to commence.

2) *Propagation*: The ordered grain boundary sample demonstrated unsteady, accelerating crack growth characterized by the formation of an extensive nanocrack network interspersed with grain bridges. In contrast, the AIF-containing sample experienced steady, constant-rate crack growth with distributed plastic activity preceding the crack tip. The evenly distributed plastic activity in the AIF-containing sample indicates that the grain boundaries were better able to mitigate dislocation damage, whereas the ordered grain boundary sample had extensive nanocracking and highly localized plasticity.

In summary, the ordered grain boundary sample had highly localized plasticity with unsteady crack propagation and extensive nanocracking. The AIF sample instead demonstrated enhanced ductility with steady crack propagation and evenly distributed plastic activity, indicating that the AIFs diffused grain boundary strain and inhibited boundary fracture. While nanocrystalline metal grain sizes cause undesirable rapid crack growth during fatigue, the

associated large volume fraction of grain boundaries may serve as a silver-lining. Extrinsically, grain bridging coupled with enhanced damage tolerance techniques can increase fatigue toughness by resisting crack propagation in nanocrystalline metals. Intrinsically, AIFs can diffuse grain boundary strain concentrations and promote dislocation activity for more stable crack growth. A simple thermal processing route has been shown to significantly enhance the ductile fatigue toughness of a nanocrystalline binary alloy suggesting a path forward for nanocrystalline alloys in fatigue related applications.

Chapter 5: Amorphous Intergranular Films Improve the Radiation Tolerance of Nanocrystalline Cu-Zr

5.1 Introduction

Future fission and fusion nuclear reactors will push the limits of current material capabilities [188-193]. For example, hotter reactor operation temperatures for more efficient electricity generation are projected to break 1000 °C at the gas outlets of Generation IV very high-temperature reactor designs [188, 189, 194]. In addition to high temperature demands, longer nuclear reactor lifetimes coupled with greater safety and reliability goals necessitate the need for materials with improved radiation tolerance [192]. Point defects formed during irradiation of metals consist of vacancies, interstitials, Frenkel pairs, and point defect clusters [195], where these defects can aggregate into larger structures to achieve lower energy states. Larger defects observed in face-centered cubic metals with low stacking fault energies include partial dislocations, Frank loops, perfect dislocations, and three-dimensional defects such as voids, and stacking fault tetrahedra [195]. Accumulation of radiation damage can eventually cause a multitude of issues including swelling caused by cavities (voids or bubbles) within a material [196], embrittlement caused by hardening [197], and irradiation assisted stress corrosion cracking caused by intergranular cracking [198].

Inclusion of surfaces and interfaces within a material have been shown to aid in defect recovery by acting as point defect sinks and recombination sites that reduce damage accumulation, leading to improved radiation tolerance [199-202]. Surfaces are ideal sinks that serve as perfect interstitial-vacancy recombination sites, a fact utilized by nanoporous metals that have an extremely large surface-to-volume ratio [199]. For example, nanoporous Au has been shown to be an unsaturable defect sink within an ideal ligament diameter versus dose rate window where defect migration to the ligament surface occurs faster than the time between collision cascades

[199, 203]. The ability of an interface, such as at a grain or phase boundary, to act as a sink is understood in relation to an ideal sink through the sink efficiency, which is defined as the ratio of the flux of defects to an interface to the flux of defects to an ideal sink [15].

Interfaces in the form of grain boundaries serve as defect sinks by absorbing interstitials and facilitating defect recombination through emission of the stored interstitials to vacancies, annihilating the defect pairs [199, 204]. The sink efficiency of a grain boundary is dependent on the grain boundary structure in addition to other considerations such as grain size, the presence of other nearby sinks such as voids or dislocations, the defect recombination rate [195, 205, 206], and defect in-boundary mobility [207]. Han et al. [206] observed that the void denuded zone width, an expression of sink efficiency, is dependent on both the grain boundary misorientation and normal plane in coarse-grained Cu. In addition to void denuded zones, grain boundary structure also influences impurity segregation, dopant diffusivity, and resistance against grain boundary sliding, which all in turn impact radiation tolerance [191]. Nanocrystalline metals have shown excellent radiation tolerance due to their large volume fraction of grain boundaries serving as defect sinks [5, 208-210], but grain growth during irradiation ultimately degrades this radiation tolerance due to the concurrent decrease in grain boundary fraction [199, 201, 208]. Additionally, a scaling breakdown has been observed where grain refinement alone is not sufficient to improve radiation tolerance [211, 212]. For example, Barr et al. [211] observed no change in defect size or density in irradiated nanocrystalline Pt with grain sizes ranging from 100 to 20 nm. Since sink efficiency and radiation tolerance are grain boundary dependent, approaches that can drastically alter grain boundary structure and chemistry in nanocrystalline metals are desirable [213].

One such approach is through complexions that describe grain boundaries as having phase-like behavior. Grain boundaries can undergo discrete transitions in structure and composition in

response to parameters such as temperature, composition, and grain boundary character [56, 59], and similar to traditional bulk phase transitions, grain boundaries that have undergone complexion transitions also have significantly changed behaviors. For example, Luo et al. [64] observed that Bi adsorption onto Ni grain boundaries to form bilayer complexions causes liquid-metal embrittlement in Ni-Bi compared to grain boundaries without bilayer adsorption. Another type of complexion is a disordered nanoscale film, also called an amorphous intergranular film (AIF). AIFs, also considered premelts [135], are amorphous regions at grain boundaries that form extremely close to the material melting point in order to lower the grain boundary energy, making AIFs the thermodynamically preferred grain boundary structure at extremely high temperatures [56, 62, 74]. Since AIFs are a thermodynamically preferred state, they serve to increase the thermal stability of nanocrystalline metals at very high temperatures [74, 126], meaning they may also combat the key issue of nanocrystalline grain growth during irradiation. While thermodynamic and kinetic mechanisms such as dopant segregation to the grain boundary [20] and Zener pinning [34, 35] can stabilize nanocrystalline grain sizes, these mechanisms often break down with increasing temperature [50, 214, 215]. AIFs not only stabilize a microstructure, but they best do so at very high temperatures, where for example a new microstructure stabilization regime was found at approximately 70% of the melting temperature in Ni-W due to AIF formation [126].

In addition to stabilizing the microstructure, AIFs may also improve radiation tolerance. Using molecular dynamics simulations, Ludy and Rupert [71] observed that AIFs act as ultra-efficient point defect sinks, able to absorb both interstitials and vacancies due to their excess free volume that better accommodates vacancies, compared to ordered grain boundaries that prefer interstitials. Related studies point towards excess free volume at interfaces as beneficial for radiation tolerance. Extra free volume present at phase boundary interfaces, such as multilayer

Cu-Nb [201, 216], and Cu-V [201, 217], in the form of constitutional vacancies increases the solubility of He and minimizes swelling, where more free volume correlates to increased He trapping and in turn improved radiation tolerance [218-220]. Samaras et al. [221] observed that free volume within a grain boundary can serve as defect recombination sites. Also, AIFs act as fast diffusion pathways, a property utilized during solid state activated sintering [62, 222], which may lead to faster in-boundary defect mobility and annihilation rates [207].

The impact of AIFs on radiation tolerance is evaluated experimentally using nanocrystalline ball-milled Cu-Zr samples heat treated to either have only ordered grain boundaries or to contain AIFs distributed throughout the grain boundary network. The samples were then subjected to in situ transmission electron microscopy (TEM) irradiation and ex situ bulk irradiation. Differences in the microstructural evolution and total defect cluster area density are evaluated from the in situ TEM irradiation data, and differences in grain growth as a function of depth and defect number density are evaluated from the ex situ irradiation data. These results highlight the importance of grain boundary structural transitions on radiation tolerance, where the incorporation of AIFs distributed throughout the grain boundary network cumulatively act to improve the radiation damage tolerance of nanocrystalline Cu-Zr.

5.2 Materials and Methods

AIF formation is promoted in alloys that have dopant segregation to the grain boundary and a negative enthalpy of mixing [75]. Cu doped with Zr satisfies these criteria, and Cu-Zr has been shown previously to form AIFs [66, 74]. A Cu-Zr powder composed of 3 at.% Zr was prepared using mechanical ball-milling in a SPEX SamplePrep 8000M Mixer/Mill to produce micrometer sized particles composed of nanocrystalline grains. The powders were milled for 10 h using a hardened steel vial and milling media with 2 wt.% stearic acid added as a process control

agent. Powder samples were then encapsulated under vacuum in high purity quartz tubes, and annealed at 950 °C ($0.98T_{solidus}$ of Cu-3 at.% Zr) for 1 h to achieve Zr dopant segregation and grain boundary structural transitions to AIFs. The samples were then either slowly cooled over a period of approximately 5 min or quenched in water in under 1 s. Slowly cooling gives any AIFs formed during the high temperature treatment sufficient time to return to a crystalline grain boundary structure, and will be referred to as the ordered grain boundary sample. If instead the sample was rapidly quenched, thermodynamically stable states accessible at elevated temperatures such as AIFs are frozen into a place at room temperature, and will be referred to as the AIF-containing sample. Since AIFs are only thermodynamically preferred close to the melting point of the material, AIFs quenched into place are metastable at room temperature [57, 59, 66]. It is also important to note that AIFs do not exist at every grain boundary due to heterogeneous distributions of grain boundary energy, local chemistry, and quench rate [56, 66].

In situ TEM irradiation refers to ion irradiation performed on electron transparent specimens with concurrent TEM inspection, and ex situ irradiation refers to ion irradiation performed on a bulk specimens under vacuum in a separate irradiation chamber. Both ordered grain boundary and AIF-containing samples of the ball-milled Cu-Zr powder were subjected to in situ TEM and ex situ irradiation using an Au^{4+} ion beam generated by a Tandem Van De Graaff accelerator at Sandia National Laboratories [158]. Estimations of the depth dependent displacement damage, projected ion beam range, and amount of implanted Au in the irradiated samples were calculated using the Stopping and Range of Ions in Matter (SRIM) 2013 program [223] with the quick Kinchin-Pease damage estimation method [224], and threshold displacement energies of 30 eV for Cu and 40 eV for Zr [212]. Flux is defined as the number of ions crossing a unit area per unit time (ions/cm^2s), and fluence is the flux integrated over time to yield the total

number of ions irradiated into the material over the entire irradiation period (ions/cm^2). Damage accumulation levels due to increasing dose are measured using displacements per atom (dpa), and dose rate is the damage accumulation per unit time (dpa/s).

In situ TEM irradiation was performed using the I^{3}TEM JEOL 2100 at Sandia National Laboratories [158] operating at 200 kV. In situ TEM irradiation video was collected at 15 frames per second in bright field TEM mode using a 1k × 1k camera. A 2.8 MeV Au^{4+} beam was used to irradiate the samples at a flux of 1.5×10^{11} ions/cm^{2}s to a fluence of 4.0×10^{14} ions/cm^2 and damage level of approximately 7 dpa (dose rate of 2.6×10^{-3} dpa/s). The ion beam impacted the in situ TEM samples 60° to the sample surface in order to optimize the coincidence of the electron and ion beams. Ex situ irradiation was performed on ball-milled particles of the ordered grain boundary and AIF-containing samples. The particles are hundreds of micrometers thick and contain thousands of nanocrystalline grains, constituting bulk irradiation conditions. Two iterations of the ex situ irradiation were performed at 25 °C and 200 °C. A 20 MeV Au^{4+} beam was used at a flux of 1.1×10^{12} ions/cm^{2}s to a fluence of 2.1×10^{16} ions/cm^2 and damage level of approximately 95 dpa (dose rate of 4.8×10^{-3} dpa/s). The ion beam impacted the bulk samples 90° to the sample surface. Ex situ irradiation occurred through rastering of a highly focused ion beam to better ensure accurate fluence calculations over the entire irradiated area. No active cooling was present during the ex situ irradiations, but any degree of irradiation induced heating will be equal between the ordered grain boundary and AIF-containing samples since they were irradiated using the same parameters at the same time. Details of the irradiation experiments are presented in Table 5.1.

Experiment Type	Temperature (°C)	Ion Beam	Power (MeV)	Flux (ions/cm^{2}s)	Fluence (ions/cm^2)	Beam Projected Range (μm)	Max Dose (dpa)	Max implanted Au (at.%)
In situ TEM	25	Au^{4+}	2.8	1.5×10^{11}	4.0×10^{14}	NA	7	0.03
Ex situ	25	Au^{4+}	20	1.1×10^{12}	2.1×10^{16}	2.2 +/-0.3	95	0.3
Ex situ	200	Au^{4+}	20	1.1×10^{12}	2.1×10^{16}	2.2 +/-0.3	95	0.3

Table 5.1. Details of the in situ transmission electron microscopy and ex situ irradiation experiments.

All electron transparent samples of the ball-milled Cu-Zr powders for the in situ TEM irradiations and post ex situ irradiation TEM inspections were made through the focused ion beam (FIB) lift-out technique for cross-sectional TEM inspection using an FEI Nova 600 Nanolab and FEI Quanta 3D FEG Scanning Electron Microscope (SEM) with final low voltage polishes to remove excess FIB damage. Bright field TEM, high resolution TEM, scanning TEM (STEM), STEM energy dispersive X-ray spectroscopy (STEM-EDS), and selected area electron diffraction were performed using a JEOL JEM-2100 and JEOL 2800 TEM operating at 200 kV. AIF imaging was performed with high resolution TEM where Fresnel fringes were used to identify interfacial films and ensure edge-on orientation of the grain boundaries. STEM-EDS maps were collected using the Cliff-Lorimer method with no absorbance using a 3 × 3 kernel size. Electron energy loss spectroscopy (EELS) was performed using a JEOL GrandARM300CF in STEM mode operating at 300 kV in order to compute the thicknesses of the electron transparent specimens for volumetric defect area and number density calculations. The thicknesses were calculated using the log-ratio (absolute) method with a measured convergence semi-angle of 21 mrad, collection semi-angle of 30 mrad, and effective atomic number of 29. The average thicknesses of each electron transparent sample were measured by finding the average sample thickness from a total measured area of approximately 12 μm^2 on each lift-out.

Transmission Kikuchi diffraction (TKD) was performed on the ex situ irradiated samples using an FEI Quanta 3D FEG SEM-FIB with Kikuchi diffraction patterns collected using an Oxford Nordlys F+ electron backscatter diffraction detector. TKD was performed following methods established in previous TKD studies [225-227]. The electron transparent samples were held at a working distance of approximately 3.5 mm and tilted 20° from horizontal, and the SEM was operated at 30 kV and 11 nA using a 1 mm aperture with the microscope in its high current analytical mode. TKD maps and inverse pole figures (IPFs) were collected using a step size of 10 nm in a series of small maps in order to keep scan times short to best minimize drift. Multiple scans were then combined to create one large scan map for each sample, where each combined map contained 175,000 to 250,000 points. A minimum grain reconstruction threshold of 2° was used in TKD data analysis. No other data processing was performed, and the TKD results shown in this study are comprised of the raw data. Grain size was calculated from bright field TEM images and verified using the TKD data by measuring the areas of grains and calculating the average equivalent circular diameter. At least 100 grains were measured from the ordered grain boundary and AIF-containing samples to measure the average grain size before irradiation. Additional details regarding the inspection and irradiation methods are presented in Appendix C.

5.3 Results and Discussion

5.3.1 Initial Microstructure and Radiation Conditions

Figure 5.1 shows representative images of the ball-milled Cu-Zr samples after receiving heat treatments to create the ordered grain boundary and AIF-containing samples. The average grain size before irradiation was 110 ± 34 nm for the ordered grain boundary sample, and 91 ± 30 nm for the AIF-containing sample. Figure 5.1(a) shows a bright field TEM image of the AIF-containing sample microstructure before irradiation. Figure 5.1(b) shows a high resolution TEM

image of an AIF from the AIF-containing sample, where the dashed red lines highlight the presence of the AIF along the grain boundary. Figure 5.1(c) shows a dark field STEM image from the AIF-containing sample, and Figure 5.1(d) shows the associated STEM-EDS map with the distribution of Zr throughout the microstructure shown in yellow. Zr segregation to the grain boundaries was present in both samples, with examples indicated by the red arrows. Due to the ball-milling process, ZrC precipitates are also found within microstructure [74]. The inset in Figure 5.1(a) shows the associated selected area electron diffraction pattern, where the solid blue lines indicate the face-centered cubic Cu phase, and the dashed red lines indicate the ZrC phase. The ZrC precipitates may impact the radiation damage tolerance behavior of the nanocrystalline Cu-Zr samples since precipitates can both limit grain boundary mobility through pinning [34, 35] and serve as defect sinks [228, 229]. Both the ordered grain boundary and AIF-containing samples were sourced from the same ball-milled powder and contained ZrC precipitates, meaning the impact of ZrC precipitates between the two samples will be the same and divergences in radiation damage tolerance can be attributed to the presence or absence of AIFs distributed throughout the grain boundary network.

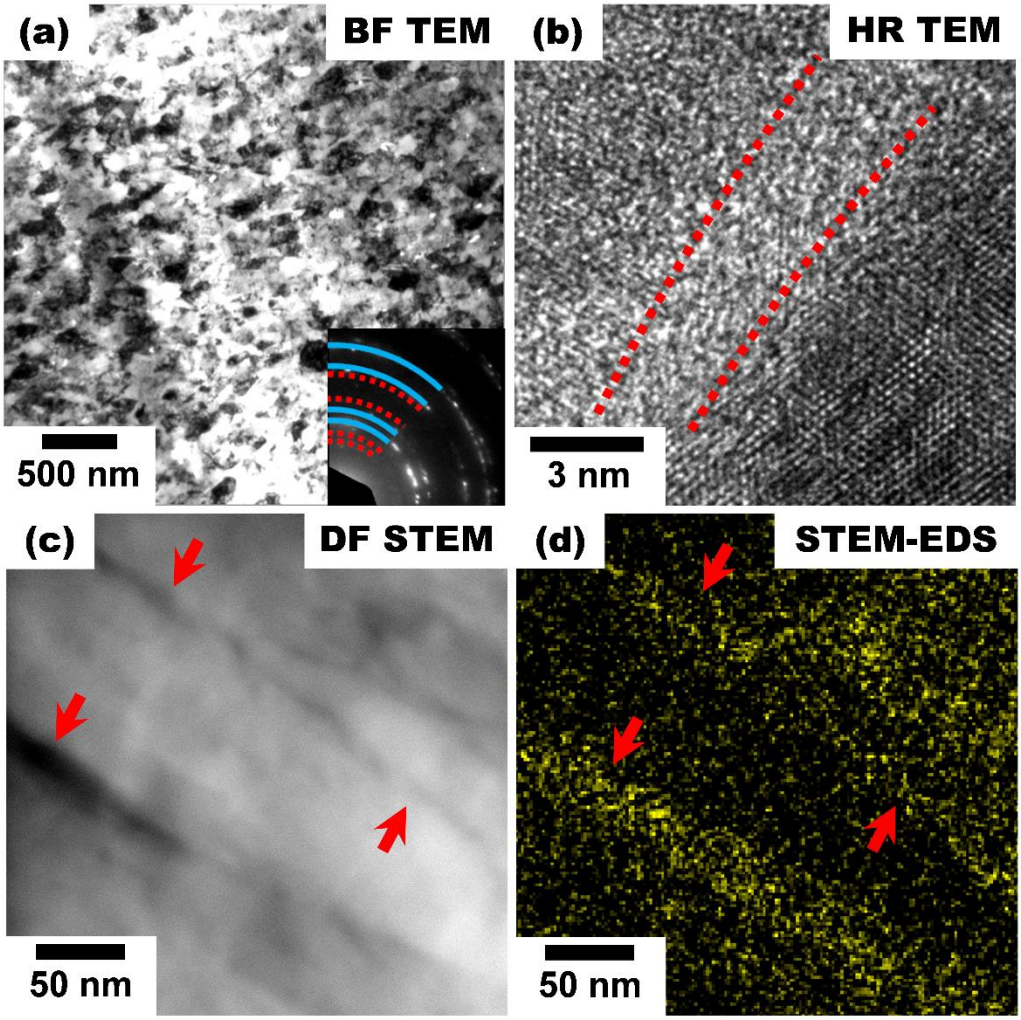

Figure 5.1. Microstructural and chemical analysis of the Cu-3 at.% Zr heat treated alloy before irradiation. (a) shows bright field transmission electron microscopy (BF TEM) image of the sample containing amorphous intergranular films (AIFs) before irradiation. The inset shows the associated selected area electron diffraction pattern, where the solid blue lines indicate the face-centered cubic Cu phase, and the dashed red lines indicate the ZrC phase. (b) shows high resolution (HR) TEM image of an AIF, where the dashed red lines highlight the presence of the AIF along the grain boundary. (c) shows dark field scanning transmission electron microscopy (DF STEM) image and the associated (d) energy dispersive X-ray spectroscopy map (STEM-EDS), where Zr dopant is indicated with yellow. The red arrows in (c) and (d) indicate grain boundaries with Zr segregation.

The in situ TEM and ex situ bulk experiments constitute a roughly one order magnitude difference in radiation conditions. Figure 5.2 shows the estimated damage accumulation level as a function of cross-sectional depth for each experiment. Figure 5.2(a) shows the in situ TEM irradiation using a 2.8 MeV Au^{4+} beam impacting 60° to the sample surface. The dashed red line

at 115 nm indicates the average electron transparent sample thickness of the in situ TEM irradiated samples determined through EELS. The associated red box indicates the approximate electron transparent sample thickness range subjected to irradiation accounting for a 20 nm standard deviation of the TEM sample thickness. The projected range of a 2.8 MeV Au^{4+} beam irradiated into Cu-3 at.% Zr impacting 90° to the sample surface is 250 ± 60 nm which is well beyond the average electron transparent sample thickness, but the 60° specimen angle necessary to permit concurrent TEM inspection may allow some Au implantation to occur, reaching a maximum possible value of 0.03 at.% Au. Figure 5.2(b) shows similar calculations for the ex situ irradiation into bulk samples using a 20 MeV Au^{4+} beam impacting 90° to the sample surface. The dashed yellow line and associated yellow box show the projected beam range of 2.2 ± 0.3 μm. A maximum damage level of approximately 95 dpa occurs at a depth of 2 μm within the bulk samples, and approximately 0.3 at.% Au was implanted within the bulk specimen. While Au implantation may alter local alloy chemistry and impact behavior upon irradiation, both the ordered grain boundary and AIF-containing samples were subjected to the same degree of Au implantation during the in situ TEM and ex situ irradiations, meaning divergences in radiation damage tolerance may again be attributed to differences in the grain boundary structure.

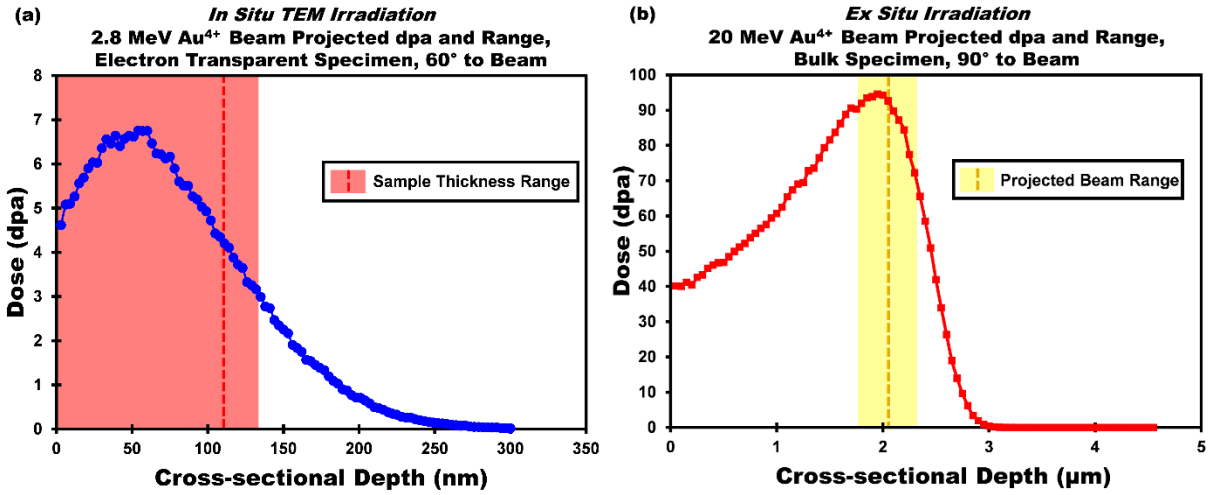

Figure 5.2. The estimated damage accumulation levels measured in displacements per atom (dpa) as a function of cross-sectional depth for the in situ transmission electron microscopy (TEM) and ex situ irradiations. (a) shows the in situ TEM irradiation profile using a 2.8 MeV Au^{4+} beam incident 60° to the sample surface. The dashed red line at 115 nm indicates the average electron transparent sample thickness of the in situ TEM irradiated samples, and the associated red box indicates the approximate electron transparent sample thickness range subjected to irradiation. (b) shows the ex situ bulk sample irradiation profile using a 20 MeV Au^{4+} beam incident 90° to the sample surface. The dashed yellow line and associated yellow box show the projected beam range of 2.2 ± 0.3 μm.

The sink efficiencies of different grain boundaries have previously been compared using denuded zone widths where a larger denuded zone correlates to improved sink efficiency, but several factors limit this interpretation [230]. For example, the grain boundary structure itself is dynamic during irradiation [207]. Also, AIFs do not occur at every grain boundary, further restricting the comparison of individual grain boundaries for sink efficiency and implications on radiation tolerance. Instead the sink efficiency and radiation tolerance of the entire grain boundary network is investigated. The microstructural evolution and total defect cluster area density from the in situ TEM irradiation, and grain growth and defect number density from the ex situ irradiation are gathered across many grains to evaluate the radiation tolerance of the grain boundary network as a whole.

5.3.2 Microstructural Evolution and Total Defect Cluster Area Density from the In Situ TEM Irradiation

Microstructural evolution during in situ TEM irradiation was analyzed using bright field TEM images gathered from the in situ TEM video. Three modes of microstructural evolution were observed. Mode 1 refers to a general change in grain shape without a significant change in area, which may be due to sample bending or grain boundary mobility. Mode 2 refers to grain growth indicated by a significant increase in grain area at the expense of a neighboring grain. Mode 3 refers to a significant change in grain contrast due to either sample bending, accumulation of defects, or grain rotation out of the bright field TEM imaging conditions. Figure 5.3 shows bright field TEM images captured from the in situ TEM irradiation videos of the ordered grain boundary and AIF-containing samples. Figures 5.3(a)-(c) show the microstructural evolution of the ordered grain boundary sample with increasing dose at 1, 3, and 6 dpa respectively, and Figures 5.3(d)-(f) shows similar images for the AIF-containing sample. Grains indicative of each microstructural evolution mode are highlighted in red and numbered in accordance with their evolution mode in Figure 5.3. All three modes of microstructural evolution were observed in the ordered grain boundary sample, but mode 2 grain growth was not observed in the AIF-containing sample within the imaged region. This indicates that there was less grain growth in the AIF-containing sample compared to the ordered grain boundary sample during the in situ TEM irradiation.

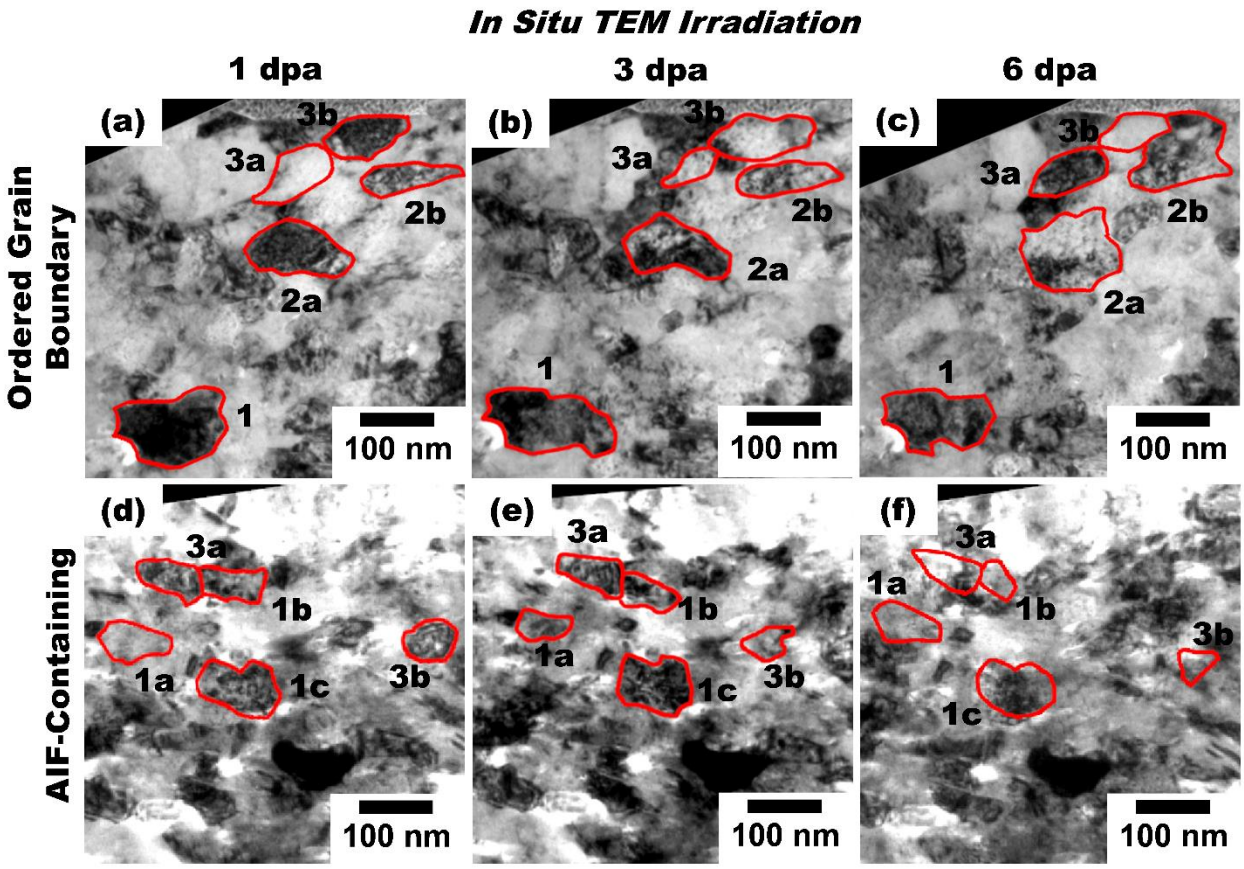

Figure 5.3. Microstructural evolution with increasing dose measured in displacements per atom (dpa) during in situ transmission electron microscopy (TEM) irradiation. (a)-(c) show microstructural evolution of the ordered grain boundary sample with increasing dose at 1, 3, and 6 dpa respectively. (d)-(f) show similar images for the sample containing amorphous intergranular films (AIFs). Three modes of microstructural evolution were observed. Mode 1 refers to a general change in grain shape without a significant change in area. Mode 2 refers to grain growth indicated by a significant increase in grain area at the expense of a neighboring grain. Mode 3 refers to a significant change in grain contrast. Grains indicative of each microstructural evolution mode are highlighted in red and numbered in accordance with their evolution mode.

Determination of defect density, calculated using defect width, area, number, or some combination thereof, has four notable experimental limitations [231]. The resolution limit of the imaging technique used curtails measurement of the smallest defects, defects can be lost due to diffusion to the sample surface, the foil thickness influences perceived defect density, and finally only a proportion of resolvable defects are seen due to imaging condition constraints. The first

three limitations are taken into consideration by using identical TEM inspection conditions between samples, and by measuring the sample thickness using EELS to normalize the defect densities by volume. The fourth limitation poses the greatest challenge. Performing traditional TEM techniques to determine radiation defect nature as described by Jenkins and Kirk [231] involves sample tilting to precise imaging conditions so that the appropriate coupling of the diffraction vector (g) and the Burgers vector (b) are met to yield $g \bullet b$ visibility or invisibility conditions for defect analysis, but this is non-trivial in nanocrystalline metals due to the small grain size [213]. Accounting for this limitation, defect density from the in situ TEM irradiation is gathered using the total defect cluster area across many grains instead of measuring the size of individual defects in order to avoid ambiguities in defect nature and size.

While the exact nature of the defects are not known, previous heavy ion irradiation studies using Cu, a face-centered cubic material, observed that vacancy and interstitial clusters form directly within the collision cascade, and then coalesce into point defect clusters, loops, dislocations, dislocation tangles, cavities, and vacancy-type stacking fault tetrahedra [232, 233]. The addition of Zr solute to Cu decreases the stacking fault energy, and may make stacking fault tetrahedra easier to form in Cu-Zr than in pure Cu [234]. Irradiation induced defects were isolated compared to other TEM contrast features such as bend contours through feature movement using frame by frame video analysis. Irradiation induced defects were identified as discrete dark contrast features that appeared and evolved asynchronously within a grain, moving in a jerky manner consistent with defect percolation motion [235, 236]. Total defect cluster areas were measured from individual grains with visible defects tracked throughout the entire radiation sequence. Total defect cluster area per volume for each dose level was then calculated by measuring the total defect area within a grain and dividing by the grain volume. The grain volume was calculated using the

grain area at each dose level multiplied by the average thickness of the electron transparent sample measured through EELS. The defect cluster areas from each grain were then summed across all tracked grains to find the total defect cluster area. The total defect area measurements were done twice from different grains, using a total of approximately 20 grains from each the ordered grain boundary and AlF-containing samples.

Figure 5.4 presents the total defect cluster area per volume, hereafter referred to as the defect area density, measurement method and change with increasing dose gathered using the in situ TEM irradiation video from 0 to 6 dpa. Defects present at 0 dpa may be due in part to the FIB sample preparation method. The scale bars in Figures 5.4(a)-(d) are 100 nm. Figures 5.4(a) and (c) show bright field TEM images of a representative grain from the ordered grain boundary sample subjected to in situ TEM irradiation at 1 and 2 dpa, with the grain outlined in red. The radiation induced defects present in each grain are marked in black in Figures 5.4(b) and (d). The defect area density is then calculated by finding the total area of identified defects in Figures 5.4(b) and (d) and then dividing by the grain volume, calculated using the sample thickness multiplied by the respective outlined grain area in Figures 5.4(a) and (c). While extremely thin, the electron transparent samples still have an average thickness of 115 ± 20 nm, or approximately the average grain diameter. Figure 5.4(e) shows the same grain from Figures 5.4(a) and (c) rotated to qualitatively show the impact of electron transparent specimen thickness on the measurement of defect area density. Since bright field TEM images show features in projection, the true shape and size of the defect may be different than what is viewed in a bright field TEM image, represented by the solid and dotted lines within the sample. The solid line represents the true defect shape and size, and the dotted line represents the perceived defect shape and size in the projected bright field TEM image. Also, parts of a defect may be invisible or tangled if not in appropriate imaging

conditions. Figure 5.4(f) shows the change in defect area density with increasing dose, where error bars represent one standard deviation. Due to the measurement methods and imaging limitations, it cannot be determined if changes in the defect area density are due to differences in individual defect size or number of defects. It can simply be observed that the ordered grain boundary sample (blue circles) shows a significant increase in defect area density compared to the AIF-containing sample (red squares) starting at 4 dpa, remaining through to the end of the radiation sequence. At 6 dpa, the ordered grain boundary sample had approximately 1.5 times the defect area density compared to the AIF-containing sample.

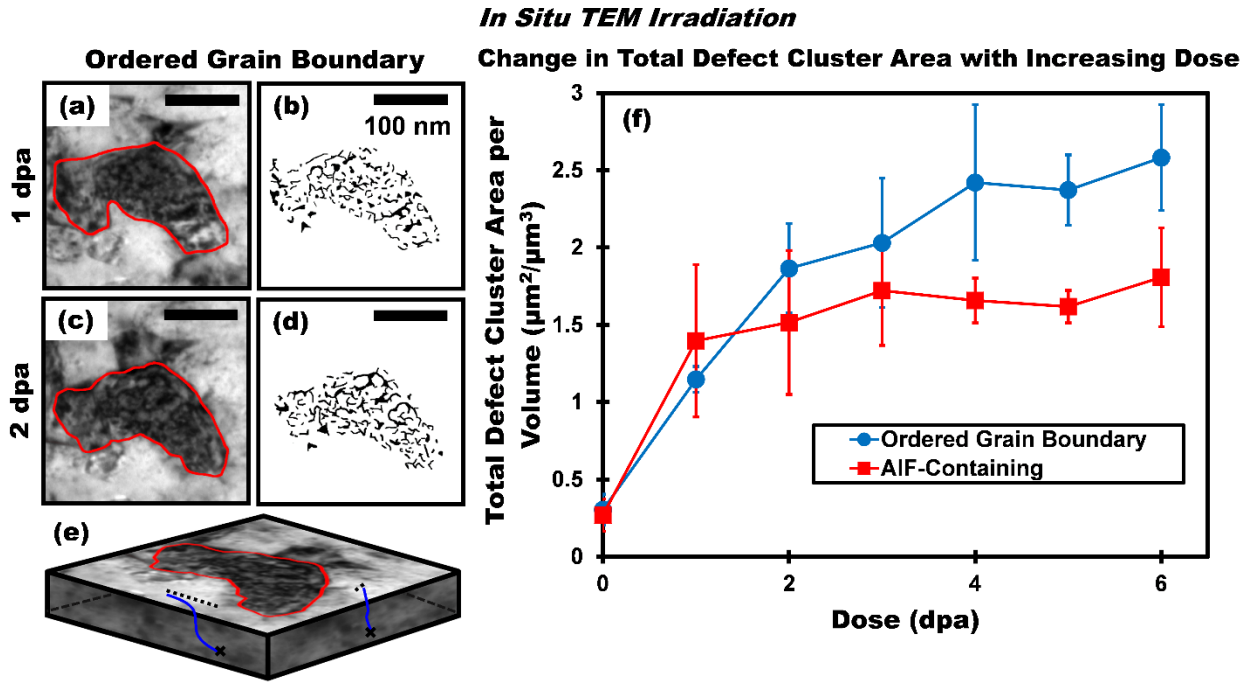

Figure 5.4. The total defect cluster area density with increasing dose measured in displacements per atom (dpa) from 0 to 6 dpa. The scale bars in (a)-(d) are 100 nm. (a) and (c) show bright field transmission electron microscopy (TEM) images of a representative grain from the ordered grain boundary sample subjected to in situ TEM irradiation at 1 and 2 dpa, with the grain boundary outlined in red. (b) and (d) show radiation induced defects marked in black present in each respective grain. (e) shows the same grain from (a) and (c) rotated to qualitatively show the impact of electron transparent specimen thickness on the measurement of defect cluster area, represented by the solid and dashed lines. (f) shows the change in total defect cluster area per volume with increasing dose for the ordered grain boundary (blue circles) and amorphous intergranular film (AIF) containing (red squares) samples. Error bars represent one standard deviation.

In addition to the defect area density values, the defect generation rates can also be compared, where the defect generation rate is defined as the change in number of visible defects with increasing dose. Generally there are four stages during defect accumulation determined through the defect generation rate. The first stage is defect incubation, marked by a steep, positive defect accumulation slope. The second stage is defect non-interaction, followed by the third defect interaction stage, both marked by steadily decreasing yet positive slopes. The fourth stage is defect saturation where an equilibrium between defect formation and destruction is reached, marked by a plateau in defect generation [237, 238]. A final recovery stage may also occur, marked by a negative slope due to decreasing defect density [239]. In the ordered grain boundary sample, the incubation stage lasted from 0 to 1 dpa with a steep slope of 0.84 $\mu m^2/\mu m^3$dpa, the defect non-interaction and interaction stages lasted from 1 to 3 dpa with slightly lower slope of 0.72 $\mu m^2/\mu m^3$dpa, and the saturation stage lasted from 3 to 6 dpa, with a plateau slope of 0.16 $\mu m^2/\mu m^3$dpa. In comparison, the AIF-containing sample also had a defect incubation zone from 0 to 1 dpa with a steep slope 1.13 $\mu m^2/\mu m^3$dpa, but after this stage the AIF-containing sample diverges in behavior from the ordered grain boundary sample. Instead the defect non-interaction and interaction stages from 1 to 3 dpa had a slope of only 0.16 $\mu m^2/\mu m^3$dpa, or 4.5 times smaller than in the ordered grain boundary sample. The defect generation rate then saturates from 3 to 6 dpa with a plateau slope of 0.02 $\mu m^2/\mu m^3$dpa, or 8 times smaller than in the ordered grain boundary sample. This indicates that the defect generation rate is not only significantly lower, but a more robust defect saturation plateau is achieved at a lower defect area density in the AIF-containing sample compared to the ordered grain boundary sample. This indicates that AIFs distributed throughout the grain boundary network can improve the net grain boundary sink efficiency,

allowing a steady-state between defect formation and destruction to be reached much earlier in radiation damage lifetime.

5.3.3 Grain Growth and Defect Number Density per Volume from the Ex Situ Irradiations at 25 °C and 200 °C

While in situ TEM irradiation provides crucial insight regarding time dependent phenomena such as defect generation rate, interpretations can be influenced by factors such as surface defect annihilation [240, 241], and electron beam effects [242-244]. Complementary ex situ bulk irradiations were performed using the conditions presented in Table 5.1 and Figure 5.2(b). In the bulk sample cross-sectional reference frame, the Y-axis is parallel to the ion beam direction, and the Z-axis is parallel to the cross-sectional inspection axis. The Z-axis was chosen for grain orientation analysis since differing textures between samples along the inspection axis may impact defect density comparisons since defect habit planes and visibility criteria are crystallographically constrained, making different proportions of defects visible depending on the inspected crystal direction [231]. An IPF map visualizes texture by showing which crystal direction is parallel to the IPF assigned direction, here the Z-axis, which will be referred to as IPF-Z. Equal area projection plots are used to analyze the IPF-Z maps, where an even distribution of plotted directions across the whole projection area correlates to a random distribution of crystal directions in the measurement region and a lack of texture [245]. The samples were irradiated two at temperatures, 25 °C and 200 °C, in order to access different defect annihilation and mobility regimes. At 25 °C primarily interstitials are mobile since little energy is required for an interstitial to move to an adjacent interstitial location, but vacancy mobility is limited since it requires rearrangement of atoms at lattice sites. Therefore vacancies are immobile at room temperature and are annihilated when recombined with mobile interstitials [196], which for example may be emitted by a nearby grain boundary [204]. At approximately 30% of the melting temperature,

there is sufficient thermal energy for vacancies to also become mobile, allowing vacancy clustering and the formation of larger vacancy-based defects such as voids and stacking fault tetrahedra [196].

Figures 5.5(a)-(c) show the bright field TEM, Kikuchi band contrast map, and IPF-Z maps for the ordered grain boundary sample irradiated at 25 °C outlined in purple, and Figures 5.5(g)-(i) show similar data for the AIF-containing sample outlined in orange. The dashed red lines show the sample surface, and the dashed yellow lines show the projected ion beam range, approximately 2.2 μm deep within the sample. Figure 5.5(e) shows the electron transparent sample reference frame axes. Figures 5.5(d) and (f) show equal area projection plots for the corresponding IPF-Z maps. The IPF-Z equal area projection plots were only collected for the regions most affected by irradiation, from the sample surface to the projected beam range depth between the red and yellow dashed lines. Both samples irradiated at 25 °C have similar textures within the beam projected range, with some preference for (101) oriented grains. Figure 5.6 shows similar data as presented in Figure 5.5 for the samples irradiated at 200 °C. The equal area projection distribution plots in Figures 5.6(d) and (f) both show a greater preference for the (001) direction compared to the samples irradiated at 25 °C. This means that defect densities are comparable within each temperature condition, but inspections of the 25 °C and 200 °C samples may capture different proportions of visible radiation defects, limiting direct comparison of defect densities between the two temperature conditions.

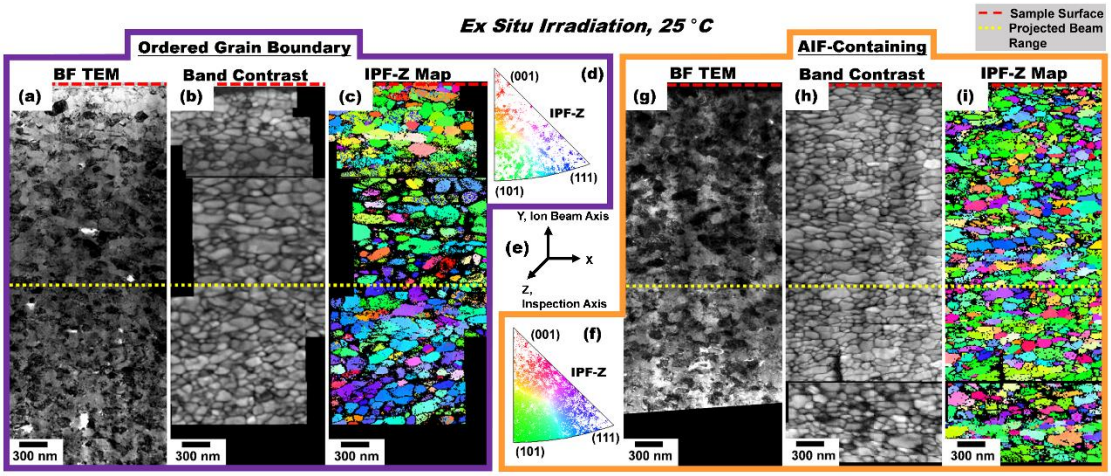

Figure 5.5. (a)-(c) Bright field transmission electron microscopy (BF TEM), band contrast, and inverse pole figure Z direction (IPF-Z) maps for the ordered grain boundary sample irradiated at 25 °C outlined in purple. (g)-(i) show similar data for the sample containing amorphous intergranular films (AIFs) outlined in orange. The dashed red lines show the sample surface, and the dashed yellow lines show the projected ion beam range. (e) shows the electron transparent sample reference frame axes, where the Y-axis is parallel to the ion beam axis, and the Z-axis is parallel to the inspection axis. (d) and (f) show equal area projection plots for the corresponding IPF-Z maps, where (d) refers to the ordered grain boundary sample, and (f) refers to the AIF-containing sample.

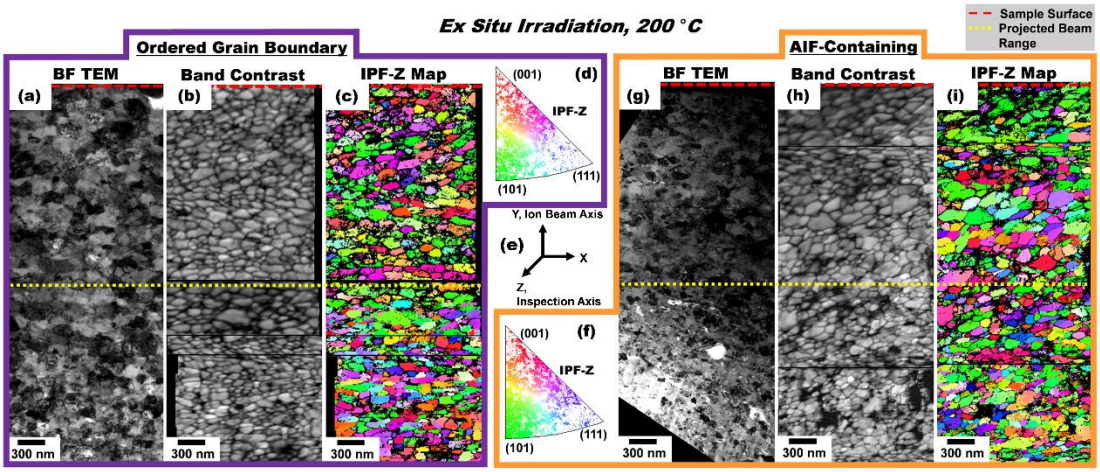

Figure 5.6. (a)-(c) show bright field transmission electron microscopy (BF TEM), band contrast, and inverse pole figure Z direction (IPF-Z) maps for the ordered grain boundary sample irradiated at 200 °C outlined in purple. (g)-(i) show similar data for the sample containing amorphous intergranular films (AIFs) outlined in orange. The dashed red lines show the sample surface, and the dashed yellow lines show the projected ion beam range. (e) shows electron transparent sample reference frame axes, where the Y-axis is parallel to the ion beam axis, and the Z-axis is parallel to the inspection axis. (d) and (f) show equal area projection plots for the corresponding IPF-Z maps, where (d) refers to the ordered grain boundary sample, and (f) refers to the AIF-containing sample.

Figure 5.7 shows the grain size as a function of cross-sectional depth measured from the TEM imaged regions in Figures 5.5 and 5.6. Each point shows the average grain size of a 100 nm depth range. For example, the first point shows the average grain size of those grains present from the sample surface at 0 nm to 100 nm, and the second point shows the average grain size of those grains present from 100 nm to 200 nm deep within the sample and so forth. Approximately 10 grains were used to find the average grain size present in each 100 nm section. The grain position within the cross-sectional depth was determined using the centroid of the grain, where the centroid is defined as the average coordinates of all of the image pixels contained within the grain. The dashed yellow line and associated yellow box show the expected beam penetration depth at approximately 2.2 ± 0.3 μm. The two dashed gray lines shows the average grain sizes of the ordered grain boundary and AIF-containing samples before irradiation. Figure 5.7(a) shows the grain size measurements for the samples irradiated at 25 °C. The ordered grain boundary sample (blue circles) shows grain growth to approximately 140 nm compared to the initial average grain size of 110 ± 34 nm. While the 140 nm average grain size is within error of the baseline average grain size, the consistent upward shift in grain size within the projected beam range is indicative of grain growth. In the portions of the cross-section deeper than the beam projected range, the average grain size returns to the expected baseline grain size for the ordered grain boundary sample. The AIF-containing sample (red triangles) shows a different trend, where within the beam projected range, the average grain size stays close to the baseline grain size of 91 ± 30 nm. There is only apparent grain growth at the beam penetration depth, where damage levels reach a maximum of 95 dpa in addition to Au implantation that alters the expected alloy chemistry and may alter local damage tolerance behaviors. Figure 5.7(b) shows similar data for the samples irradiated at 200 °C. Both the ordered grain boundary (green circles) and AIF-containing (purple

triangles) samples follow similar trends where both samples had an increase in grain size to approximately 130-140 nm, and then a return to their respective baseline grain sizes beyond the beam projected range.

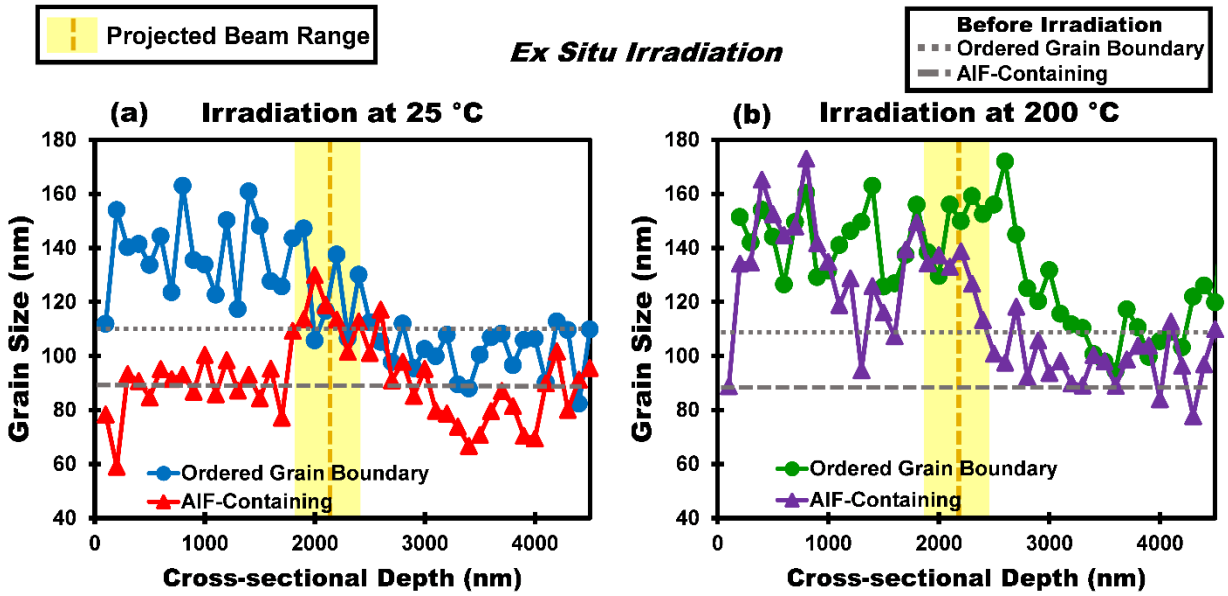

Figure 5.7. Grain size as a function of cross-sectional depth. Each point shows the average grain size of a 100 nm depth range. The dashed yellow line and associated yellow box show the expected beam penetration depth at approximately 2.2 ± 0.3 µm. The two dashed gray lines show the average grain sizes of the ordered grain boundary and amorphous intergranular films (AIF) containing samples before irradiation. (a) shows grain size measurements for the samples irradiated at 25 °C of the ordered grain boundary (blue circles) and the AIF-containing (red triangles) samples. (b) shows similar data for the samples irradiated at 200 °C for the ordered grain boundary (green circles) and AIF-containing (purple triangles) samples.

The number of defects in the sample independent of the defect size, hereafter referred to as the defect number density, was calculated by counting the number of dark spot damage features visible in bright field TEM images within the beam projected range (sample surface to 2.2 µm deep) and then divided by the sample measurement volume, which is the combined grain area from those grains in which defects were visible multiplied by the electron transparent sample thickness. The defect counting was repeated three times from three different regions of the irradiated samples,

accumulating to thousands of defects being counted in each sample. While the defect number density is also subject to ambiguity in accordance with the defect inspection challenges discussed, such as multiple defects being too close together to resolve, miscounting due to defect tangling or overlap, and the exact character of the defect being unknown, the large number of defects counted makes such errors inconsequential, and all measured samples are subject to the same counting errors. Error bars are calculated by adjusting the measurement volume using the variation in measured sample thickness from EELS. The lower bound is the number of counted defects divided by the minimum measurement volume using the minimum of the measured electron transparent sample thickness from EELS. The upper bound is calculated similarly using the maximum measurement volume.

Figure 5.8 shows representative high resolution TEM images of defects observed in the irradiated samples. Figure 5.8(a) shows an assortment of defects present as dark spots which may encompass defects previously observed in face-centered cubic Cu such as point defect clusters, stacking fault tetrahedra, loops, dislocations, or dislocation tangles [232, 233]. A stacking fault tetrahedron indicated by the red arrow in Figure 5.8(a) is shown in greater detail in Figure 5.8(b) using the inverse fast Fourier transform of the stacking fault tetrahedron. Dotted red lines frame the stacking fault tetrahedron, and solid red lines indicate a possible stacking fault. Further TEM inspection is necessary to fully characterize the nature of the stacking fault tetrahedron [231]. Cavities can be easily viewed by going slightly out of focus, where underfocused cavities appear bright with a dark border [231]. Figure 5.8(c) shows several underfocused cavities, with one cavity indicated by a red arrow and shown in greater detail in Figure 5.8(d). Cavity formation can be promoted by high oxygen content in the lattice [232], which is an expected impurity for ball-milled alloys [103, 215].

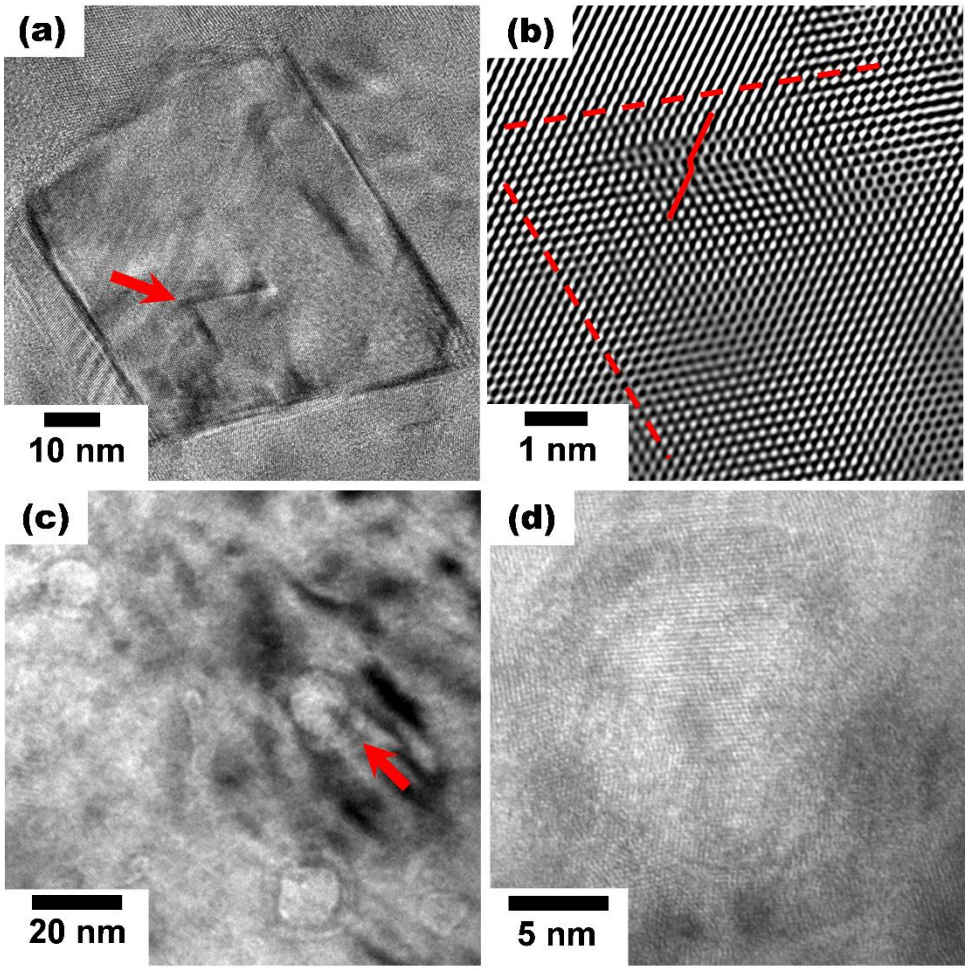

Figure 5.8. Representative high resolution transmission electron microscopy images of defects observed in the irradiated samples. (a) shows several defects present as dark spots which may be point defect clusters, stacking fault tetrahedra, loops, dislocations, or dislocation tangles. (b) shows the inverse fast Fourier transform of a possible stacking fault tetrahedron indicated by the red arrow in (a). Dotted red lines frame the stacking fault tetrahedron, and the solid red line indicates a possible stacking fault. (c) shows several underfocused cavities, with one cavity indicated by a red arrow and shown in greater detail in (d).

Defects such as those shown in Figure 5.8 were then counted to calculate the defect number density. Figure 5.9 shows the defect number density for the ordered grain boundary and AIF-containing samples irradiated at 25 °C and 200 °C. For the samples irradiated at 25 °C, the ordered grain boundary sample is shown with a blue circle, and the AIF-containing sample with a red circle. For the 200 °C irradiation, the ordered grain boundary sample is shown with a green square,

and the AIF-containing sample with a purple square. The associated ranges indicate the upper and lower error bounds of defect number density due to variation in the sample thickness. For the 25 °C irradiation, the ordered grain boundary sample showed a higher defect number density compared to the AIF-containing sample beyond the considerations of variations in sample thickness, suggesting improved defect sinking in the AIF-containing sample compared to the ordered grain boundary sample. For the 200 °C irradiation, both the ordered grain boundary and AIF-containing samples had comparable defect number densities.

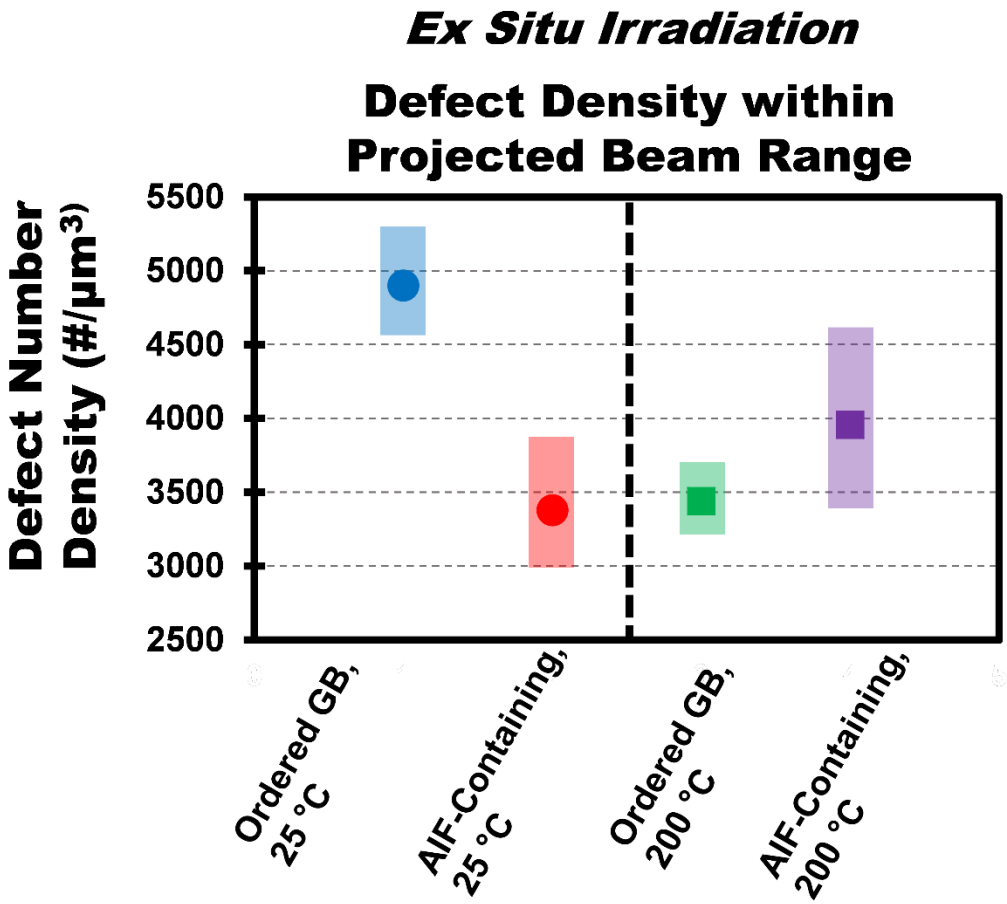

Figure 5.9. The defect number density for the ordered grain boundary and amorphous intergranular film (AIF) containing samples irradiated at 25 °C and 200 °C. For the samples irradiated at 25 °C, the ordered grain boundary sample is shown with a blue circle, and the AIF-containing sample with a red circle. For the 200 °C irradiation, the ordered grain boundary sample is shown with a green square, and the AIF-containing sample with a purple square. The associated ranges indicate the upper and lower error bounds of defect density due to variations in sample thickness.

5.3.4 Impact of Amorphous Intergranular Films and Grain Boundary Complexion Transitions on Radiation Tolerance

The AIF-containing samples have both lower defect area and number densities compared to the ordered grain boundary samples. This correlates to molecular dynamics simulations that have shown AIFs acting as unbiased sinks due to their increased thickness and excess free volume compared to an ordered grain boundary [71]. AIFs may also still be emitting interstitials to annihilate vacancies in the grain interior similar to an ordered grain boundary loaded with interstitials [204]. The increased effective thickness of an AIF also allows more of the collision cascade itself to be contained within the boundary compared to an ordered grain boundary, allowing defects to be produced closer to the sink and faster recombination rates [71]. AIFs also act as fast diffusion pathways [62, 207, 222], which may further increase in-boundary diffusion and recombination rates. The combined impact of these effects increases the sink efficiency of an AIF compared to an ordered grain boundary. As a result, incorporation of AIFs increases the net grain boundary network sink efficiency and reduces the overall defect area and number densities.

The AIF-containing sample also had less grain growth compared to the ordered grain boundary sample. Grain growth during irradiation can be caused by a number of factors, including radiation induced diffusion, dopant grain boundary desegregation, and ion beam mixing. Radiation induced diffusion is caused by atomic jumps within thermal spikes that generate the movement of atoms across grain boundaries. This in turn causes grain growth that is dependent on the local grain boundary curvature, nature of the cascade structure, formation of subcascades at grain boundaries [246-249], intrinsic properties of the material, and radiation conditions [213]. The increased effective thickness of an AIF compared to an ordered grain boundary may capture more of these atomic jumps and impede atomic movement into neighboring grains, thus limiting grain growth. AIFs may also restrict the local grain boundary mobility at thermal spikes [247],

especially since AIFs are preferred at very high temperatures. The proportion of the grain boundary network that transforms to an AIF both lowers the net grain boundary network energy and locally restricts grain boundary mobility, where even pinning only a fraction of grain boundaries has been shown to impede grain growth of the entire grain boundary network [53, 250]. Therefore by distributing AIFs throughout the grain boundary network, not only is the net sink efficiency of the grain boundary network increased, but the net grain boundary network energy and mobility is decreased, combining to prevent grain growth and dramatically improve the radiation tolerance of the nanocrystalline alloy.

Desegregation of dopants at the grain boundary may also degrade thermodynamic grain size stabilization and cause grain growth [251-253]. For example Cr depletion and Ni enrichment have been observed at the grain boundaries of irradiated 304L and 316L austenitic stainless steels [254], and dopant desegregation due to increasing temperature has been observed in nanocrystalline Ag-W [214]. Similarly, ion beam mixing disrupts the compositional separation between grain boundary and grain interior [255]. Miscible alloys are observed to undergo ballistic intermixing at phase boundaries, which has been observed in miscible alloy multilayers of Al-Nb [256] and Fe-W [257]. Conversely, immiscible alloy multilayers retain sharp chemical boundaries with no intermetallic formation or amorphization detected upon irradiation due to their large positive enthalpy of mixing, which indicates that any ballistic mixing is counteracted by dynamic demixing, which has been observed in Cu-Nb and Cu-V [201, 216]. Cu-Zr is a miscible alloy, chosen in part specifically for this characteristic to promote AIF formation [75]. STEM-EDS was performed on both the 25 °C and 200 °C ex situ irradiated ordered grain boundary and AIF-containing samples. Zr segregation to the grain boundaries was still present after irradiation, but subtle changes in adsorbed Zr and complexion transitions throughout the grain boundary network

could cumulatively degrade radiation tolerance over time. For the ordered grain boundary samples, thermal input alone is not sufficient to cause any of the observed grain growth. Annealing studies of the same ball-milled nanocrystalline Cu-Zr alloy showed excellent thermal stability at 550 °C where only ordered grain boundaries existed within the grain boundary network [74]. The combined effects of Zr dopant segregation that lowers the grain boundary energy and kinetic pinning from ZrC particles were sufficient to stabilize the nanostructure at temperatures below the AIF-transition threshold. Therefore, phenomena specific to radiation such as radiation induced diffusion, dopant grain boundary desegregation, and ion beam mixing are necessary to cause the grain growth observed in the ordered grain boundary sample, and may also ultimately degrade the stability of the AIF-containing sample.

The ability of AIFs to improve the grain boundary network sink efficiency and limit grain growth breaks down in the 200 °C ex situ irradiation, where the AIF-containing sample behaved the same as the ordered grain boundary sample. Both had a similar defect number density and degree of grain growth within the projected beam range. This breakdown can be attributed to the metastable nature of an AIF quenched into place resulting in a complexion transition. AIFs are only the thermodynamically preferred grain boundary state at temperatures of at least 60-85% of the material melting temperature [57, 84]. At 200 °C, the preferred grain boundary state is crystalline, where indications of a complexion transition from an ordered grain boundary to an AIF in Cu-Zr have only been observed between 750 °C and 850 °C [54, 74]. All samples subjected to ex situ irradiation were exposed to the same dose at the same time and therefore the same degree of irradiation induced heating. The combined effects of the ion irradiation, irradiation induced heating, and 200 °C stage temperature were sufficient to push enough AIFs out of their metastable state, causing them to crystallize and form ordered grain boundaries and noticeably change the

material radiation tolerance to be more like the ordered grain boundary sample. It is important to note that AIFs may still remain distributed throughout the grain boundary network in the AIF-containing sample irradiated at 200 °C, but not enough to cause a cumulative impact on behavior, and hence the observed grain growth. Instead, the combined effects of only the ion irradiation and irradiation induced heating performed at 25 °C does not appear sufficient to disrupt enough AIFs out of their metastable state to cumulatively change the radiation tolerance. This means that complexion transitions can be used to favorably tune the radiation tolerance of nanocrystalline alloys. Radiation conditions that promote AIF formation, such as very hot operating temperature within the AIF forming regime, may cause a counterintuitive increase in grain size stability and radiation tolerance.

5.4 Conclusion

Three observations are made from the nanocrystalline alloy irradiation experiments performed in this study. First, AIFs increase the net sink efficiency of the entire grain boundary network. This is evidenced by the AIF-containing samples having a smaller defect area density measured from the in situ TEM irradiation video and a lower defect number density measured from 25 °C ex situ irradiation compared to the ordered grain boundary samples. Second, AIFs limit grain growth during irradiation. This is evidenced by the absence of grain growth in the AIF-containing sample during in situ TEM irradiation, and less grain growth measured in the AIF-containing sample from the 25 °C ex situ irradiation compared to the ordered grain boundary samples. Third, complexion transitions due to radiation conditions change the radiation tolerance. This is evidenced by the divergence in behaviors observed in the irradiation performed at 200 °C compared to 25 °C.

A main challenge for nanocrystalline metal irradiation is a loss of radiation tolerance due to grain growth, which is further exacerbated by high temperature operating conditions. In nanocrystalline Cu-Zr, the transformation of an ordered grain boundary network to an AIF-containing network improved the net grain boundary network sink efficiency and limited grain growth that in turn improved the radiation tolerance. Additionally, AIFs operate best at extremely high temperatures, making AIFs a promising prospect for improved radiation tolerance in high temperature nuclear applications. The grain boundary network as a whole can be used to improve the radiation tolerance of nanocrystalline alloys by including a proportion of extremely sink efficient and stable grain boundaries through complexion transitions for cumulative radiation tolerance improvements.

Chapter 6: Conclusions

In nanocrystalline metals, engineering the structure and composition of the grain boundaries is critical in order to realize the full potential of these materials, but methods to do this remain limited. Complexions offer a powerful perspective that considers grain boundaries as phase-like entities that can undergo dramatic transitions in composition and structure depending on external variables such as temperature and composition, similar to bulk phases. Using this perspective, different complexion types have been found to significantly alter material behavior. AIFs, a premelt type of complexion that forms at very high temperatures, have been shown to significantly improve damage tolerance, but alloys known to form them are extremely few. Due to their scarcity, application studies of AIFs are also limited. The goal of this thesis was to enable AIF research by formalizing selection criteria to find nanocrystalline alloys that can form these features, and then investigate applications where AIF damage tolerance can be leveraged. The relevant conclusions of this thesis are summarized below.

In Chapter 2, we proposed a set of materials selection rules aimed at predicting the formation of AIFs, with an emphasis on encouraging (1) the segregation of dopants to the grain boundaries and (2) the formation of a glassy structure. To validate these predictions, binary Cu-rich and Ni-rich metallic alloys encompassing a range of thermodynamic parameter values were created using sputter deposition and subsequently heat treated to allow for transformation of the boundary structure. All of the alloys studied had dopant segregation to the grain boundary, but exhibited different interfacial structures. Cu-Zr, Cu-Hf, and Ni-Zr formed AIFs while Cu-Nb and Cu-Mo retained crystalline order at their grain boundaries, which can mainly be attributed to differences in ΔH^{mix}. We find that a positive ΔH^{seg} coupled with a negative ΔH^{mix} promotes

nanoscale AIF formation, and using these selection rules, we made AIF-forming predictions for a wide variety of transition metal binary alloys.

In Chapter 3, we applied these selection rules to discover a new AIF-forming alloy, and further populated the AIF materials toolbox. Nanocrystalline Ni-W annealed at 1000 °C and above, and then rapidly quenched is found to contain AIFs. Solute segregation is used to limit grain growth in nanocrystalline metals, but this stabilization often breaks down at high temperatures. AIFs provide a possible alternative route to lower grain boundary energy and therefore limit grain growth specifically at high temperatures where they are thermodynamically accessible. Using this, we discovered a counterintuitive region of nanocrystalline stability at elevated temperatures due to AIF formation, highlighting the unexpected benefits possible using the complexion perspective.

Upon defining material selection rules for nanocrystalline alloys that can form AIFs, we then investigated applications where AIF damage tolerance can be best utilized. Nanocrystalline metals typically have high fatigue strengths, but low resistance to crack propagation. AIFs have been shown to diffuse grain boundary strain concentrations during monotonic loading, suggesting they may also be beneficial for fatigue properties. In Chapter 4, we probed this hypothesis using in situ TEM fatigue cycling on Cu-1 at.% Zr thin films thermally treated to have either only ordered grain boundaries or to contain AIFs. The sample with only ordered grain boundaries experienced grain coarsening at crack initiation followed by unsteady crack propagation and extensive nanocracking, whereas the sample containing AIFs had no grain coarsening at crack initiation followed by steady crack propagation and distributed plastic activity. We find that microstructural design for control of these behaviors through simple thermal treatments can access new modes of nanocrystalline metal fatigue toughness.

Damage tolerance is also an important consideration for nuclear radiation applications. The radiation tolerance of metals can be improved through the incorporation of surfaces and interfaces within the material, and AIFs are predicted to have improved sink efficiencies compared to traditional ordered grain boundaries due to their increased effective thickness and amorphous structure. In Chapter 5, ball-milled nanocrystalline Cu-Zr heat treated to either have only ordered grain boundaries or to contain AIFs distributed throughout the grain boundary network were subjected to in situ TEM irradiation and ex situ bulk irradiation. Differences in defect densities and grain growth due to grain boundary structural transitions were then investigated. We found that when AIFs are incorporated within a material, not only is the net sink efficiency of the whole grain boundary network increased, but grain growth is also limited, leading to improved nanocrystalline alloy radiation tolerance.

In summary, we found that AIFs are not obscure features relegated to theory and exotic forming conditions. Instead, AIFs can possibly be found in a large number of alloys through simple heat treatments. Furthermore, AIFs are ideal candidates to improve nanocrystalline alloy behaviors in certain extreme environments. They naturally form close to the melting point, leading to a counterintuitive increase in grain size stabilization at high temperatures. AIFs are also desirable when damage tolerance is key, such as in fatigue and nuclear radiation applications. While grain size is the standard metallurgical parameter, the large grain boundary volume fraction of nanocrystalline metals necessitates new perspectives. In addition to grain size, the nature of the grain boundary network is critical to fully understanding and engineering nanocrystalline metals. Complexions offer a unique perspective to achieve this, and AIFs exemplify the unexpected, beneficial, and unleveraged behaviors possible in nanocrystalline metals using this approach.

Chapter 7: Directions for Future Work

This thesis has taken AIFs from thermodynamic peculiarities to viable and desirable engineering design goals. However, several gaps exist in our understanding of AIFs. Future AIF research should be directed in the following specific areas.

- *Proving that the AIFs observed in this study are true complexions*. A complexion has a very specific definition and is not a generalized term for any general grain boundary. Grain boundaries called complexions have special phase-like behaviors, meaning the grain boundary structure and composition are reversible depending on extrinsic parameters such as temperature and composition. The AIFs in this thesis can at most be surely called premelts, but their unique complexion behavior remains to be proven. In situ TEM heating that shows reversible AIF formation and dissolution above and below the transition temperature would definitively prove the complexion nature of the AIFs observed in this thesis. Efforts to do this were performed during this thesis, but solid state dewetting during in situ TEM heating posed a significant challenge to obtain useful data. More information regarding these efforts can be found in Appendix A.
- *AIF formation dependence on grain boundary character*. Complexions cannot simply be called phases since they violate the Gibbs technical definition for a phase where their existence is dependent on their local environment. That is, the grain boundary feature would cease to exist if the neighboring grains were altered. This unique dependency on gran boundary energy, and in turn grain boundary character, earns these features their unique complexion moniker. Therefore, improved understanding of the connection between grain boundary energy/character, AIF formation, and the role of AIFs within the greater grain boundary network is critical. Efforts were made during this thesis to connect

grain boundary character to AIF formation using precession electron diffraction and TKD, but obtaining all five parameters of the grain boundary character in a nanocrystalline alloy proved extremely challenging. Bicrystal/coarse-grained samples or novel AIF inspection techniques such as atomic force microscopy (AFM) or 3D X-ray diffraction (3D XRD) could enable this study.

- *Novel AIF inspection methods*. High resolution TEM is currently the only experimental method available to find AIFs in nanocrystalline alloys. New methods to show that AIFs have formed in an alloy could both ease alloy AIF-formation screening, and open new analysis pathways. AFM has been a cornerstone experimental method for complexion research, where the grain boundary energy, and hence complexion transitions, can be directly investigated by measuring grain boundary grooving [80, 258]. Grain boundary grooves were observed on the surface of the Ni-W films presented in Chapter 3, and may be used with AFM to investigate AIF formation. Amorphous regions within a material are also detectable using XRD as a signature hump. Synchrotron XRD may be able to resolve AIF formation using this amorphous signature. Finally, AIFs may also noticeably impact electrical and thermal conductivity, allowing measurement of these criteria to indicate changes in the grain boundary network. For example, concurrent four-point probe electrical measurement during heating could pinpoint AIF formation as jumps in resistivity. The possibility of such an experiment is described in greater detail in Appendix D.
- *The role of impurities during AIF formation*. Many of the processes used to create nanocrystalline alloys are subject to impurity contamination, such as H, He, O, N, C and S. These impurities are known to significantly impact material behavior and even segregate to grain boundaries, but inadequate attention is being paid to these contaminants.

In fact, many nanocrystalline alloy grain size stability studies have been performed without characterizing these impurities where they are likely significantly contributing to the observed stability. Furthermore, such impurities at the grain boundaries would likely promote AIF formation since they would frustrate the formation of long range order. Understanding the importance of these impurities on AIF formation are necessary for continued AIF application.

- *Alloys that form AIFs at lower temperatures*. While hot and extreme environments are strong applications for AIFs, high temperatures are relative. Now that the utility of AIFs in such environments has been shown in this thesis, new alloys that form AIFs at lower temperatures can be explored. In doing this, AIFs can be investigated in more manageable temperature regimes that do not limit experimentation. For example, the Cu and Ni alloys used in this thesis pushed the upper temperature limits of the tube furnace used for annealing. Also, the radiation experiments performed at Sandia National Laboratories had a maximum operation temperature of ~400 °C. Alloys with lower melting points where ~400 °C is within the AIF forming range would allow radiation to be performed when AIFs are in their true thermodynamically preferred regime, and not simply metastable. Such limitations hold true for many experimental configurations, where maximum temperatures usually top out at ~500 °C. Performing radiation or mechanical test experiments when AIFs are in their preferred thermodynamic state and not simply metastable would offer critical insights regarding the behavior of these features under potential operating conditions. Al or Sn based alloys have low melting points and are ideal candidates to explore for this purpose. Al-Mg and Sn-Ag both satisfy the selection criteria identified in Chapter 2, and they are both relevant engineering alloys. Al-7 at.% Mg was recently found

to be one of the strongest lightweight alloys ever reported [259], and Sn-Ag is an industry standard Pb-free solder for computer chips [260]. More details regarding the use of Sn-Ag for this application can be found in Appendix D.

In addition to expanding AIF theoretical understanding, a number of non-AIF research paths naturally arise from this thesis. Future work connected to this thesis should be directed in the following areas.

- *Continued in situ TEM fatigue of ordered grain boundary nanocrystalline metals*. The novel thin film annealing method used in conjunction with in situ TEM fatigue described in Chapter 4 opens new nanocrystalline fatigue research pathways. Previous in situ TEM nanocrystalline fatigue experiments were limited to pure metals in their as-sputtered state. The method used in this thesis allows improved in situ TEM inspection of the impact grain boundary doping has on nanocrystalline fatigue behaviors. For example, it can be determined if thermodynamic grain size stabilization due to dopant segregation changes the rate of grain growth during fatigue crack initiation. Perhaps an ideal fatigue loading-composition-grain size window exists where grain growth at the site of crack initiation perpetually impedes crack initiation and growth, akin to a single-crystal always existing locally in front of the crack.
- *Continued irradiation studies of nanocrystalline alloys*. While grain size stabilization is necessary for nanocrystalline metals in radiation applications, dopant segregation may actually decrease alloy radiation tolerance. The results of this thesis and other studies correlate improved radiation tolerance to increased free volume at the grain boundary. Dopant segregation reduces this free volume and may in turn degrade radiation tolerance.

Studies investigating the impact of dopant grain boundary segregation on nanocrystalline alloy irradiation are necessary.

- *Complexion "composites."* Due to their large grain boundary volume fraction, nanocrystalline metals can almost better be viewed as grain-grain boundary "composites," and complexions offer a unique perspective to tune the grain boundary portion of these nanocrystalline "composites." For example, the AIF-containing alloys studied in this thesis are essentially metal-metallic glass composites, with the glassy component restricted to the grain boundary. This perspective of "composite" nanocrystalline alloys tailored by complexions can be extended to constitute materials other than glassy AIFs. For example, carbon has been shown to segregate to grain boundaries in certain alloys [261, 262], and segregated dopant can form bilayer complexions [64]. Given the appropriate hexagonal ring structure of carbon atoms situated within the grain boundary lattice, a bilayer graphene complexion could form. Dopant grain boundary superstructures reminiscent of hexagonal ordering have been found in Ni-Bi bilayer complexions [263], and graphene-metal oxide particle composites have already been created [264, 265].

Appendix A: Deposition and Annealing of the Sputtered Films

The microstructures of metal films fabricated through sputter deposition are dependent on the power, pressure and temperature parameters used during sputter. The sputtered films used here were deposited in accordance with power-pressure-temperature sputter design rules to achieve a dense nanocrystalline film with columnar grains [266]. Zone 1 is characterized by porous crystallites separated by voids, and Zone T has densely packed but fibrous grains. Efforts were made to avoid Zone 1 and Zone T in accordance with Thornton's Structure Zone Diagram shown in Figure A.1. The target region is Zone 2, which is characterized by dense columnar grains, and is achievable using low deposition pressures at high temperatures. A low deposition rate was also used to further promote film densification. The films were ultimately deposited using an Ar pressure of 1.5 mTorr at a temperature of 400 °C, which is the maximum temperature capable on the Ulvac sputter tool. The powers used were 150W for Cu and 75 W for Zr, where the Cu target was sputtered using DC power, and the Zr using RF. The balance of these metals, at these powers, using each power source, resulted in a film with ~4 at.% Zr. The deposition rate was ~0.2 nm/sec.

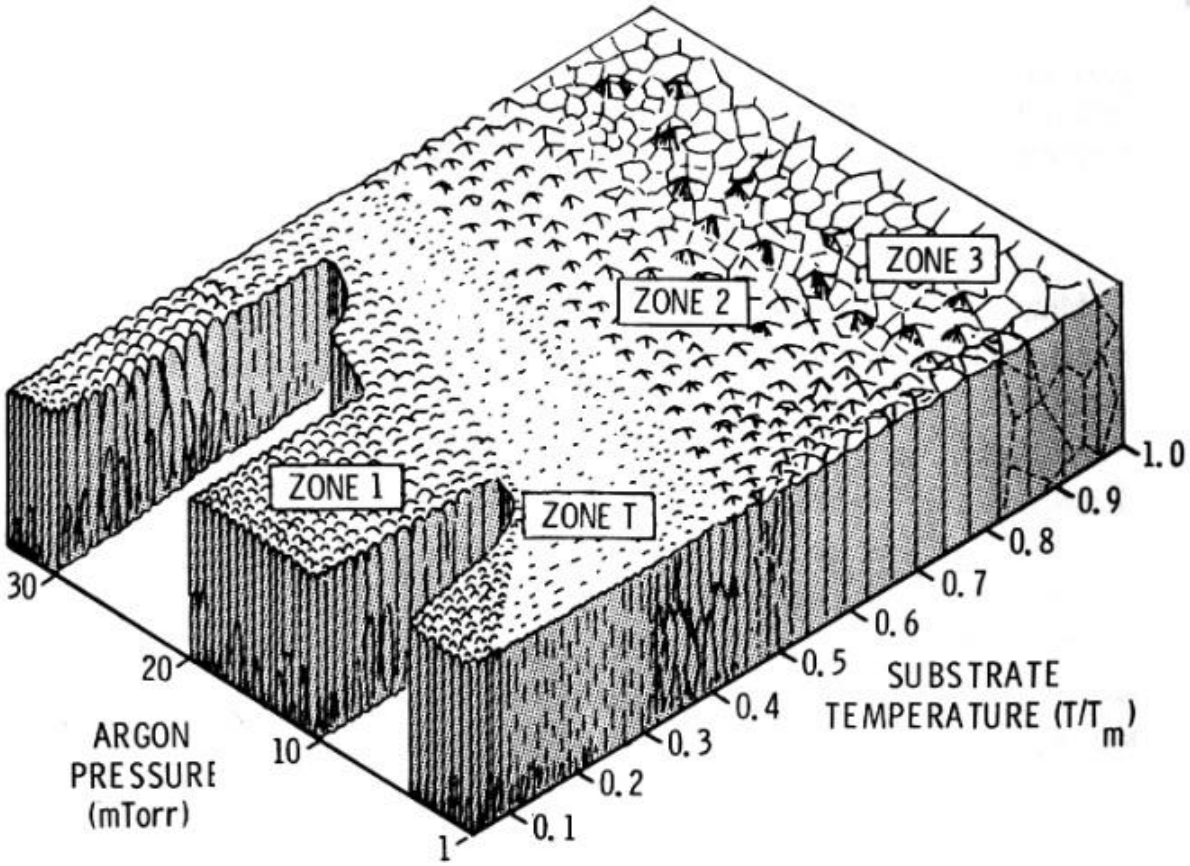

Figure A.1. Diagram of sputter microstructure zones as a function of pressure and temperature, from [266].

The maximum sputter temperature, 400 °C, is only ~40% of the Cu-Zr melting point, meaning the microstructure is still somewhat within Zone T. This may cause porosity between the columnar grains and enhance surface roughness. The Cu substrate further promoted surface roughness, since even though it was polished down to 0.1 μm grit colloidal silica, the surface is still not atomically smooth. Originally, Si was the desired substrate since single crystal wafers can be used to automatically achieve atomically smooth deposition surfaces, but Cu both chemically reacts and diffuses into Si at high temperatures. Efforts were made to find barrier layers suitable to prevent chemical reactions and diffusion of the Cu film, but all barriers evaluated could not survive the >900 °C annealing necessary for this AIF research.

This surface roughness contributed to solid state dewetting that greatly challenged proper heat treatments of the sputtered films for AIF transformations. Solid state dewetting commonly occurs in any thin film at high temperatures, but can be exacerbated by surface roughness. The films were first annealed to 500 °C for 1 day in order to relieve film stresses, allow for film densification, promote dopant segregation, and permit grain growth to ease TEM inspection, but an additional higher temperature anneal is necessary to permit AIF grain boundary transitions. Previous ball-milled Cu-Zr AIF studies were annealed at 950 °C and then quenched, but this temperature caused excessive dewetting and destruction of sputtered Cu-Zr films within seconds. As result, annealing for AIF transitions in the sputtered Cu-Zr films was lowered to 900 °C, where ~850 °C is the known lower limit for AIF formation in Cu-Zr. Also, the 900 °C anneal before quenching was limited to 60 seconds, where even 90 seconds caused almost complete film destruction. Images of solid state dewetting in the annealed films are shown in Figure A.2.

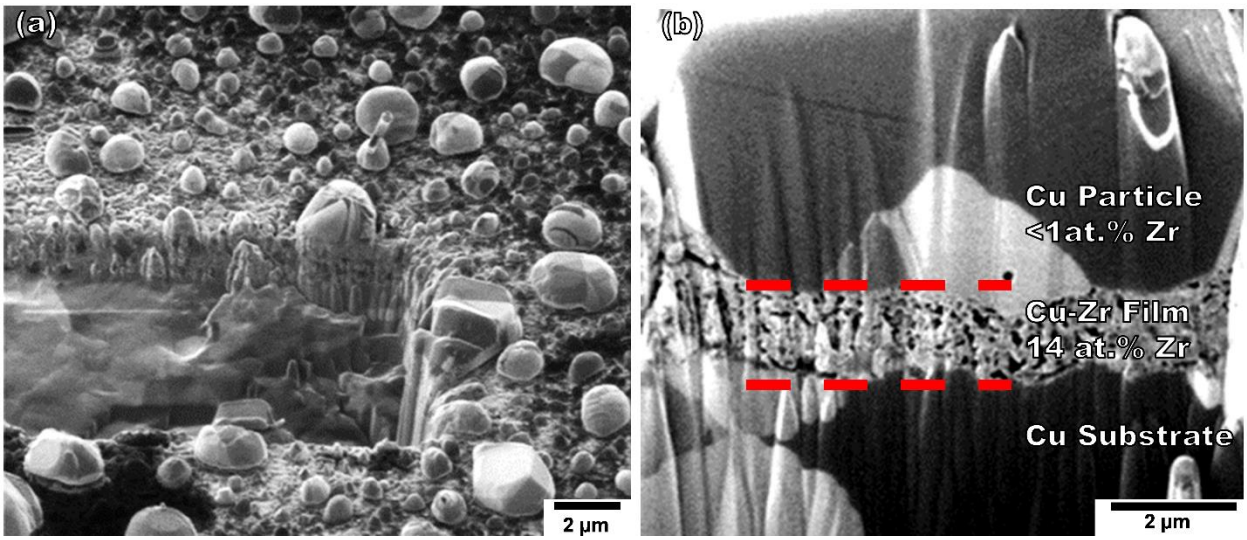

Figure A.2. Focused ion beam channeling contrast imaging of the Cu-5 at.% Zr thin film deposited on a copper substrate after being annealed at 500 °C for 24 h and then 900 ° C for 2 min with subsequent quenching. (a) shows dewetted Cu particles containing large grains dispersed across the film surface. (b) shows another focused ion beam channeling contrast imaging from a separate trench where the porous remains of the sputtered film can be seen beneath a dewetted particle. The insets in (b) show the associated compositional data for the film and particle.

Solid state dewetting is the current primary challenge for in situ TEM heating experiments to definitively prove AIF complexion transitions. Figure A.3 shows the destruction of an electron transparent film during in situ TEM heating due to solid state dewetting. All electron transparent samples, even if prepared from bulk specimens, are subject to solid state dewetting due to their thin geometry necessary to permit TEM inspection essentially making them thin films. Efforts during this thesis to perform in situ TEM heating to observe AIF complexion transitions found that solid state dewetting initiates at ~500 °C in Cu-Zr. Dewetting was observed using both Gatan and Protochips TEM heating holders, regardless of substrate (Mo grids, Cu grids, Si_3N_4 support window grids, and Protochips with open holes were all evaluated). Slow heating ramp rates, minimized AIF transitions temperatures, minimized film compositions, and minimized electron beam exposure were observed to suppress solid state dewetting in Cu-Zr and allow regions of the electron transparent film to remain usable. Ramping rates of ~0.2 °C/s to a temperature of 850 °C (current known lower AIF transition limit for Cu-Zr) were used to create the annealed AIF-containing films in Chapter 4. Cu-1 at.% Zr was also chosen in Chapter 4 to minimize the Zr composition, since higher dopant compositions increase film roughness and exacerbate dewetting. Electron beam exposure is also known to alter the behavior of thin films during in situ TEM heating, with an example shown in Figure A.4.

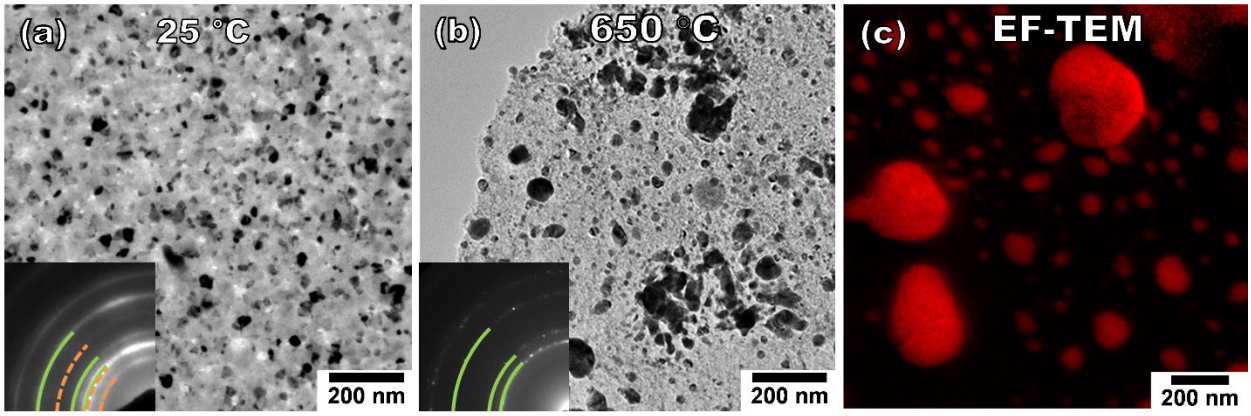

Figure A.3. Evolution of solid state dewetting in Cu-Zr with increasing temperature. The bright-field transmission electron microscopy (TEM) image in (a) shows the film in the as-deposited state at 25 °C, and (b) shows the film after annealing at 650 °C. The insets show the associated selected area electron diffraction patterns for each condition, where the face-centered cubic Cu phase is indicated by solid green lines, and the Cu_2O phase by dashed orange lines. Elemental mapping using energy filtered (EF) TEM on a separate region of the annealed film is shown in (c) where Cu is red.

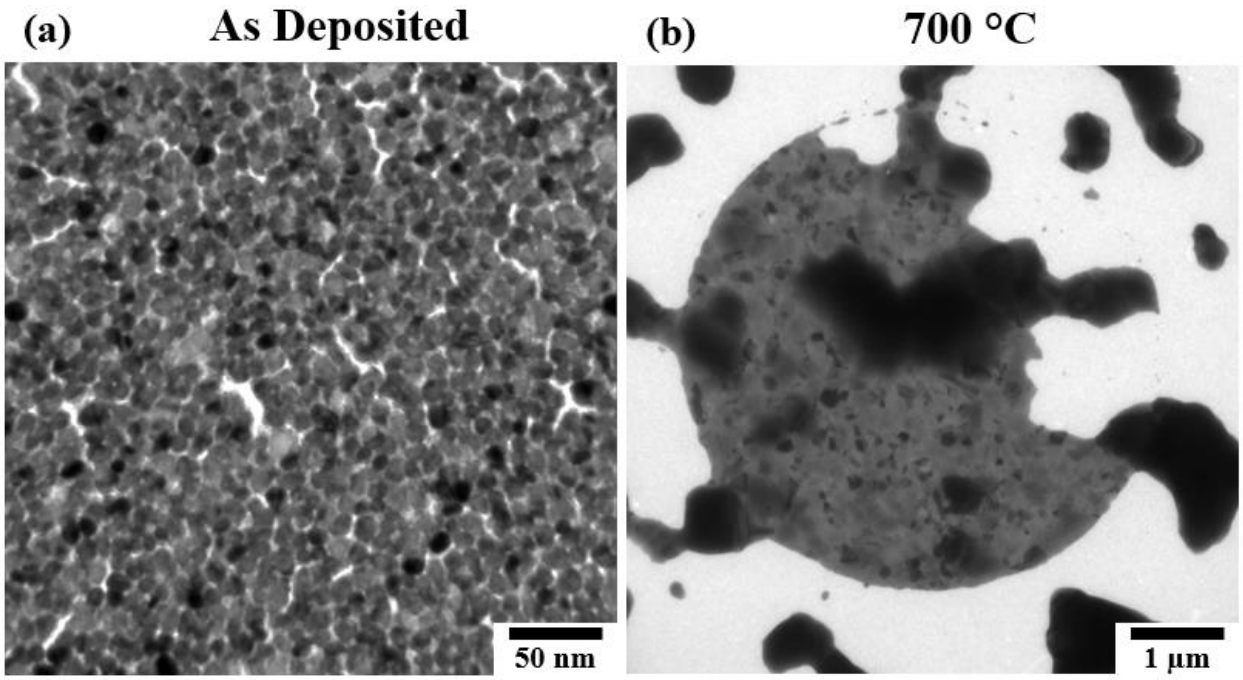

Figure A.4. Pure Cu deposited onto a Si_3N_4 support TEM grid and in situ TEM annealed to 700 °C. The thin film fully dewetted except within the electron beam spot area used during annealing, likely caused by an oxide layer on the Cu surface grown by the electron beam [244] which limited surface diffusion [242] and thus solid state dewetting.

Appendix B: Additional Experimental Details of the In Situ Transmission Electron Microscopy Fatigue Research

B.1 Supplementary Note 1

Cu-1 at.% Zr thin films were sputter deposited onto NaCl polished disc substrates 13 mm × 1 mm in dimension (International Crystal Laboratories, Inc. #0002A-4549). Portions of the film were then floated by dissolution of the substrate in a solution of water and isopropyl alcohol onto Protochips, Inc. Fusion heating chips with no supporting membrane (Protochips, Inc. #E-FHBN-10), where special care taken to not short the opposing electrical leads on either side of the heating chip window with the floated film. A small amount of Cu oxide was seen in some samples after high vacuum annealing to create the ordered and disordered samples and may be due to film interactions with the salt substrate or dissolution in water.

After annealing, portions of the film located on the heating chips were prepared for in situ TEM fatigue using a focused ion beam (FIB) lift-out technique. Portions of the annealed films chosen for lift-out were in the center of the heating chip with good contact to the window to ensure adequate thermal transfer. Figure B.1(a) shows a scanning electron microscopy (SEM) image of the thin film on a heating chip over the window holes with good thermal contact. Figure B.1(b) shows rectangles approximately 15 nm × 15 nm cut using FIB and lifted out through Pt attachment to an Omniprobe, Inc. micro-manipulator visible on the left. Next, the samples were placed across the 2.5 μm wide gauge section of the push-to-pull (PTP) device indicated by the red arrow in Figure B.1(c) and secured with electron and ion beam Pt, with final FIB sample and notch shaping shown in Figure B.1(d). Special care was taken during Pt deposition to (1) maximize the distance of the attaching Pt from the gauge section and (2) avoid imaging after deposition until base pressure was recovered in order to minimize inadvertent Pt deposition over the gauge section. If these

measures were not taken, enough accidental Pt deposition occurred to destroy electron transparency over the gauge area and make mechanical testing of the experimental specimen inconclusive. The PTP devices are from the Bruker Corporation with a stiffness of 450 N/m (Bruker Corporation #5-1092-HIGH-10) and were attached to the Bruker PI 95 PicoIndenter TEM holder Cu mount using conductive silver paint. Gluing was completed before lift-out of the sample from the heating chip onto the PTP device in order to minimize handling of the completed sample, where even the slightest vibration or pressure on the PTP device can break the extremely delicate sample once stretched across the gauge section.

The methodology used minimizes FIB damage since the deposited film thickness was sufficiently electron transparent with no further FIB thinning required, indicated by the increased brightness of the thin film over the gauge region in Figure B.1(d). Also, the thin film is in the correct orientation for transfer from the heating chip to the PTP device, which eliminates the geometric challenge faced when using a standard vertical lift-out technique for TEM sample preparation to create a plan view specimen. Other methods to minimize FIB damage or achieve a plan view lift-out have been investigated in the literature [157, 267, 268].

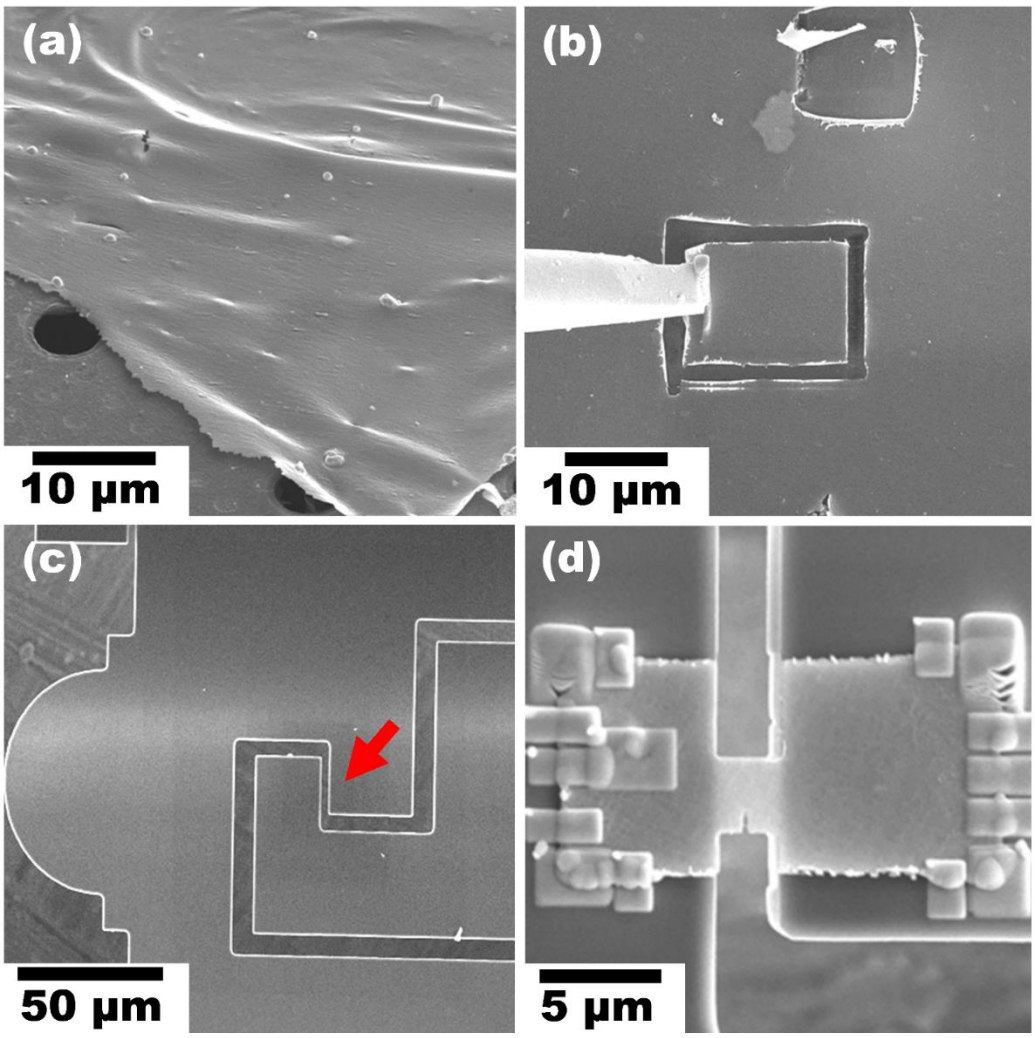

Figure B.1. (a) A scanning electron microscopy image of the Cu-1 at.% Zr thin film that has been floated onto the heating chip window area where the heating chip holes are visible. (b) shows a selected portion of the annealed thin film cut into a rectangle using the focused ion beam (FIB) technique and Pt attached to the micro-manipulator on the left for lift-out. (c) shows the push-to-pull device with the gauge section indicated by the red arrow. (d) shows the finished specimen, attached with Pt and shaped using the FIB.

B.2 Supplementary Note 2

Electron energy loss spectroscopy (EELS) was performed using a JEOL GrandARM300CF in scanning transmission electron microscopy (STEM) mode operated at 300 kV in order to compute the thickness of the as-deposited Cu-1 at.% Zr thin film. The thickness was calculated using the log-ratio (absolute) method with a measured convergence semi-angle of 31.0 mrad and

collection semi-angle of 39.4 mrad. An effective atomic number of 29 was used due to the low Zr dopant concentration. The as-deposited thin film is shown using bright field transmission electron microscopy (TEM) in Figure B.2(a) and high angle annular dark field STEM in Figure B.2(b), where the dashed red line in Figure B.2(b) shows where the thickness measurement was performed. Figure B.2(c) shows the thickness profile with an average film thickness of 51 ± 6 nm.

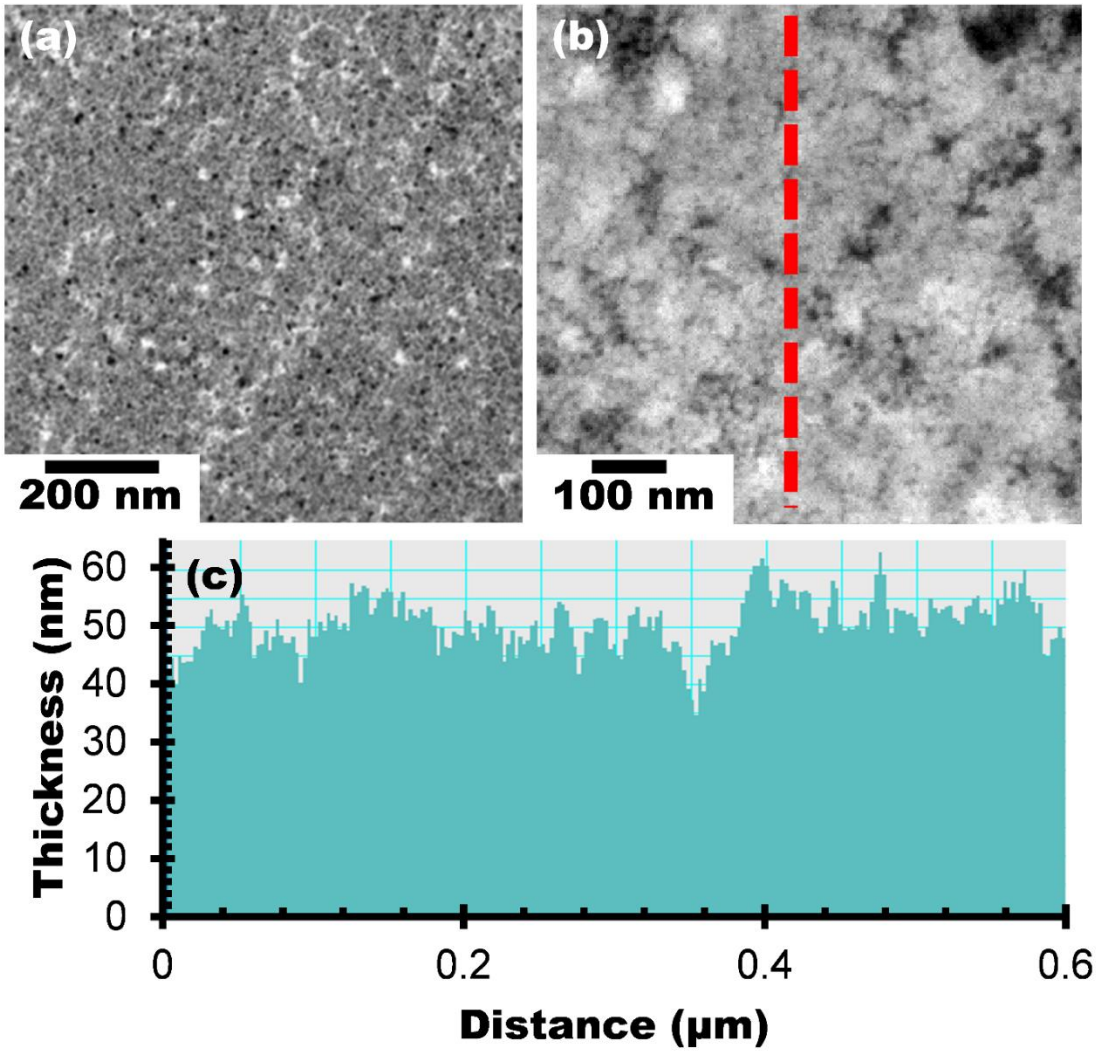

Figure B.2. The as-deposited Cu-1 at.% Zr thin film is shown using (a) bright field transmission electron microscopy and (b) high angle annular dark field scanning transmission electron microscopy. The film thickness was measured at the dashed red line in (b), with data presented in (c).

B.3 Supplementary Note 3

The full in situ TEM fatigue loading conditions and crack growth data for the ordered grain boundary and AIF-containing samples are presented in Tables B.1 and B.2, where sample fracture occurred at the final steps. Reported loads are on the total system including both the PTP device and specimen. The notch plus crack length, a, is normalized by the specimen width, W. da/dN is the crack growth rate measured as the change in crack length per number of cycles. Step 45 of the ordered sample was performed at a lower total mean load than step 44 due to the fatigue test being paused and then resumed. A representation of these loading conditions is shown in Figure B.3 for the ordered grain boundary sample where the total mean load is plotted and the vertical bars represent the total load amplitude. Figure B.4 shows the loading conditions within an individual step in greater detail using step 17 from the AIF-containing sample as an example for the load and displacement versus step time duration in Figures B.4(a) and (b) respectively. The 200 Hz loading rate causes the curves to appear as solid black boxes.

Ordered Grain Boundary Sample							
Step	**Frequency (Hz)**	**Duration (s)**	**Mean Load, Total (μN)**	**Load Amplitude, Total (μN)**	**Crack Length, *a* (μm)**	**Normalized Crack Length, *a/W***	**Crack Growth Rate, *da/dN* (m/cyc)**
0	100	200	10	5	1.000	0.303	NA
1	100	200	10	5	1.004	0.304	NA
2	100	200	20	5	1.009	0.306	2.8E-13
3	100	200	30	10	1.015	0.308	2.7E-13
4	100	200	40	10	1.022	0.310	2.4E-13
5	100	200	50	15	1.024	0.310	3.9E-13
6	100	200	60	20	1.028	0.312	4.6E-13
7	100	200	70	20	1.051	0.318	4.6E-13
8	100	200	80	30	1.055	0.320	3.2E-13
9	150	200	80	30	1.062	0.322	2.6E-13
10	200	200	80	30	1.069	0.324	3.1E-13
11	200	200	80	30	1.086	0.329	4.4E-13
12	200	200	80	30	1.102	0.334	4.7E-13
13	200	200	80	30	1.134	0.344	4.0E-13
14	200	200	90	30	1.139	0.345	2.8E-13
15	200	200	90	30	1.148	0.348	1.2E-13
16	200	200	90	30	1.151	0.349	1.3E-13
17	200	200	100	30	1.153	0.349	1.2E-13
18	200	200	100	30	1.162	0.352	1.4E-13
19	200	200	100	30	1.165	0.353	3.3E-13
20	200	200	110	30	1.172	0.355	5.2E-13
21	200	200	110	30	1.214	0.368	6.7E-13
22	200	200	110	30	1.242	0.376	6.1E-13
23	200	200	120	30	1.265	0.383	3.7E-13
24	200	200	120	30	1.270	0.385	2.1E-13
25	200	200	120	30	1.273	0.386	1.4E-13
26	200	200	130	30	1.280	0.388	4.5E-13
27	200	200	130	30	1.288	0.390	6.2E-13
28	200	200	130	30	1.352	0.410	5.9E-13
29	200	200	140	30	1.360	0.412	4.3E-13
30	200	200	140	30	1.362	0.413	1.4E-13
31	200	200	140	30	1.370	0.415	1.5E-13
32	200	200	150	30	1.376	0.417	2.0E-13
33	200	200	150	30	1.384	0.419	2.2E-13
34	200	200	150	30	1.396	0.423	5.0E-13
35	200	200	160	30	1.405	0.426	6.2E-13
36	200	200	160	30	1.466	0.444	5.9E-13
37	200	200	160	30	1.472	0.446	4.3E-13
38	200	200	170	30	1.479	0.448	9.5E-13
39	200	200	170	30	1.485	0.450	1.4E-12
40	200	200	170	30	1.650	0.500	1.4E-12
41	200	200	180	30	1.660	0.503	9.6E-13

42	200	200	180	30	1.662	0.504	2.0E-12
43	200	200	180	30	1.670	0.506	2.3E-12
44	200	200	180	30	NA	NA	NA
45	200	200	80	30	NA	NA	NA
46	200	200	90	30	2.115	0.641	2.3E-12
47	200	200	100	30	2.126	0.644	2.0E-12
48	200	200	110	30	2.132	0.646	9.3E-13
49	200	200	120	30	2.155	0.653	1.3E-12
50	200	200	130	30	2.287	0.693	1.9E-12
51	200	200	140	30	2.306	0.699	5.4E-12
52	200	200	150	30	2.440	0.739	NA
53	200	200	160	30	3.158	0.957	NA

Table B.1. The loading parameters per step of the ordered grain boundary sample in situ transmission electron microscopy fatigue and associated crack growth data.

AIF-Containing Sample							
Step	**Frequency (Hz)**	**Duration (s)**	**Mean Load, Total (μN)**	**Load Amplitude, Total (μN)**	**Crack Length, *a* (μm)**	**Normalized Crack Length, *a/W***	**Crack Growth Rate, *da/dN* (m/cyc)**
0	100	200	10	5	1.000	0.294	NA
1	100	200	10	5	1.024	0.301	NA
2	100	200	20	5	1.051	0.309	1.2E-12
3	100	200	30	10	1.066	0.314	1.7E-12
4	100	200	40	10	1.100	0.323	2.2E-12
5	100	200	50	15	1.173	0.345	2.2E-12
6	100	200	60	20	1.221	0.359	2.1E-12
7	100	200	70	20	1.226	0.361	2.0E-12
8	100	200	80	30	1.285	0.378	1.6E-12
9	150	200	80	30	1.357	0.399	1.5E-12
10	200	200	80	30	1.372	0.403	1.7E-12
11	200	200	80	30	1.436	0.422	1.8E-12
12	200	200	80	30	1.566	0.461	2.0E-12
13	200	200	80	30	1.616	0.475	1.7E-12
14	200	200	90	30	1.676	0.493	1.2E-12
15	200	200	90	30	1.717	0.505	1.7E-12
16	200	200	90	30	1.763	0.519	1.7E-12
17	200	200	100	30	1.905	0.560	1.5E-12
18	200	200	100	30	1.929	0.567	1.1E-12
19	200	200	100	30	1.940	0.571	8.8E-13
20	200	200	110	30	1.968	0.579	1.1E-12
21	200	200	110	30	2.062	0.606	1.8E-12
22	200	200	110	30	2.088	0.614	NA
23	200	200	120	30	2.223	0.654	NA

Table B.2. The loading parameters per step of the amorphous intergranular film (AIF) containing sample in situ transmission electron microscopy fatigue and associated crack growth data.

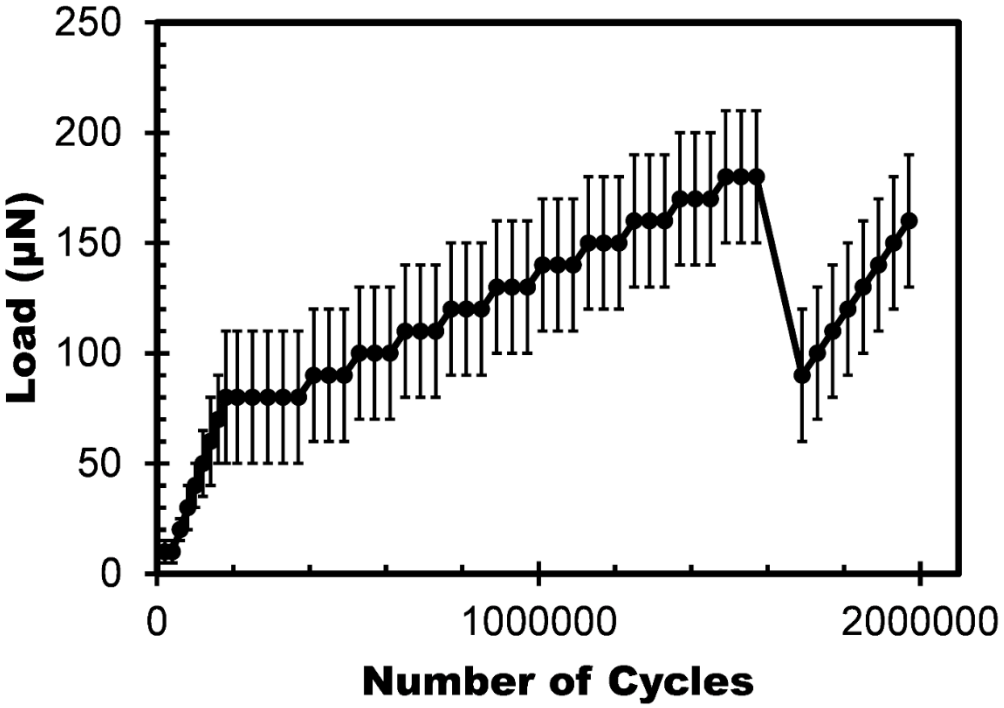

Figure B.3. The loading conditions of the ordered grain boundary sample for each step are shown where the total mean load is plotted and the vertical bars represent the total load amplitude for each step. The drop at 1,690,000 is due to the fatigue cycling being paused and then resumed. The amorphous intergranular film containing sample received identical loading conditions through to its point of failure.

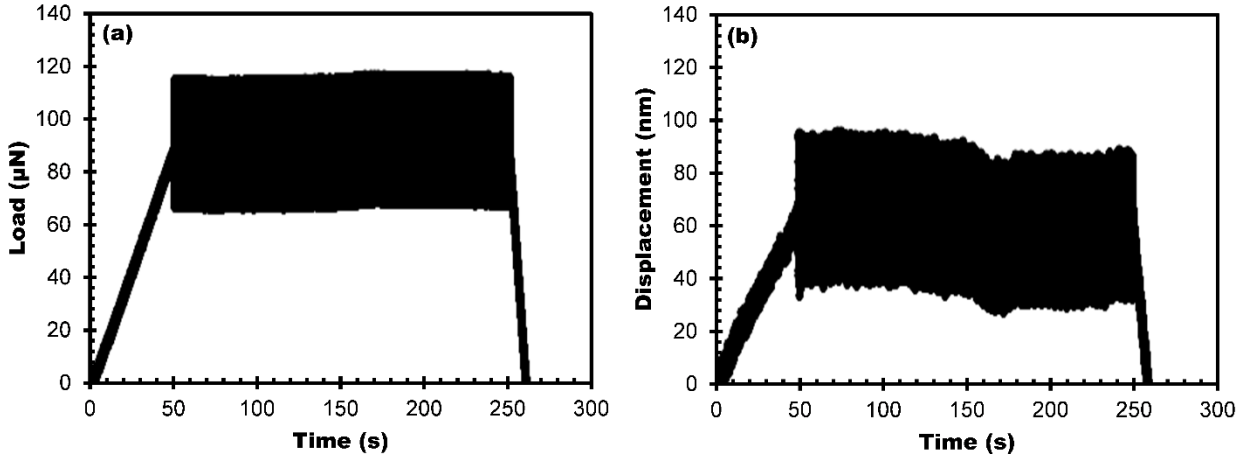

Figure B.4. Representative (a) load and (b) displacement curves from the amorphous intergranular film fatigue cycling at loading step number 17. The 200 Hz loading rate causes the curves to appear as solid black boxes.

Appendix C: Additional Details Regarding the Radiation Experiments

C.1 Additional Experimental Details

- Particles of the ball-milled powder were affixed onto Si carriers in the irradiation chamber using carbon tape for the 25 °C irradiation and M-Bond 610 adhesive for the 200 °C irradiation for greater adhesive temperature stability.
- The thicknesses of each electron transparent TEM sample measured using EELS are shown in Table C.1.

Electron Transparent Sample	**Average Thickness and std. dev. (nm)**
Ordered GB, in situ irradiation	86 +/- 11
AIF-Containing, in situ irradiation	103 +/- 10
Ordered GB, ex situ irradiation, 25 °C	100 +/- 15
AIF-Containing, ex situ irradiation, 25 °C	123 +/- 20
Ordered GB, ex situ irradiation, 200 °C	147 +/- 10
AIF-Containing, ex situ irradiation, 200 °C	132 +/- 22

Table C.1. Thickness of each electron transparent transmission electron microscopy sample measured using electron energy loss spectroscopy used to calculate defect cluster area and number densities

C.2 He implantation Efforts

He implantation was also performed in order to investigate the impact of AIFs on swelling and bubble precipitation. In order for the bubbles to coalesce, implantation or a post implantation annealing must be performed using at least 30% the melting temperature. He implantations were performed at Los Alamos National Laboratory at 300 °C (the maximum temperature possible) in order to reach the bubble coalescence regime and match prior work [206]. In accordance with the conclusions from Chapter 5, 300 °C coupled with irradiation is likely sufficient to allow crystallization of AIFs, making the implantation results inconclusive for this thesis. Implantation at room temperature and subsequent annealing at AIF transition temperatures, or different alloy

systems where 300 °C is within the AIF transition range (with possible alloys described in greater detail in Chapter 7 and Appendix D) are possible pathways to consider for this research.

Appendix D: Motivation for Sn-Ag AIF investigation

Sn doped with Ag has a positive ΔH^{seg} [39] and a negative ΔH^{mix} [269], making this alloy a possible AIF-former in accordance with Chapter 2. Additionally, this alloy has a low melting point, where Sn-4 at.% Ag eutectic melts at 221 °C [269]. This makes Sn-Ag a viable candidate for AIF inspection, where temperatures as low as 155 °C (70% the eutectic melting temperature) may have AIF transitions. A lower melting temperature makes heated radiation and mechanical tests more accessible compared to Cu and Ni based alloys that have melting points almost 5 times greater, since many experimental configurations simply cannot sustain the operation temperatures necessary for AIF transitions in alloys with such high melting points. Tests can be performed in the temperature range where AIFs are the thermodynamically preferred state, and not simply metastable at room temperature. This makes new testing and inspection of AIFs feasible in order to more fully investigate their behavior, and approximates how AIFs could perform in real extreme environments, such as very-high temperature Gen IV nuclear reactors.

Sn-Ag (or related Sn-rich solders such as Sn-Pb) near the eutectic composition is an industry standard solder alloy for microchips [260], meaning there is an extensive history of research regarding this alloy in which to insert grain boundary AIF studies. Sn-Ag plating baths can easily be purchased (ex. Dupont Solderon™ BP TS 6000 Tin-Silver Plating Chemistry), or purchased as wires at any electronics store and subjected to mechanical processes such as equal channel angular pressing for grain refinement. Microchips manufactured with Sn-rich solder are subjected to a reflow process where the solder is melted in order to create the final solder bump shape and microstructure. If AIFs indeed form in Sn-Ag, then every microchip ever manufactured containing Sn-Ag solder (or related Sn-based alloys) may be subject to their effects. Yield losses, malformed solder bumps, anomalous failure modes, and premature solder failure may all have

roots in AIFs formed within the solder bump during high temperature excursions. For example, an overheating computer could push chip temperatures into the Sn-Ag AIF-forming regime, forming fast diffusion pathways within the solder bumps and ultimately causing premature electromigration failures due accelerated vacancy diffusion. In fact, in the extensive literature concerning Sn-Ag, there is already evidence that this alloy can form AIFs. Premelting was observed 10.6 °C below the melting point of pure Sn (or at ~95% of the melting point) during reflow at the interface of Sn and Ag multilayers [270]. Due to the metastable nature of AIFs at room temperature, the fact that AIFs do not form at every grain boundary, and that high resolution TEM is required to observe their presence, AIFs could indeed be playing an unknown, unexpected role in the chip industry, correlating to potentially millions of dollars of yield loss and premature failures.

If AIFs form in Sn-Ag (or related Sn-rich alloys), the extensive history of solder electrical research could also contribute to AIF research. Electrical resistivity is known to increase with decreasing grain size [271]. AIFs may further increase electrical resistivity due to the amorphous structuring of the grain boundary that may increase electron scattering [272, 273]. Four point probe measurements during Sn-Ag heating could be used to isolate jumps in resistance due to AIF formation across transition temperatures. Very fine control in resistance measurements and temperature would be necessary to permit these experiments. For example, a 5 °C temperature variation corresponds to almost 3% of the eutectic melting point. Fortunately concurrent electrical measurement during heating, with in situ SEM inspection under vacuum is possible using the Kleindiek system with the micro-heating stage (maximum 450 °C). UCI has a Kleindiek PS8 system compatible with the FEI Magellan SEM through the CaSTL center.

AIFs are a naturally occurring grain boundary entities that will form if the thermodynamic conditions are right. This thesis discovered in Chapter 2 that AIFs could possibly form in a wide range of alloys, many of which are already commonly used in industry. Additionally, many industrial processes already use high temperature treatments to achieve desired metallurgical states, such as casting, forging, and reflowing. The complexion perspective proved fruitful in formalizing components of AIF theory, but complexions are not part of metallurgical vernacular. Focusing on industry standard alloys, and using keywords such as "premelt" instead of "AIF" may open new doors in which to investigate these unique features.

References

[1] T. Watanabe, Grain boundary engineering: historical perspective and future prospects, J. Mater. Sci. 46(12) (2011) 4095.
[2] K.S. Kumar, H. Van Swygenhoven, S. Suresh, Mechanical behavior of nanocrystalline metals and alloys: the golden jubilee issue—selected topics in materials science and engineering: past, present and future, edited by S. Suresh, Acta Mater. 51(19) (2003) 5743.
[3] Y.S. Zhang, Z. Han, K. Wang, K. Lu, Friction and wear behaviors of nanocrystalline surface layer of pure copper, Wear 260(9) (2006) 942.
[4] T.M. Pollock, A.S. Argon, Creep resistance of CMSX-3 nickel base superalloy single crystals, Acta Metall. et Mater. 40(1) (1992) 1.
[5] G. Palumbo, S.J. Thorpe, K.T. Aust, On the contribution of triple junctions to the structure and properties of nanocrystalline materials, Scripta Metall. et Mater. 24(7) (1990) 1347.
[6] M.A. Meyers, A. Mishra, D.J. Benson, Mechanical properties of nanocrystalline materials, Prog. Mater Sci. 51(4) (2006) 427.
[7] M. Legros, B.R. Elliott, M.N. Rittner, J.R. Weertman, K.J. Hemker, Microsample tensile testing of nanocrystalline metals, Philos. Mag. A 80(4) (2000) 1017.
[8] Y.M. Wang, K. Wang, D. Pan, K. Lu, K.J. Hemker, E. Ma, Microsample tensile testing of nanocrystalline copper, Scripta Mater. 48(12) (2003) 1581.
[9] E.O. Hall, The deformation and ageing of mild steel: III, discussion of results, Proc. Phys. Soc. B 64(9) (1951) 747.
[10] T.J. Rupert, W. Cai, C.A. Schuh, Abrasive wear response of nanocrystalline Ni–W alloys across the Hall–Petch breakdown, Wear 298 (2013) 120.
[11] H.A. Padilla II, B.L. Boyce, C.C. Battaile, S.V. Prasad, Frictional performance and near-surface evolution of nanocrystalline Ni–Fe as governed by contact stress and sliding velocity, Wear 297(1-2) (2013) 860.
[12] T.J. Rupert, C.A. Schuh, Sliding wear of nanocrystalline Ni–W: structural evolution and the apparent breakdown of Archard scaling, Acta Mater. 58(12) (2010) 4137.
[13] B.L. Boyce, H.A. Padilla, Anomalous fatigue behavior and fatigue-induced grain growth in nanocrystalline nickel alloys, Metall. Mater. Trans. A 42(7) (2011) 1793.
[14] A.P. Sutton, R.W. Balluffi, Overview no. 61 on geometric criteria for low interfacial energy, Acta Metall. 35(9) (1987) 2177.
[15] A.P. Sutton, R.W. Balluffi, Interfaces in crystalline materials, Oxford University Press, New York, 1995.
[16] S.J. Dillon, G.S. Rohrer, Characterization of the grain-boundary character and energy distributions of yttria using automated serial sectioning and EBSD in the FIB, J. Am. Ceram. Soc. 92(7) (2009) 1580.
[17] D.G. Brandon, Structure of high-angle grain boundaries, Acta Metall. 14(11) (1966) 1479.
[18] G. Palumbo, K.T. Aust, E.M. Lehockey, U. Erb, P. Lin, On a more restrictive geometric criterion for "special" CSL grain boundaries, Scripta Mater. 38(11) (1998) 1685.
[19] J. Weissmüller, Alloy effects in nanostructures, Nanostructured Materials 3(1-6) (1993) 261.
[20] T. Chookajorn, H.A. Murdoch, C.A. Schuh, Design of stable nanocrystalline alloys, Science 337 (2012) 951.
[21] M. Ames, J. Markmann, R. Karos, A. Michels, A. Tschope, R. Birringer, Unraveling the nature of room temperature grain growth in nanocrystalline materials, Acta Mater. 56 (2008) 4255.

[22] Q. Wei, T. Jiao, S.N. Mathaudhu, E. Ma, K.T. Hartwig, K.T. Ramesh, Microstructure and mechanical properties of tantalum after equal channel angular extrusion (ECAE), Mater. Sci. Eng., A 358 (2003) 266.
[23] J.M. Dake, C.E. Krill, Sudden loss of thermal stability in Fe-based nanocrystalline alloys, Scripta Mater. 66 (2012) 390.
[24] G. Hibbard, K.T. Aust, G. Palumbo, U. Erb, Thermal stability of electrodeposited nanocrystalline cobalt, Scripta Mater. 44 (2001) 513.
[25] G. Hibbard, J. McCrea, G. Palumbo, K. Aust, U. Erb, An initial analysis of mechanisms leading to late stage abnormal grain growth in nanocrystalline Ni, Scripta Mater. 47(2) (2002) 83.
[26] V.Y. Gertsman, R. Birringer, On the room temperature grain growth in nanocrystalline copper, Scripta Metall. et Mater. 30 (1994) 577.
[27] Z. Morlin, J. Tremmel, An emission electronmicroscopy study on the heat treatment induced grain growth of molybdenum and tantalum, Journal de Microscopie 5(4) (1966).
[28] B.B. Straumal, W. Gust, V.G. Sursaeva, V.N. Semenov, L.S. Shvindlerman, Normal and abnormal grain growth in tungsten polycrystals, Mater. Sci. Forum 294-296 (1999) 533.
[29] J.E. Burke, D. Turnbull, Recrystallization and grain growth, Prog. Metal Phys. 3(C) (1952) 220.
[30] J.W. Cahn, The impurity-drag effect in grain boundary motion, Acta Metall. 10(9) (1962) 789.
[31] C.C. Koch, R.O. Scattergood, M. Saber, H. Kotan, High temperature stabilization of nanocrystalline grain size: thermodynamic versus kinetic strategies, J. Mater. Res. 28(13) (2013) 1785.
[32] K. Boylan, D. Ostrander, U. Erb, G. Palumbo, K.T. Aust, An in-situ tem study of the thermal stability of nanocrystalline NiP, Scripta Metall. et Mater. 25(12) (1991) 2711.
[33] Z. Chen, F. Liu, X.Q. Yang, C.J. Shen, Y.M. Zhao, A thermokinetic description of nano-scale grain growth under dynamic grain boundary segregation condition, J. Alloys Compd. 608(C) (2014) 338.
[34] E. Nes, N. Ryum, O. Hunderi, On the Zener drag, Acta Metall. 33(1) (1985) 11.
[35] K.A. Darling, A.J. Roberts, Y. Mishin, S.N. Mathaudhu, L.J. Kecskes, Grain size stabilization of nanocrystalline copper at high temperatures by alloying with tantalum, J. Alloys Compd. 573 (2013) 142.
[36] C.C. Koch, R.O. Scattergood, K.A. Darling, J.E. Semones, Stabilization of nanocrystalline grain sizes by solute additions, J. Mater. Sci. 43(23-24) (2008) 7264.
[37] A.R. Kalidindi, T. Chookajorn, C.A. Schuh, Nanocrystalline materials at equilibrium: a thermodynamic review, JOM 67(12) (2015) 2834.
[38] T.J. Rupert, The role of complexions in metallic nano-grain stability and deformation, Curr. Opin. Solid State Mater. Sci. 20(5) (2016) 257.
[39] H.A. Murdoch, C.A. Schuh, Estimation of grain boundary segregation enthalpy and its role in stable nanocrystalline alloy design, J. Mater. Res. 28(16) (2013) 2154.
[40] H.A. Murdoch, C.A. Schuh, Stability of binary nanocrystalline alloys against grain growth and phase separation, Acta Mater. 61(6) (2013) 2121.
[41] T. Chookajorn, C.A. Schuh, Thermodynamics of stable nanocrystalline alloys: a monte carlo analysis, Phys. Rev. B 89(6) (2014) 064102.
[42] A.R. Kalidindi, C.A. Schuh, Stability criteria for nanocrystalline alloys, Acta Mater. 132 (2017) 128.

[43] K.A. Darling, M.A. Tschopp, B.K. VanLeeuwen, M.A. Atwater, Z.K. Liu, Mitigating grain growth in binary nanocrystalline alloys through solute selection based on thermodynamic stability maps, Comput. Mater. Sci. 84 (2014) 255.
[44] B. Faber, E. Cadel, A. Menand, G. Schmitz, R. Kirchheim, Phosphorus segregation in nanocrystalline Ni-3.6at%P alloy investigated with the tomographic atom probe (TAP), Acta Mater. 48 (2000).
[45] B.G. Clark, K. Hattar, M.T. Marshall, T. Chookajorn, B.L. Boyce, C.A. Schuh, Thermal stability comparison of nanocrystalline Fe-based binary alloy pairs, JOM 68(6) (2016) 1625.
[46] H. Sun, C. Deng, Direct quantification of solute effects on grain boundary motion by atomistic simulations, Comput. Mater. Sci. 93 (2014) 137.
[47] T. Frolov, K.A. Darling, L.J. Kecskes, Y. Mishin, Stabilization and strengthening of nanocrystalline copper by alloying with tantalum, Acta Mater. 60(5) (2012) 2158.
[48] E. Botcharova, J. Freudenberger, L. Schultz, Mechanical and electrical properties of mechanically alloyed nanocrystalline Cu–Nb alloys, Acta Mater. 54(12) (2006) 3333.
[49] J.R. Trelewicz, C.A. Schuh, Grain boundary segregation and thermodynamically stable binary nanocrystalline alloys, Phys. Rev. B 79 (2009).
[50] A.J. Detor, C.A. Schuh, Microstructural evolution during the heat treatment of nanocrystalline alloys, J. Mater. Res. 22(11) (2007) 3233.
[51] K.A. Darling, B.K. VanLeeuwen, C.C. Koch, R.O. Scattergood, Thermal stability of nanocrystalline Fe–Zr alloys, Mater. Sci. Eng., A 527(15) (2010) 3572.
[52] F. Abdeljawad, P. Lu, N. Argibay, B.G. Clark, B.L. Boyce, S.M. Foiles, Grain boundary segregation in immiscible nanocrystalline alloys, Acta Mater. 126 (2017) 528.
[53] C.J. O'Brien, C.M. Barr, P.M. Price, K. Hattar, S.M. Foiles, Grain boundary phase transformations in PtAu and relevance to thermal stabilization of bulk nanocrystalline metals, J. Mater. Sci. 53(4) (2018) 2911.
[54] Z. Pan, T.J. Rupert, Effect of grain boundary character on segregation-induced structural transitions, Phys. Rev. B 93(13) (2016) 134113.
[55] N.M. Heckman, S.M. Foiles, C.J. O'Brien, M. Chandross, C.M. Barr, N. Argibay, K. Hattar, P. Lu, D.P. Adams, B.L. Boyce, New nanoscale toughening mechanisms mitigate embrittlement in binary nanocrystalline alloys, Nanoscale 10(45) (2018) 21231.
[56] S.J. Dillon, M. Tang, W.C. Carter, M.P. Harmer, Complexion: a new concept for kinetic engineering in materials science, Acta Mater. 55(18) (2007) 6208.
[57] X. Shi, J. Luo, Developing grain boundary diagrams as a materials science tool: a case study of nickel-doped molybdenum, Phys. Rev. B 84(1) (2011).
[58] S.J. Dillon, M.P. Harmer, J. Luo, Grain boundary complexions in ceramics and metals: an overview, JOM 61(12) (2009) 38.
[59] P.R. Cantwell, M. Tang, S.J. Dillon, J. Luo, G.S. Rohrer, M.P. Harmer, Grain boundary complexions, Acta Mater. 62 (2014) 1.
[60] M. Tang, W.C. Carter, R.M. Cannon, Grain boundary order-disorder transitions, J. Mater. Sci. 41(23) (2006) 7691.
[61] T. Frolov, D.L. Olmsted, M. Asta, Y. Mishin, Structural phase transformations in metallic grain boundaries, Nat. Comm. 4 (2013) 1899.
[62] J. Luo, Liquid-like interface complexion: From activated sintering to grain boundary diagrams, Curr. Opin. Solid State Mater. Sci. 12(5) (2008) 81.
[63] A. Kundu, K.M. Asl, J. Luo, M.P. Harmer, Identification of a bilayer grain boundary complexion in Bi-doped Cu, Scripta Mater. 68(2) (2013) 146.

[64] J. Luo, H. Cheng, K.M. Asl, C.J. Kiely, M.P. Harmer, The role of a bilayer interfacial phase on liquid metal embrittlement, Science 333(6050) (2011) 1730.
[65] W. Sigle, G. Richter, M. Rühle, S. Schmidt, Insight into the atomic-scale mechanism of liquid metal embrittlement, Appl. Phys. Lett. 89(12) (2006) 121911.
[66] A. Khalajhedayati, Z. Pan, T.J. Rupert, Manipulating the interfacial structure of nanomaterials to achieve a unique combination of strength and ductility, Nat. Comm. 7 (2016) 10802.
[67] T.E. Hsieh, R.W. Balluffi, Experimental study of grain boundary melting in aluminum, Acta Metall. 37(6) (1989) 1637.
[68] Z. Pan, T.J. Rupert, Amorphous intergranular films as toughening structural features, Acta Mater. 89 (2015) 205.
[69] Z. Pan, T.J. Rupert, Damage nucleation from repeated dislocation absorption at a grain boundary, Comput. Mater. Sci. 93 (2014) 206.
[70] C. Brandl, T.C. Germann, A. Misra, Structure and shear deformation of metallic crystalline–amorphous interfaces, Acta Mater. 61(10) (2013) 3600.
[71] J.E. Ludy, T.J. Rupert, Amorphous intergranular films act as ultra-efficient point defect sinks during collision cascades, Scripta Mater. 110 (2016) 37.
[72] V. Turlo, T.J. Rupert, Grain boundary complexions and the strength of nanocrystalline metals: dislocation emission and propagation, Acta Mater. 151 (2018) 100.
[73] Y. Wang, J. Li, A.V. Hamza, T.W. Barbee Jr., Ductile crystalline-amorphous nanolaminates, Proced. Nat. Acad. of Sci. 104(27) (2007) 11155.
[74] A. Khalajhedayati, T.J. Rupert, High-Temperature Stability and Grain Boundary Complexion Formation in a Nanocrystalline Cu-Zr Alloy, JOM 67(12) (2015) 2788.
[75] J.D. Schuler, T.J. Rupert, Materials selection rules for amorphous complexion formation in binary metallic alloys, Acta Mater. 140 (2017) 196.
[76] M. Faraday, Note on regelation, Proc. R. Soc. London 10 (1859) 440.
[77] E.W. Hart, Two-dimensional phase transformation in grain boundaries, Scripta Metall. 2(3) (1968) 179.
[78] J.W. Cahn, Transitions and phase equilibria among grain boundary structures, Le Journal de Physique Colloques 43(C6) (1982) C6.
[79] A.P. Sutton, R.W. Balluffi, H. Lüth, J.M. Gibson, Interfaces in crystalline materials and surfaces and interfaces of solid materials, Physics Today 49 (1996) 88.
[80] S.J. Dillon, M.P. Harmer, Multiple grain boundary transitions in ceramics: a case study of alumina, Acta Mater. 55(15) (2007) 5247.
[81] S. Divinski, M. Lohmann, C. Herzig, B. Straumal, B. Baretzky, W. Gust, Grain-boundary melting phase transition in the Cu− Bi system, Phys. Rev. B 71(10) (2005) 104104.
[82] M. Tang, W.C. Carter, R.M. Cannon, Grain boundary transitions in binary alloys, Phys. Rev. Lett. 97(7) (2006) 075502.
[83] D.R. Clarke, On the detection of thin intergranular films by electron microscopy, Ultramicroscopy 4(1) (1979) 33.
[84] J. Luo, X. Shi, Grain boundary disordering in binary alloys, Appl. Phys. Lett. 92(10) (2008) 101901.
[85] W.H. Zachariasen, The atomic arrangement in glass, JACS 54(10) (1932) 3841.
[86] A.R. Cooper, W.H. Zachariasen - the melody lingers on, J. Non-Cryst. Solids 49(1) (1982) 1.
[87] A. Inoue, Stabilization of metallic supercooled liquid and bulk amorphous alloys, Acta Mater. 48(1) (2000) 279.

[88] A. Ziegler, J.C. Idrobo, M.K. Cinibulk, C. Kisielowski, N.D. Browning, R.O. Ritchie, Interface structure and atomic bonding characteristics in silicon nitride ceramics, Science 306(5702) (2004) 1768.
[89] M.K. Cinibulk, H.J. Kleebe, Effects of oxidation on intergranular phases in silicon nitride ceramics, J. Mater. Sci. 28(21) (1993) 5775.
[90] D.B. Williams, C.B. Carter, Transmission electron microscopy: a textbook for materials science, Springer, New York, 1996.
[91] C. Koch, I. Ovid'ko, S. Seal, S. Veprek, Structural nanocrystalline materials: fundamentals and applications Cambridge University Press, New York, 2007.
[92] J.A. Thornton, Influence of substrate temperature and deposition rate on structure of thick sputtered Cu coatings, J. Vacuum Sci. Tech. 12(4) (1975) 830.
[93] C.V. Thompson, Structure evolution during processing of polycrystalline films, Annu. Rev. Mater. Sci. 30(1) (2000) 159.
[94] Q. Jin, D.S. Wilkinson, G.C. Weatherly, Determination of grain-boundary film thickness by the fresnel fringe imaging technique, J. Eur. Ceram. Soc. 18(15) (1998) 2281.
[95] C.W. Corti, Sintering aids in powder metallurgy, Platinum Met. Rev. 30(4) (1986) 184.
[96] Z. Pan, T.J. Rupert, Spatial variation of short-range order in amorphous intergranular complexions, Comput. Mater. Sci. 131 (2017) 62.
[97] W.H. Wang, C. Dong, C.H. Shek, Bulk metallic glasses, Mater. Sci. Eng., R 44(2-3) (2004) 45.
[98] D. Wang, Y. Li, B.B. Sun, M.L. Sui, K. Lu, E. Ma, Bulk metallic glass formation in the binary Cu–Zr system, Appl. Phys. Lett. 84(20) (2004) 4029.
[99] W. Xing, A.R. Kalidindi, C.A. Schuh, Preferred nanocrystalline configurations in ternary and multicomponent alloys, Scripta Mater. 127 (2017) 136.
[100] N.N. Greenwood, A. Earnshaw, Chemistry of the elements, 2nd ed., Butterworth-Heinemann, Oxford, 1997.
[101] K. Zhang, B. Dice, Y. Liu, J. Schroers, M.D. Shattuck, C.S. O'Hern, On the origin of multi-component bulk metallic glasses: atomic size mismatches and de-mixing, J. Chem. Phys. 143(5) (2015) 054501.
[102] D.A. Porter, K.E. Easterling, M. Sherif, Phase transformations in metals and alloys, CRC press, New York, 2009.
[103] M. Kapoor, T. Kaub, K.A. Darling, B.L. Boyce, G.B. Thompson, An atom probe study on Nb solute partitioning and nanocrystalline grain stabilization in mechanically alloyed Cu-Nb, Acta Mater. 126 (2017) 564.
[104] Z. Pan, T.J. Rupert, Formation of ordered and disordered interfacial films in immiscible metal alloys, Scripta Mater. 130 (2017) 91.
[105] N.Q. Vo, J. Schäfer, R.S. Averback, K. Albe, Y. Ashkenazy, P. Bellon, Reaching theoretical strengths in nanocrystalline Cu by grain boundary doping, Scripta Mater. 65(8) (2011) 660.
[106] N.Q. Vo, S.W. Chee, D. Schwen, X. Zhang, P. Bellon, R.S. Averback, Microstructural stability of nanostructured Cu alloys during high-temperature irradiation, Scripta Mater. 63(9) (2010) 929.
[107] M.A. Atwater, K.A. Darling, A visual library of stability in binary metallic systems: the stabilization of nanocrystalline grain size by solute addition: part 1, Army Research Lab Aberdeen Proving Ground MD Weapons and Materials Research Directorate, 2012.
[108] O.J. Kleppa, S. Watanabe, Thermochemistry of alloys of transition metals: part III. copper-silver,-titanium,-zirconium, and-hafnium at 1373 K, J. Electron. Mater. 20(12) (1991) 391.

[109] L. Zhang, E. Martinez, A. Caro, X.Y. Liu, M.J. Demkowicz, Liquid-phase thermodynamics and structures in the Cu–Nb binary system, Modell. Simul. Mater. Sci. Eng. 21(2) (2013) 025005.
[110] C.J. Smithells, W.F. Gale, T.C. Totemeier, Smithells metals reference book, 8th ed., Elsevier Butterworth-Heinemann, Boston, 2004.
[111] D.H. Kang, H. Zhang, H. Yoo, H.H. Lee, S. Lee, G.W. Lee, H. Lou, X. Wang, Q. Cao, D. Zhang, J. Jiang, Interfacial free energy controlling glass-forming ability of Cu-Zr alloys, Sci. Rep. 4 (2014) 5167.
[112] A. Inoue, W. Zhang, Formation, thermal stability and mechanical properties of Cu-Zr and Cu-Hf binary glassy alloy rods, Mater. Trans. 45(2) (2004) 584.
[113] M. Klinger, A. Jager, Crystallographic Tool Box (CrysTBox): automated tools for transmission electron microscopists and crystallographers, J. Appl. Crystallogr. 48(Pt 6) (2015) 2012.
[114] C. Gammer, C. Mangler, C. Rentenberger, H.P. Karnthaler, Quantitative local profile analysis of nanomaterials by electron diffraction, Scripta Mater. 63(3) (2010) 312.
[115] Z. Pan, T.J. Rupert, Effect of grain boundary character on segregation-induced structural transitions, Physical Review B 93(13) (2016) 134113.
[116] M.N. Polyakov, T. Chookajorn, M. Mecklenburg, C.A. Schuh, A.M. Hodge, Sputtered Hf–Ti nanostructures: a segregation and high-temperature stability study, Acta Mater. 108 (2016) 8.
[117] T. Frolov, Y. Mishin, Stable nanocolloidal structures in metallic systems, Phys. Rev. Lett. 104(5) (2010) 055701.
[118] T. Gladman, On the theory of the effect of precipitate particles on grain growth in metals, Proc. R. Soc. London, Ser. A 294(1438) (1966) 298.
[119] Y.D. Dong, G. Gregan, M.G. Scott, Formation and stability of nickel-zirconium glasses, J. Non-Cryst. Solids 43(3) (1981) 403.
[120] M. Rösner-Kuhn, J. Qin, K. Schaefers, U. Thiedemann, M.G. Frohberg, Temperature dependence of the mixing enthalpy and excess heat capacity in the liquid system nickel-zirconium, Int. J. Thermophys. 17(4) (1996) 959.
[121] G. Ghosh, C. Kantner, G.B. Olson, Thermodynamic modeling of the Pd-X (X=Ag, Co, Fe, Ni) systems, J. Phase Equilib. 20(3) (1999) 295.
[122] Y.M. Kim, Y.H. Shin, B.J. Lee, Modified embedded-atom method interatomic potentials for pure Mn and the Fe–Mn system, Acta Mater. 57(2) (2009) 474.
[123] O.J. Kleppa, L. Topor, Thermochemistry of binary liquid gold alloys: The systems (Au + Cr), (Au + V), (Au + Ti), and (Au + Sc) at 1379 K, Metall. Trans. A 16(1) (1985) 93.
[124] C.J. Lin, F. Spaepen, Nickel-niobium alloys obtained by picosecond pulsed laser quenching, Acta Metall. 34(7) (1986) 1367.
[125] F. Spaepen, Interdiffusion in amorphous metallic artificial multilayers, Mater. Sci. Eng. 97 (1988) 403.
[126] J.D. Schuler, O.K. Donaldson, T.J. Rupert, Amorphous complexions enable a new region of high temperature stability in nanocrystalline Ni-W, Scripta Mater. 154 (2018) 49.
[127] A.J. Detor, C.A. Schuh, Grain boundary segregation, chemical ordering and stability of nanocrystalline alloys: atomistic computer simulations in the Ni–W system, Acta Mater. 55(12) (2007) 4221.
[128] A.J. Detor, C.A. Schuh, Tailoring and patterning the grain size of nanocrystalline alloys, Acta Mater. 55(1) (2007) 371.

[129] P. Franke, D. Neuschütz, Ni-W, Binary systems part 4: binary systems from Mn-Mo to Y-Zr: phase diagrams, phase transition data, Integral and partial quantities of alloys, Springer, Berlin, Heidelberg, 2006.
[130] K.A. Darling, B.K. VanLeeuwen, J.E. Semones, C.C. Koch, R.O. Scattergood, L.J. Kecskes, S.N. Mathaudhu, Stabilized nanocrystalline iron-based alloys: guiding efforts in alloy selection, Mater. Sci. Eng., A 528 (2011) 4365.
[131] F. Abdeljawad, S.M. Foiles, Stabilization of nanocrystalline alloys via grain boundary segregation: a diffuse interface model, Acta Mater. 101 (2015) 159.
[132] A. Hu, The nature and behavior of grain boundaries: a symposium held at the TMS-AIME fall meeting in Detroit, Michigan, October 18–19, 1971, Springer Science & Business Media, 2012.
[133] V.K. Gupta, D.H. Yoon, H.M. Meyer, J. Luo, Thin intergranular films and solid-state activated sintering in nickel-doped tungsten, Acta Mater. 55(9) (2007) 3131.
[134] X. Shi, J. Luo, Grain boundary wetting and prewetting in Ni-doped Mo, Appl. Phys. Lett. 94(25) (2009) 251908.
[135] J. Luo, V.K. Gupta, D.H. Yoon, H.M. Meyer III, Segregation-induced grain boundary premelting in nickel-doped tungsten, Appl. Phys. Lett. 87(23) (2005) 231902.
[136] J.D. Schuler, C.M. Barr, N.M. Heckman, G. Copeland, B.L. Boyce, K. Hattar, T.J. Rupert, In situ high-cycle fatigue reveals importance of grain boundary structure in nanocrystalline Cu-Zr, JOM 71(4) (2019) 1221.
[137] K.M. Youssef, R.O. Scattergood, K.L. Murty, J.A. Horton, C.C. Koch, Ultrahigh strength and high ductility of bulk nanocrystalline copper, Appl. Phys. Lett. 87(9) (2005) 091904.
[138] C.C. Koch, K.M. Youssef, R.O. Scattergood, K.L. Murty, Breakthroughs in optimization of mechanical properties of nanostructured metals and alloys, Adv. Eng. Mater. 7(9) (2005) 787.
[139] R.O. Ritchie, Mechanisms of fatigue-crack propagation in ductile and brittle solids, Int. J. Fracture 100(1) (1999) 55.
[140] T. Hanlon, E.D. Tabachnikova, S. Suresh, Fatigue behavior of nanocrystalline metals and alloys, Int. J. Fatigue 27(10) (2005) 1147.
[141] T. Hanlon, Y.N. Kwon, S. Suresh, Grain size effects on the fatigue response of nanocrystalline metals, Scripta Mater. 49(7) (2003) 675.
[142] T.A. Furnish, D.C. Bufford, F. Ren, A. Mehta, K. Hattar, B.L. Boyce, Evidence that abnormal grain growth precedes fatigue crack initiation in nanocrystalline Ni-Fe, Scripta Mater. 143 (2018) 15.
[143] T.A. Furnish, A. Mehta, D. Van Campen, D.C. Bufford, K. Hattar, B.L. Boyce, The onset and evolution of fatigue-induced abnormal grain growth in nanocrystalline Ni–Fe, J. Mater. Sci. 52(1) (2017) 46.
[144] R.A. Meirom, D.H. Alsem, A.L. Romasco, T. Clark, R.G. Polcawich, J.S. Pulskamp, M. Dubey, R.O. Ritchie, C.L. Muhlstein, Fatigue-induced grain coarsening in nanocrystalline platinum films, Acta Mater. 59(3) (2011) 1141.
[145] M.D. Sangid, The physics of fatigue crack initiation, Int. J. Fatigue 57 (2013) 58.
[146] H.A. Padilla II, B.L. Boyce, A review of fatigue behavior in nanocrystalline metals, Exp. Mech. 50(1) (2010) 5.
[147] F. Mompiou, M. Legros, A. Boé, M. Coulombier, J.P. Raskin, T. Pardoen, Inter- and intragranular plasticity mechanisms in ultrafine-grained Al thin films: an in situ TEM study, Acta Mater. 61(1) (2013) 205.

[148] K.S. Kumar, S. Suresh, M.F. Chisholm, J.A. Horton, P. Wang, Deformation of electrodeposited nanocrystalline nickel, Acta Mater. 51(2) (2003) 387.
[149] D.S. Gianola, B.G. Mendis, X.M. Cheng, K.J. Hemker, Grain-size stabilization by impurities and effect on stress-coupled grain growth in nanocrystalline Al thin films, Mater. Sci. Eng., A 483 (2008) 637.
[150] L. Wang, T. Xin, D. Kong, X. Shu, Y. Chen, H. Zhou, J. Teng, Z. Zhang, J. Zou, X.D. Han, In situ observation of stress induced grain boundary migration in nanocrystalline gold, Scripta Mater. 134 (2017) 95.
[151] Z.X. Wu, Y.W. Zhang, M.H. Jhon, D.J. Srolovitz, Anatomy of nanomaterial deformation: Grain boundary sliding, plasticity and cavitation in nanocrystalline Ni, Acta Mater. 61(15) (2013) 5807.
[152] P. Liu, S.C. Mao, L.H. Wang, X.D. Han, Z. Zhang, Direct dynamic atomic mechanisms of strain-induced grain rotation in nanocrystalline, textured, columnar-structured thin gold films, Scripta Mater. 64(4) (2011) 343.
[153] L.F. Allard, W.C. Bigelow, M. Jose Yacaman, D.P. Nackashi, J. Damiano, S.E. Mick, A new MEMS-based system for ultra-high-resolution imaging at elevated temperatures, Microsc. Res. Tech. 72(3) (2009) 208.
[154] L. Zhong, J. Wang, H. Sheng, Z. Zhang, S.X. Mao, Formation of monatomic metallic glasses through ultrafast liquid quenching, Nature 512(7513) (2014) 177.
[155] D.C. Bufford, D. Stauffer, W.M. Mook, S.A. Syed Asif, B.L. Boyce, K. Hattar, High cycle fatigue in the transmission electron microscope, Nano Lett. 16(8) (2016) 4946.
[156] X.K. Zhu, Progress in development of fracture toughness test methods for SENT specimens, Int. J. Press. Vessels and Piping 156 (2017) 40.
[157] V. Samaeeaghmiyoni, H. Idrissi, J. Groten, R. Schwaiger, D. Schryvers, Quantitative in-situ TEM nanotensile testing of single crystal Ni facilitated by a new sample preparation approach, Micron 94 (2017) 66.
[158] K. Hattar, D.C. Bufford, D.L. Buller, Concurrent in situ ion irradiation transmission electron microscope, Nucl. Instrum. Methods Phys. Res., Sect. B 338 (2014) 56.
[159] S.K. Lin, Y.L. Lee, M.W. Lu, Evaluation of the staircase and the accelerated test methods for fatigue limit distributions, Int. J. Fatigue 23(1) (2001) 75.
[160] R.C. Hugo, H. Kung, J.R. Weertman, R. Mitra, J.A. Knapp, D.M. Follstaedt, In-situ TEM tensile testing of DC magnetron sputtered and pulsed laser deposited Ni thin films, Acta Mater. 51(7) (2003) 1937.
[161] C.M. Park, J.A. Bain, Focused-ion-beam induced grain growth in magnetic materials for recording heads, J. Appl. Phys. 91(10) (2002) 6830.
[162] C.V. Thompson, Grain growth in thin films, Annu. Rev. Mater. Sci. 20(1) (1990) 245.
[163] Y. Yang, B. Imasogie, G.J. Fan, P.K. Liaw, W.O. Soboyejo, Fatigue and fracture of a bulk nanocrystalline NiFe alloy, Metall. Mater. Trans. A 39(5) (2008) 1145.
[164] D. Farkas, M. Willemann, B. Hyde, Atomistic mechanisms of fatigue in nanocrystalline metals, Phys. Rev. Lett. 94(16) (2005) 165502.
[165] R.O. Ritchie, Mechanisms of fatigue crack propagation in metals, ceramics and composites: role of crack tip shielding, Mater. Sci. Eng., A 103(1) (1988) 15.
[166] J.K. Shang, R.O. Ritchie, Crack bridging by uncracked ligaments during fatigue-crack growth in SiC-reinforced aluminum-alloy composites, Metall. Trans. A 20(5) (1989) 897.
[167] R. Ramachandramoorthy, R. Bernal, H.D. Espinosa, Pushing the envelope of in situ transmission electron microscopy, ACS Nano 9(5) (2015) 4675.

[168] Z. Liu, D. Yu, J. Tang, X. Chen, X. Wang, Stress intensity factor and T-stress solutions for three-dimensional clamped single edge notched tension (SENT) specimens, Int. J. Press. Vessels and Piping 168 (2018) 11.
[169] M.D. Thouless, Bridging and damage zones in crack growth, J. Am. Ceram. Soc. 71(6) (1988) 408.
[170] A. Vinogradov, Fatigue limit and crack growth in ultra-fine grain metals produced by severe plastic deformation, J. Mater. Sci. 42(5) (2007) 1797.
[171] R. Pippan, A. Hohenwarter, Fatigue crack closure: a review of the physical phenomena, Fatigue Fract. Eng. Mater. Struct. 40(4) (2017) 471.
[172] C. Laird, G.C. Smith, Crack propagation in high stress fatigue, Philos. Mag. 7(77) (1962) 847.
[173] J. Xie, X. Wu, Y. Hong, Shear bands at the fatigue crack tip of nanocrystalline nickel, Scripta Mater. 57(1) (2007) 5.
[174] K. Tanaka, Y. Nakai, M. Yamashita, Fatigue growth threshold of small cracks, Int. J. Fracture 17(5) (1981) 519.
[175] C. Bjerkén, S. Melin, A study of the influence of grain boundaries on short crack growth during varying load using a dislocation technique, Eng. Fracture Mech. 71(15) (2004) 2215.
[176] M.Y. Gutkin, I.A. Ovid'ko, Nanocracks at grain boundaries in nanocrystalline materials, Philos. Mag. Lett. 84(10) (2004) 655.
[177] S. Suresh, Crack deflection: implications for the growth of long and short fatigue cracks, Metall. Trans. A 14(11) (1983) 2375.
[178] A.M. Gokhale, W.J. Drury, S. Mishra, Recent developments in quantitative fractography, Fractography of Modern Engineering Materials: Composites and Metals, ASTM, Philadelphia, 1993, pp. 3.
[179] D. Farkas, H. Van Swygenhoven, P.M. Derlet, Intergranular fracture in nanocrystalline metals, Phys. Rev. B: Condens. Matter 66(6) (2002) 060101.
[180] M.D. Sangid, G.J. Pataky, H. Sehitoglu, R.G. Rateick, T. Niendorf, H.J. Maier, Superior fatigue crack growth resistance, irreversibility, and fatigue crack growth–microstructure relationship of nanocrystalline alloys, Acta Mater. 59(19) (2011) 7340.
[181] Y. Zhang, G.J. Tucker, J.R. Trelewicz, Stress-assisted grain growth in nanocrystalline metals: grain boundary mediated mechanisms and stabilization through alloying, Acta Mater. 131 (2017) 39.
[182] R. Liu, Y. Tian, Z. Zhang, X. An, P. Zhang, Z. Zhang, Exceptional high fatigue strength in Cu-15at.%Al alloy with moderate grain size, Sci. Rep. 6 (2016) 27433.
[183] G.Q. Xu, M.J. Demkowicz, Healing of nanocracks by disclinations, Phys. Rev. Lett. 111(14) (2013) 145501.
[184] T. Leitner, A. Hohenwarter, R. Pippan, Revisiting fatigue crack growth in various grain size regimes of Ni, Mater. Sci. Eng., A 646 (2015) 294.
[185] T.R. Bieler, P. Eisenlohr, F. Roters, D. Kumar, D.E. Mason, M.A. Crimp, D. Raabe, The role of heterogeneous deformation on damage nucleation at grain boundaries in single phase metals, Int. J. Plast. 25(9) (2009) 1655.
[186] A. Singh, L. Tang, M. Dao, L. Lu, S. Suresh, Fracture toughness and fatigue crack growth characteristics of nanotwinned copper, Acta Mater. 59(6) (2011) 2437.
[187] L. Liu, J. Wang, S.K. Gong, S.X. Mao, Atomistic observation of a crack tip approaching coherent twin boundaries, Sci. Rep. 4 (2014) 4397.

[188] T. Abram, S. Ion, Generation-IV nuclear power: a review of the state of the science, Energy Policy 36(12) (2008) 4323.
[189] L.K. Mansur, A.F. Rowcliffe, R.K. Nanstad, S.J. Zinkle, W.R. Corwin, R.E. Stoller, Materials needs for fusion, Generation IV fission reactors and spallation neutron sources–similarities and differences, J. Nucl. Mater. 329 (2004) 166.
[190] S.J. Zinkle, G.S. Was, Materials challenges in nuclear energy, Acta Mater. 61(3) (2013) 735.
[191] K.L. Murty, I. Charit, Structural materials for Gen-IV nuclear reactors: challenges and opportunities, J. Nucl. Mater. 383(1-2) (2008) 189.
[192] R.W. Grimes, R.J.M. Konings, L. Edwards, Greater tolerance for nuclear materials, Nature Mat. 7 (2008) 683.
[193] E.E. Bloom, S.J. Zinkle, F.W. Wiffen, Materials to deliver the promise of fusion power–progress and challenges, J. Nucl. Mater. 329 (2004) 12.
[194] D. Chapin, S. Kiffer, J. Nestell, The very high temperature reactor: a technical summary, MPR Associates, Alexandria, VA (2004).
[195] G.S. Was, Fundamentals of radiation materials science: metals and alloys, Springer, 2016.
[196] L.K. Mansur, Void swelling in metals and alloys under irradiation: an assessment of the theory, Nucl. Technol. 40(1) (1978) 5.
[197] G.R. Odette, G.E. Lucas, Embrittlement of nuclear reactor pressure vessels, JOM 53(7) (2001) 18.
[198] P. Scott, A review of irradiation assisted stress corrosion cracking, J. Nucl. Mater. 211(2) (1994) 101.
[199] I.J. Beyerlein, A. Caro, M.J. Demkowicz, N.A. Mara, A. Misra, B.P. Uberuaga, Radiation damage tolerant nanomaterials, Mater. Today 16(11) (2013) 443.
[200] W. Han, M.J. Demkowicz, N.A. Mara, E. Fu, S. Sinha, A.D. Rollett, Y. Wang, J.S. Carpenter, I.J. Beyerlein, A. Misra, Design of radiation tolerant materials via interface engineering, Adv. Mater. 25(48) (2013) 6975.
[201] X. Zhang, E. Fu, A. Misra, M.J. Demkowicz, Interface-enabled defect reduction in He ion irradiated metallic multilayers, JOM 62(12) (2010) 75.
[202] A. Misra, M.J. Demkowicz, X. Zhang, R.G. Hoagland, The radiation damage tolerance of ultra-high strength nanolayered composites, JOM 59(9) (2007) 62.
[203] E.M. Bringa, J.D. Monk, A. Caro, A. Misra, L. Zepeda-Ruiz, M. Duchaineau, F. Abraham, M. Nastasi, S.T. Picraux, Y.Q. Wang, D. Farkas, Are nanoporous materials radiation resistant?, Nano Lett. 12(7) (2012) 3351.
[204] X.M. Bai, A.F. Voter, R.G. Hoagland, M. Nastasi, B.P. Uberuaga, Efficient annealing of radiation damage near grain boundaries via interstitial emission, Science 327(5973) (2010) 1631.
[205] N.V. Doan, G. Martin, Elimination of irradiation point defects in crystalline solids: sink strengths, Phys. Rev. B 67(13) (2003) 134107.
[206] W.Z. Han, M.J. Demkowicz, E.G. Fu, Y.Q. Wang, A. Misra, Effect of grain boundary character on sink efficiency, Acta Mater. 60(18) (2012) 6341.
[207] B.P. Uberuaga, L.J. Vernon, E. Martinez, A.F. Voter, The relationship between grain boundary structure, defect mobility, and grain boundary sink efficiency, Sci. Rep. 5 (2015) 9095.
[208] N. Nita, R. Schaeublin, M. Victoria, Impact of irradiation on the microstructure of nanocrystalline materials, J. Nucl. Mater. 329 (2004) 953.
[209] Y. Chimi, A. Iwase, N. Ishikawa, M. Kobiyama, T. Inami, S. Okuda, Accumulation and recovery of defects in ion-irradiated nanocrystalline gold, J. Nucl. Mater. 297(3) (2001) 355.

[210] M. Rose, A.G. Balogh, H. Hahn, Instability of irradiation induced defects in nanostructured materials, Nucl. Instrum. Methods Phys. Res., Sect. B 127 (1997) 119.
[211] C.M. Barr, N. Li, B.L. Boyce, K. Hattar, Examining the influence of grain size on radiation tolerance in the nanocrystalline regime, Appl. Phys. Lett. 112(18) (2018) 181903.
[212] O. El-Atwani, J.E. Nathaniel, A.C. Leff, B.R. Muntifering, J.K. Baldwin, K. Hattar, M.L. Taheri, The role of grain size in He bubble formation: implications for swelling resistance, J. Nucl. Mater. 484 (2017) 236.
[213] C.M. Barr, O. El-Atwani, D. Kaoumi, K. Hattar, Interplay between grain boundaries and radiation damage, JOM (2019) 1.
[214] Z.B. Jiao, C.A. Schuh, Nanocrystalline Ag-W alloys lose stability upon solute desegregation from grain boundaries, Acta Mater. 161 (2018) 194.
[215] E. Botcharova, J. Freudenberger, L. Schultz, Cu–Nb alloys prepared by mechanical alloying and subsequent heat treatment, J. Alloys Compd. 365(1-2) (2004) 157.
[216] X. Zhang, N. Li, O. Anderoglu, H. Wang, J.G. Swadener, T. Höchbauer, A. Misra, R.G. Hoagland, Nanostructured Cu/Nb multilayers subjected to helium ion-irradiation, Nucl. Instrum. Methods Phys. Res., Sect. B 261(1-2) (2007) 1129.
[217] E.G. Fu, J. Carter, G. Swadener, A. Misra, L. Shao, H. Wang, X. Zhang, Size dependent enhancement of helium ion irradiation tolerance in sputtered Cu/V nanolaminates, J. Nucl. Mater. 385(3) (2009) 629.
[218] M. Zhernenkov, S. Gill, V. Stanic, E. DiMasi, K. Kisslinger, J.K. Baldwin, A. Misra, M.J. Demkowicz, L. Ecker, Design of radiation resistant metallic multilayers for advanced nuclear systems, Appl. Phys. Lett. 104(24) (2014) 241906.
[219] M.J. Demkowicz, D. Bhattacharyya, I. Usov, Y.Q. Wang, M. Nastasi, A. Misra, The effect of excess atomic volume on He bubble formation at fcc–bcc interfaces, Appl. Phys. Lett. 97(16) (2010) 161903.
[220] A. Kashinath, A. Misra, M.J. Demkowicz, Stable storage of helium in nanoscale platelets at semicoherent interfaces, Phys. Rev. Lett. 110(8) (2013) 086101.
[221] M. Samaras, P.M. Derlet, H. Van Swygenhoven, M. Victoria, Radiation damage near grain boundaries, Philos. Mag. 83(31-34) (2003) 3599.
[222] J. Luo, Developing interfacial phase diagrams for applications in activated sintering and beyond: current status and future directions, J. Am. Ceram. Soc. 95(8) (2012) 2358.
[223] J.F. Ziegler, M.D. Ziegler, J.P. Biersack, SRIM–The stopping and range of ions in matter (2010), Nucl. Instrum. Methods Phys. Res., Sect. B 268(11-12) (2010) 1818.
[224] R.E. Stoller, M.B. Toloczko, G.S. Was, A.G. Certain, S. Dwaraknath, F.A. Garner, On the use of SRIM for computing radiation damage exposure, Nucl. Instrum. Methods Phys. Res., Sect. B 310 (2013) 75.
[225] D.B. Bober, A. Khalajhedayati, M. Kumar, T.J. Rupert, Grain boundary character distributions in nanocrystalline metals produced by different processing routes, Metall. Mater. Trans. A 47(3) (2016) 1389.
[226] R.R. Keller, R.H. Geiss, Transmission EBSD from 10 nm domains in a scanning electron microscope, J. Microscopy 245(3) (2012) 245.
[227] P.W. Trimby, Orientation mapping of nanostructured materials using transmission Kikuchi diffraction in the scanning electron microscope, Ultramicroscopy 120 (2012) 16.
[228] C. Lu, Z. Lu, X. Wang, R. Xie, Z. Li, M. Higgins, C. Liu, F. Gao, L. Wang, Enhanced radiation-tolerant oxide dispersion strengthened steel and its microstructure evolution under helium-implantation and heavy-ion irradiation, Sci. Rep. 7 (2017) 40343.

[229] I.S. Kim, J.D. Hunn, N. Hashimoto, D.L. Larson, P.J. Maziasz, K. Miyahara, E.H. Lee, Defect and void evolution in oxide dispersion strengthened ferritic steels under 3.2 MeV Fe+ ion irradiation with simultaneous helium injection, J. Nucl. Mater. 280(3) (2000) 264.
[230] O. El-Atwani, E. Martinez, E. Esquivel, M. Efe, C. Taylor, Y.Q. Wang, B.P. Uberuaga, S.A. Maloy, Does sink efficiency unequivocally characterize how grain boundaries impact radiation damage?, Phys. Rev. Mater. 2(11) (2018) 113604.
[231] M.L. Jenkins, M.A. Kirk, Characterisation of radiation damage by transmission electron microscopy, CRC Press, 2000.
[232] S.J. Zinkle, G.L. Kulcinski, R.W. Knoll, Microstructure of copper following high dose 14 MeV Cu ion irradiation, J. Nucl. Mater. 138(1) (1986) 46.
[233] N. Yoshida, K. Kitajima, E. Kuramoto, Evolution of damage structures under 14 MeV neutron, 4 MeV Ni ion and 1.25 MeV electron irradiation, J. Nucl. Mater. 122(1-3) (1984) 664.
[234] M. Azimi, G.H. Akbari, Development of nano-structure Cu–Zr alloys by the mechanical alloying process, J. Alloys Compd. 509(1) (2011) 27.
[235] A.J.E. Foreman, M.J. Makin, Dislocation movement through random arrays of obstacles, Philos. Mag. 14(131) (1966) 911.
[236] J.S. Robach, I.M. Robertson, B.D. Wirth, A. Arsenlis, In-situ transmission electron microscopy observations and molecular dynamics simulations of dislocation-defect interactions in ion-irradiated copper, Philos. Mag. 83(8) (2003) 955.
[237] N. Li, K. Hattar, A. Misra, In situ probing of the evolution of irradiation-induced defects in copper, J. Nucl. Mater. 439(1-3) (2013) 185.
[238] B.N. Singh, S.J. Zinkle, Defect accumulation in pure fcc metals in the transient regime: a review, J. Nucl. Mater. 206(2-3) (1993) 212.
[239] W.S. Cunningham, J.M. Gentile, O. El-Atwani, C.N. Taylor, M. Efe, S.A. Maloy, J.R. Trelewicz, Softening due to grain boundary cavity formation and its competition with hardening in helium implanted nanocrystalline tungsten, Sci. Rep. 8(1) (2018) 2897.
[240] W. Jäger, M. Rühle, M. Wilkens, Elastic interaction of a dislocation loop with a traction-free surface, Physica Status Solidi A 31(2) (1975) 525.
[241] W. Jäger, M. Wilkens, Formation of vacancy-type dislocation loops in tungsten bombarded by 60 keV Au ions, Physica Status Solidi A 32(1) (1975) 89.
[242] B. Muntifering, R. Dingreville, K. Hattar, J. Qu, Electron beam effects during in-situ annealing of self-ion irradiated nanocrystalline nickel, MRS Online Proc. Library Archive 1809 (2015) 13.
[243] C.W. Allen, In situ ion- and electron-irradiation effects studies in transmission electron microscopes, Ultramicroscopy 56(1) (1994) 200.
[244] J.A. Sundararajan, M. Kaur, Y. Qiang, Mechanism of electron beam induced oxide layer thickening on iron–iron oxide core–shell nanoparticles, J. Phys. Chem. C 119(15) (2015) 8357.
[245] V. Randle, O. Engler, Introduction to texture analysis: macrotexture, microtexture and orientation mapping, CRC press, 2014.
[246] D. Kaoumi, A.T. Motta, R.C. Birtcher, A thermal spike model of grain growth under irradiation, J. Appl. Phys. 104(7) (2008) 073525.
[247] D.C. Bufford, F.F. Abdeljawad, S.M. Foiles, K. Hattar, Unraveling irradiation induced grain growth with in situ transmission electron microscopy and coordinated modeling, Appl. Phys. Lett. 107(19) (2015) 191901.
[248] M. Alurralde, A. Caro, M. Victoria, Radiation damage cascades: liquid droplet treatment of subcascade interactions, J. Nucl. Mater. 183(1-2) (1991) 33.

[249] J.C. Liu, M. Nastasi, J.W. Mayer, Ion irradiation induced grain growth in Pd polycrystalline thin films, J. Appl. Phys. 62(2) (1987) 423.
[250] E.A. Holm, S.M. Foiles, How grain growth stops: a mechanism for grain-growth stagnation in pure materials, Science 328(5982) (2010) 1138.
[251] C.M. Barr, G.A. Vetterick, K.A. Unocic, K. Hattar, X.M. Bai, M.L. Taheri, Anisotropic radiation-induced segregation in 316L austenitic stainless steel with grain boundary character, Acta Mater. 67 (2014) 145.
[252] T.R. Allen, J.T. Busby, G.S. Was, E.A. Kenik, On the mechanism of radiation-induced segregation in austenitic Fe–Cr–Ni alloys, J. Nucl. Mater. 255(1) (1998) 44.
[253] H. Wiedersich, P.R. Okamoto, N.Q. Lam, A theory of radiation-induced segregation in concentrated alloys, J. Nucl. Mater. 83(1) (1979) 98.
[254] G.S. Was, J.P. Wharry, B. Frisbie, B.D. Wirth, D. Morgan, J.D. Tucker, T.R. Allen, Assessment of radiation-induced segregation mechanisms in austenitic and ferritic–martensitic alloys, J. Nucl. Mater. 411(1) (2011) 41.
[255] R.S. Averback, Fundamental aspects of ion beam mixing, Nucl. Instrum. Methods Phys. Res., Sect. B 15(1) (1986) 675.
[256] N. Li, M.S. Martin, O. Anderoglu, A. Misra, L. Shao, H. Wang, X. Zhang, He ion irradiation damage in Al/Nb multilayers, J. Appl. Phys. 105(12) (2009) 123522.
[257] N. Li, E.G. Fu, H. Wang, J.J. Carter, L. Shao, S.A. Maloy, A. Misra, X. Zhang, He ion irradiation damage in Fe/W nanolayer films, J. Nucl. Mater. 389(2) (2009) 233.
[258] G.S. Rohrer, The role of grain boundary energy in grain boundary complexion transitions, Curr. Opin. Solid State Mater. Sci. 20(5) (2016) 231.
[259] S.C. Pun, W. Wang, A. Khalajhedayati, J.D. Schuler, J.R. Trelewicz, T.J. Rupert, Nanocrystalline Al-Mg with extreme strength due to grain boundary doping, Mater. Sci. Eng., A 696 (2017) 400.
[260] K.N. Tu, A.M. Gusak, M. Li, Physics and materials challenges for lead-free solders, J. Appl. Phys. 93(3) (2003) 1335.
[261] Y. Li, D. Raabe, M. Herbig, P. Choi, S. Goto, A. Kostka, H. Yarita, C. Borchers, R. Kirchheim, Segregation stabilizes nanocrystalline bulk steel with near theoretical strength, Phys. Rev. Lett. 113(10) (2014) 106104.
[262] C.J. Marvel, P.R. Cantwell, M.P. Harmer, The critical influence of carbon on the thermal stability of nanocrystalline Ni–W alloys, Scripta Mater. 96 (2015) 45.
[263] Z. Yu, P.R. Cantwell, Q. Gao, D. Yin, Y. Zhang, N. Zhou, G.S. Rohrer, M. Widom, J. Luo, M.P. Harmer, Segregation-induced ordered superstructures at general grain boundaries in a nickel-bismuth alloy, Science 358(6359) (2017) 97.
[264] C. Nethravathi, T. Nisha, N. Ravishankar, C. Shivakumara, M. Rajamathi, Graphene–nanocrystalline metal sulphide composites produced by a one-pot reaction starting from graphite oxide, Carbon 47(8) (2009) 2054.
[265] X. Huang, X. Qi, F. Boey, H. Zhang, Graphene-based composites, Chem. Soc. Rev. 41(2) (2012) 666.
[266] J.A. Thornton, The microstructure of sputter-deposited coatings, J. Vacuum Sci. Tech. 4(6) (1986) 3059.
[267] J.P. Liebig, M. Göken, G. Richter, M. Mačković, T. Przybilla, E. Spiecker, O.N. Pierron, B. Merle, A flexible method for the preparation of thin film samples for in situ TEM characterization combining shadow-FIB milling and electron-beam-assisted etching, Ultramicroscopy 171 (2016) 82.

[268] C. Li, G. Habler, L.C. Baldwin, R. Abart, An improved FIB sample preparation technique for site-specific plan-view specimens: a new cutting geometry, Ultramicroscopy 184 (2018) 310.
[269] I. Karakaya, W.T. Thompson, The Ag-Sn (silver-tin) system, Bulletin of Alloy Phase Diagrams 8(4) (1987) 340.
[270] M.B. Zhou, X. Ma, X.P. Zhang, Premelting behavior and interfacial reaction of the Sn/Cu and Sn/Ag soldering systems during the reflow process, J. Mater. Sci. 23(8) (2012) 1543.
[271] M.J. Aus, B. Szpunar, U. Erb, A.M. El-Sherik, G. Palumbo, K.T. Aust, Electrical resistivity of bulk nanocrystalline nickel, J. Appl. Phys. 75(7) (1994) 3632.
[272] W. Wu, S.H. Brongersma, M. Van Hove, K. Maex, Influence of surface and grain-boundary scattering on the resistivity of copper in reduced dimensions, Appl. Phys. Lett. 84(15) (2004) 2838.
[273] A.F. Mayadas, M. Shatzkes, Electrical-resistivity model for polycrystalline films: the case of arbitrary reflection at external surfaces, Phys. Rev. B 1(4) (1970) 1382.